THESIS FOR DEGREE OF DOCTOR OF PHILOSOPHY

Adding Utility to Carbon Materials: Introducing Dopants Using Highly Soluble Metal Salts and Functionalizing Surfaces via Bromomethylation

SAMUEL JOSEPH FRETZ

CHALMERS

Department of Chemistry and Chemical Engineering
CHALMERS UNIVERSITY OF TECHNOLOGY
Gothenburg, Sweden 2019

Adding Utility to Carbon Materials: Introducing Dopants Using Highly Soluble Metal Salts and Functionalizing Surfaces *via* Bromomethylation

SAMUEL JOSEPH FRETZ
ISBN 978-91-7905-162-4

Doktorsavhandlingar vid Chalmers tekniska högskola
Ny serie nr 4629
ISSN 0346-718X

Department of Chemistry and Chemical Engineering
Chalmers University of Technology
SE-412 96 Gothenburg
Sweden
Telephone +46 (0)31-772 1000

Cover: A visual representation of the utility of the bromomethylation reaction. In the first step, the carbon surface is functionalized using this reaction, which is followed by bromide displacement with ethylenediamine (EN). The carbon is used subsequently as a cathode in lithium-sulfur (Li-S batteries) where it shows improved cycling performance relative to the unmodified precursor. The lower left graphic depicts interactions between the surface-bound EN groups and a partially reduced sulfur species (lithium polysulfide, LiPS, Li_2S_8) in the battery electrolyte, which are likely responsible for the enhanced battery performance.

Printed by:
Chalmers Reproservice
Gothenburg, Sweden 2019

Adding Utility to Carbon Materials: Introducing Dopants Using Highly Soluble Metal Salts and Functionalizing Surfaces *via* Bromomethylation

Samuel J. Fretz
PhD Student at Applied Surface Chemistry (TYK)
Chemistry and Chemical Engineering
Chalmers University of Technology

Abstract

Carbon-based materials have received intense research interest over the past few decades due to their unique combination of properties including porosity, non-toxicity, chemical inertness, low density, and electrical conductivity, which has allowed them to find a wide array of applications including supercapacitors, batteries, CO_2 capture, fuel cells, and catalysis. To expand their utility, a variety of techniques have been developed to enhance their reactivity and functionality. One such method is doping, wherein heteroatoms (*i.e*. non-carbon elements) are purposefully incorporated into the carbon structure with the goal of introducing new reactivity to the material. The first paper in this thesis focuses on using soluble Fe salts as dopants for iron/nitrogen-doped ordered mesoporous carbons (Fe-OMC). The anion was found to have a strong effect on the structure, Fe loading, and oxygen reduction reaction (ORR) activity of the Fe-OMC. High Fe loadings of above 3 wt% were obtained for one of the soluble salts, but their activity in polymer electrolyte membrane fuel cells (PEMFCs) did not increase appreciably compared to the standard chloride salt. Electron paramagnetic resonance (EPR) was used to gain insight into the structure and ORR activity of the various Fe species within each Fe-OMC.

Another method for increasing the utility of carbon materials is grafting or surface functionalization, which consists of covalently attaching small, organic molecules to the carbon surface. In three papers of this thesis, we report a novel two-step method for the surface functionalization of high surface area carbon materials. The carbons are first subjected to the bromomethylation reaction then, in the second step, many nucleophiles can substitute bromide resulting in monolayer-functionalized surfaces that can be tailored for a specific application. Example nucleophiles include azide, amines, iodide, sulfite, and amide enolates. Several carbon materials efficiently and reproducibly undergo these reactions and the surface-bound groups are stable for months under ambient conditions. This two-step scheme has numerous advantages over other surface modification techniques for carbon including use of solution-phase reagents, minimal harm to the carbon framework, monolayer functionalization, and no carbon pretreatment steps. A total of 12 surface groups were synthesized, which demonstrates the synthetic flexibility of this two-step technique.

Four of the twelve modified carbons were used as cathodes in lithium-sulfur (Li-S) batteries. When used with an electrolyte containing lithium nitrate ($LiNO_3$), the functionalized cathodes show increased capacities by virtue of utilizing more S. When used with electrolytes lacking $LiNO_3$, the surface groups attenuate the lithium polysulfide (LiPS) shuttle as measured by the much higher initial Coulombic efficiencies (ICEs) recorded for the functionalized cathodes relative to the unfunctionalized control. The observations with both electrolytes evidence strong interactions between the electroactive S and the surface groups. The higher binding energies (BEs) computed by density functional theory (DFT) support strong interactions between the surface groups and various sulfur species while cyclic voltammetry (CV) and electrochemical impedance spectroscopy (EIS) lend evidence for a significantly reduced LiPS shuttle on the functionalized carbon surfaces. Based on these results with Li-S batteries, we hope that this two-step method of introducing organic groups to carbon surfaces will find wide-spread use in many applications.

Key words: carbon materials, doping, surface functionalization, Li-S batteries, fuel cells.

Acknowledgements

This doctoral thesis has been carried out with gratefully acknowledged financial support from the Swedish Energy Agency (Energimyndigheten) for project 37671-1.

First and foremost, I need to thank my supervisor, Prof. Anders Palmqvist, for his advice and guidance over the past three and half years. When I received his invitation to start my PhD at 1 AM local time in Colorado, I knew that I was about to start a great adventure! I also would like to thank my group members in chemistry, past and present: Giulio, Milene, Andrey, Yifei, Caroline, Gunnar, Joakim, Walter, Sanna, Björn, Richard, Florian, Samrand, and Ma Yi. You all have made working at Chalmers a very fun experience. Many other people in Applied Surface Chemistry (TYK) have also made these past years quite memorable who are too many to list here. I would like to extend a special thank you to my officemate and friend, Gunnar, for his advice and many conversations over the past several years.

I would also like to thank the following people:

Condensed Mattery Physics (KMF), especially Prof. Patrik Johansson and my co-supervisor, Prof. Professor Aleksandar Matic. I would like to extend my gratitude to all of the various KMF members throughout the years for your help and support with all things battery related.

My examiner, Prof. Hanna Härelind, for her advice and help with my thesis.

The post-docs who took it upon themselves to help me with my projects and serve as my scientific mentors: Florian “Den Stora” Nitze, Muhammed “Master” Abdelhamid, and Marco “The Godfather” Agostini.

My co-authors on Paper 1, Caroline and Walter, without whose help this project would not have been possible.

My former supervisor at Stanford University (Stanford, CA, USA) Prof. Daniel Stack, for the opportunity to work on the bromomethylation project (Paper 2). I am super happy our two groups could collaborate on this project! Additionally, I need to thank my friend and former labmate, Christopher Lyons, for his work with this topic. Also on this project were Ella Levin and my former co-supervisor, Prof. Christopher Chidsey. Thank you for your effort in this endeavor.

Marco Agostini for performing the battery testing and Piotr Jankowski for carrying out the DFT calculations for Paper 3. Thank you to Aleksandar and Patrik for helping with the manuscript.

My collaborators at Deakin University in Melbourne (VIC, Australia) Urbi Pal, Dr. Gaetan Gerard, and Prof. Patrick Howlett. It was great working with you all on Paper 4. I would also like to thank my other Deakin collaborators in Waurn Ponds (VIC, Australia) especially Profs. Russell Varley and Luke Henderson for the chance to work on a carbon fiber project. I need to extend a special thanks to all those at Deakin who helped me out during my short visit. You really made those months special!

My first research advisor, Prof. David Hart, at The Ohio State University (Columbus, OH, USA). I will always be grateful to him for allowing a complete novice of an undergraduate work in his lab conducting studies in synthetic organic chemistry. As it turns out, a lot of organic chemistry reactions can be run on carbon surfaces!

My former teachers Marilyn Kemp (chemistry) and Rodney McKinney (math and computer science) from my Overland High School days (Aurora, CO, USA) for their continued support and advice, despite my graduation over ten years ago. I need to give a special thanks to my speech therapist, Kathleen Chase. Without her help, I would not be where I am today.

My friends and family back in the US for their continued help in spite of the distance between us. Thank you, mom, dad, Zach, and Emily, for your help and advice throughout these years. I would also like to thank all of my other friends and family in the US, Argentina, Australia, Singapore and elsewhere for their continued friendship. Of course, I would like to thank all of the amazing people I have met during my five years in Sweden. It has been great to call Gothenburg home!

Peace, love, and chemistry,
Samuel J. Fretz

List of publications

This thesis is based on the following articles and manuscripts. References to these documents in the text are written as "Paper X" where X is the number shown below.

1. Influence of Iron Salt Anions on Formation and Oxygen Reduction Activity of Fe/N-Doped Mesoporous Fuel Cell Catalysts
   S. J. Fretz, C. Janson, W. R. Rosas, and A. E. C. Palmqvist
   Under revision at ACS Omega

2. Bromomethylation of high-surface area carbons as a versatile synthon: Adjusting the electrode-electrolyte interface in lithium-sulfur batteries
   S. J. Fretz, C. T. Lyons, E. Levin, C. E. D. Chidsey, A. E. C. Palmqvist, and T. D. P. Stack,
   Accepted to Journal of Materials Chemistry A

3. Amide- and amine-functionalized ordered mesoporous carbon Li-S battery cathodes
   S. J. Fretz, M. Agostini, P. Jankowski, P. Johansson, A. Matic, and A. E. C. Palmqvist
   Manuscript

4. Sulfonate-functionalization of carbon cathodes as a substitute for lithium nitrate in the electrolyte of lithium-sulfur batteries
   S. J. Fretz, U. Pal, G. M. A. Girard, P. Howlett, and A. E. C. Palmqvist
   Manuscript

Contribution report

1. I synthesized the Fe-OMCs and characterized them using EA, TGA, nitrogen-sorption, and XRD. I wrote the manuscript except the EPR section.
2. I synthesized the functionalized CMK3 samples and characterized them using EA, nitrogen-sorption, SAXS, XRD, and CV. I fabricated all battery cathodes and performed all battery tests. I wrote the manuscript.
3. I synthesized the functionalized CMK3 samples and characterized them using EA, nitrogen-sorption, and CV. I fabricated all battery cathodes. I co-wrote the manuscript with Dr. Marco Agostini.
4. I synthesized the functionalized CMK3 samples and characterized them using EA, nitrogen-sorption, and CV. I fabricated all battery cathodes and I performed all battery tests except for CMK3-3 and the *post-mortem* analysis with SEM and EDX. I wrote the manuscript.

Table of Contents

Abbreviations

LiPS	lithium polysulfides
Li-S	lithium-sulfur (batteries)
PEMFC	polymer/proton electrolyte membrane fuel cell
OTf^-	trifluoromethanesulfonate or triflate
OAc^-	acetate
AcOH	acetic acid
FA	furfurylamine
OMC	ordered mesoporous carbon
Fe-OMC	iron/nitrogen-doped ordered mesoporous carbon
ORR	oxygen reduction reaction
RDE	rotating disc electrode
TGA	thermogravimetric analysis
EA	elemental analysis
XRD	X-ray diffraction
SAXS	small angle X-ray scattering
XRF	X-ray fluorescence
XPS	X-ray photoelectron spectroscopy
SEM	scanning electron microscopy
EIS	electrochemical impedance spectroscopy
EPR	electron paramagnetic resonance (spectroscopy)
CC	constant current (cycling)
CV	cyclic voltammetry
BET	Brunauer-Emmett-Teller (theory for surface area determination)
BJH	Barett-Joyner-Halenda (theory for determination of pore volumes)
AC	activated carbon
DFT	density functional theory
BE	binding energy
LiTFSI	lithium bis(trifluoromethanesulfonyl)imide
TBAB	tetrabutylammonium bromide
EN	ethylenediamine
DMA	N,N-dimethylacetamide
TMMA	N,N,N',N'-tetramethylmalonamide
$LiSO_3$-R	lithium sulfonate (functional group bound to carbon surface)

This thesis is dedicated to all of the hard-working teachers, especially those in math and science, who helped me throughout the years. A special thanks to my high school chemistry teacher, Mrs. Kemp, who never gave up on me despite my protesting.

1 Introduction: carbon as an energy source and as a material

The 21st Century could very well become the most important century in human history. During the upcoming decades, humanity will face many unprecedented challenges – climate change, overpopulation, and rampant pollution to name a few. Furthermore, the ever-increasing desire of developing countries and communities to become industrialized puts pressure on the environment and its limited resources. A large part of industrialization and, indeed, of living a comfortable lifestyle, is reliable access to electricity. Post-industrial countries such as those in North America and Europe used combustion of reduced carbon reagents – coal and hydrocarbons – to power their industrial revolutions and the subsequent electrification. If such methods are used by the developing world and its large population in the current era, the resultant pollution will surely prove too much for the environment to handle. Thus, the burden falls on scientists and engineers to invent new methods for creating and storing electricity, not just for the developing world, but also to replace the old combustion-based systems still in place in the post-industrial world.

Electricity, by its nature, requires a conductive medium through which electrons can move. Well-known examples of conductors include metals such as Cu, Ag, Au, Fe, and Pb. Less well known is common carbon. While not as conductive as the aforementioned metals (see Table 2), carbon exhibits many advantages including low cost, high abundance, high porosity, non-toxicity, chemical inertness, and low density. More importantly, carbon possesses the unique ability to form four strong covalent bonds to itself and to most other elements in the Periodic Table. Such propensity for diverse bonding arrangements has required chemists to dedicate a whole sub-discipline of chemistry to carbon – organic chemistry. This ability also allows for easily tunable properties in the element itself; the characteristics of simple, everyday charcoal can be modulated effectively by changing its elemental composition or covalently bonding organic molecules to its surface. Ironically, carbon, which powered the Industrial Revolution and supplied the concomitant pollution, may also provide the necessary material properties for clean, renewable electricity, not as the fuel itself, but as an integral, indispensable component of 21st Century technologies.

Humanity's familiarity with carbon may also provide some distinct advantages for using this material in emerging technologies. Carbon is one of the few elements that has been known to human beings since ancient times. To the earliest human civilizations, carbon was known in the forms of soot and charcoal.[1] One of the main allotropes of carbon, diamond, was likely known to the Chinese as early as 2500 BCE.[2] The other common allotrope of carbon, graphite, was probably recognized in antiquity but was likely confused with minerals of similar appearance and texture like molybdenite (MoS_2).[3] Whereas carbon in diamond is sp^3 hybridized and possesses properties such as optical transparency, extreme hardness, and electrical insulation, carbon in graphite is sp^2 hybridized and displays strong visible absorptions, soft, lubricating properties, and electrical conductivity. If the carbon material does not show any long-range order, it is usually referred to as amorphous carbon (sometimes called charcoal) and exhibits a mixture of sp^2 and sp^3 hybridization. This type of carbon, however, typically shares more characteristics with graphite, namely the appearance (black) and electrical conductivity. It is this form of carbon that has found prominent use in energy applications (*vide infra*). In Roman times, amorphous carbon was made by heating wood in a clay dome.[3] This is the same chemistry that is used to make carbon today – a technique called *pyrolysis* or *carbonization*.

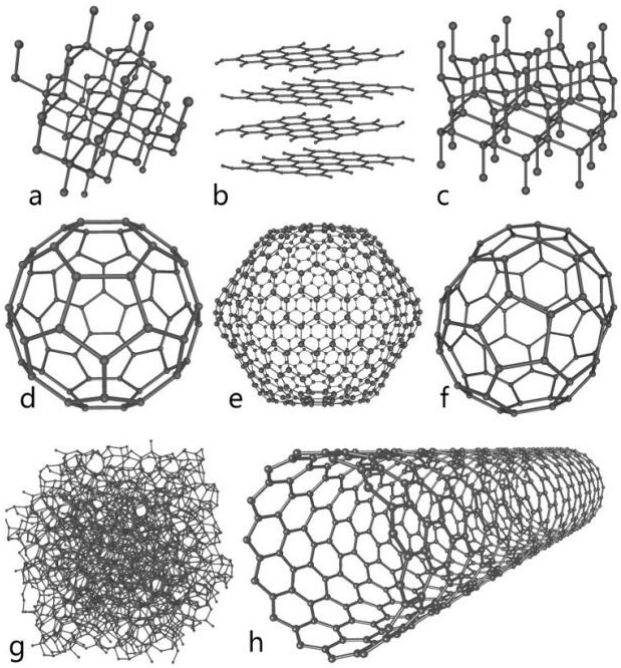

Figure 1. The structures of eight allotropes of elemental carbon. a) Diamond, b) Graphite, c) Lonsdaleite, d) C_{60} also called Buckminsterfullerene), e) C_{540} Fullerene, f) C_{70} Fullerene, g) Amorphous carbon, h) Single-walled carbon nanotube. [4] This thesis is primarily concerned with the amorphous allotrope of carbon.

Amorphous carbons are of considerable research interest because they are easy to make and modify and have tunable properties to meet the demands of a given application, which include batteries, fuel cells, supercapacitors, CO_2 capture, and catalysis among others. The central theme of this thesis is the synthesis and modification of amorphous carbons with the goal of improving their performance in batteries and fuel cells.

2 Synthesis of novel carbon materials

2.1 Natural and artificial carbon synthesis

Three of the main allotropes of carbon - graphite, diamond, and amorphous - are formed in three very distinct ways. Naturally occurring graphite forms in either metamorphic or igneous environments in the Earth's crust from amorphous precursors like coal and decaying organic matter, requiring high temperature and pressure. Graphite is never formed in sedimentary environments. Formation of graphite requires that the local concentration of O be low or else carbon oxides (CO and CO_2) are formed.[5] Diamond, by contrast, is not formed within the Earth's crust, but rather deep within the Earth's mantle at depths of 140 to 190 kilometers, where the pressure is much greater than for the formation of graphite. Carbon-containing minerals provide the carbon source and the diamond growth occurs slowly, over periods of 1 to 3.3 billion years. After formation, diamonds are brought to the Earth's surface by volcanic activity. Despite common belief, diamonds are *not* formed from coal (coal metamorphism).[6] Figure 2 shows the phase diagram for carbon and the conditions under which graphite and diamond form.[7]

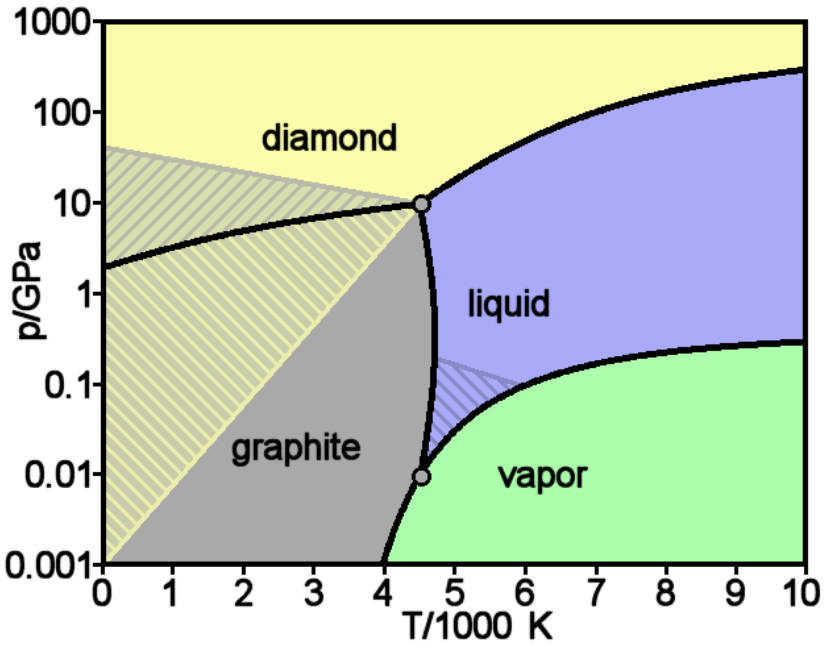

Figure 2. Phase diagram for carbon. Note that the pressures required to form diamond are much greater than for graphite. The hashed regions indicate conditions under which one phase is metastable; two phases can co-exist in these regions.[7]

The amorphous form of carbon occurs when a carbon-containing material, many times an organic polymer like those found in wood, is heated with insufficient O to combust the whole sample. This is the reason why the Romans used clay domes when heating wood to form charcoal – to exclude excess O. The carbon-containing starting material is called the *carbon precursor*, and in principle, any carbon-containing substance can serve as one. In the modern era, this method of transforming organic material into carbon is called *pyrolysis* or *carbonization* and is typically performed under inert atmospheres (*i.e.* N_2 or Ar). During this process, most, but not all, of the heteroatoms are expelled from the structure during heating, leaving behind a black, soft residue. The resulting structure is largely based on carbon-carbon bonds and is typically >90% carbon by mass.[8] Normal temperatures used for carbonization are in the range of 600 °C to 3000 °C with higher temperatures chosen to decrease the heteroatom content and increase the degree of order in the carbon lattice. Indeed, heating certain types of amorphous carbons at high temperatures approaching 3000 °C produces carbons that are essentially graphitic and contain very few heteroatoms. The process of converting amorphous carbon to graphite is referred to as *graphitization*. These types of graphitizing carbons are called "soft" carbons and proceed through an intermediate liquid phase during carbonization. Examples of soft carbons are chars, soots, cokes, and coals. Conversely, materials such as cellulose and coconut shells remain entirely in the solid phase during carbonization. These materials produce carbons

that do not develop any significant degree of crystallinity after heat treatment at 3000 °C. Such carbons are designated as non-graphitizing carbons or "hard" carbons. Some examples of hard carbons include glassy carbons, carbon fibers, and carbon blacks.[8] In the case of glassy carbon, the interwoven, tangled 3D arrangement of the graphitic (graphene) sheets provide the resistance to graphitization.

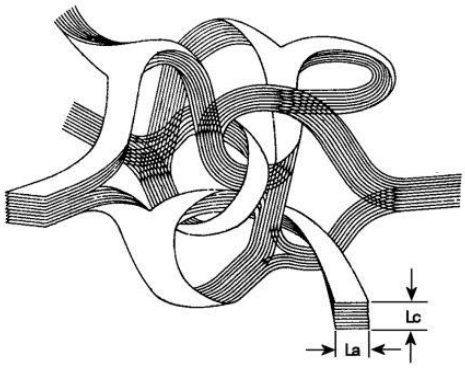

Figure 3 Drawing of the glassy carbon structure.[9] This material contains random orientations of the graphitic sheets whose interwoven nature prevents conversion to graphite upon heat treatment at 3000 °C.

As mentioned previously, the rearrangement of carbon atoms to form graphite generally requires heating at very high temperatures. However, adding certain inorganic and organic compounds can accomplish the same feat at lower temperatures. Many different additives have been used to induce graphitization including compounds of Co, Cu, and Fe.[8] This alternative approach is called catalytic graphitization and was observed in Paper 1 in one of the samples (Section 5).

2.2 Carbon synthesis with doping

Not only does the nature of the carbon precursor have a dramatic impact on the hard/soft nature of the carbon and the degree of graphitization, but also on its elemental composition. The percentage of heteroatoms (any atom besides carbon) can constitute a significant percentage of the carbon material's structure, usually in the range of 1-12 wt%.[10] Purposeful incorporation of heteroatoms into the carbonaceous structure, called *doping*, is an effective way of altering the carbon's properties. The main method for creating doped carbon materials is a bottom-up method involving the carbonization of organic precursors, which contain the desired heteroatoms. In this way, the bulk of the carbon is doped and also many of these dopants are present as surface functional groups, thereby modifying the material's surface properties. In the context of an application, the dopant can play just as important of a role as the carbon's structure.[11] For the syntheses involving doping, the temperature of carbonization must not be too high or else graphitization will occur to some extent, which lowers the heteroatom content. On the other hand, temperatures that are too low could result in incomplete carbonization (*i.e.* organic residues present in the carbon), which lowers the conductivity and structural strength of the carbon.

In a typical bottom-up synthesis involving doping, three main components are employed:

1. A carbonizable, organic molecule, called the carbon precursor, which supplies the bulk of the carbon in the final product.
2. A structure directing agent or template to give the final carbon a porous, high surface area structure.
3. Any additives needed for doping if the carbon precursor lacks that element.

Examples of structure directing agents and templates include mesoporous oxides, *e.g.* silica[12] and $CaCO_3$,[13] and eutectic salt mixtures such as $ZnCl_2$ with NaCl.[14] Carbonization of the carbon precursor mixture without such agents will yield bulk carbons with low surface area and porosity. A negative replica of the structure directing agent results from this method.

An important trait of the carbon precursor is non-volatility. As mentioned previously, any carbon-containing substance can serve as a carbon precursor. However, given the high temperatures involved for

carbonization, if the rate of evaporation is higher than carbonization, very little material will remain. It is for this reason that a polymerizable carbon precursor is often employed in such syntheses. As a monomer, the precursor can easily infiltrate the pores of the template *via* fast diffusion. Then, by polymerizing the precursor within the pores prior to carbonization, the boiling point is greatly increased, thereby making carbonization more likely. One study also found that pre-polymerizing the precursor also resulted in better replication of the template compared to the unpolymerized control sample.[15] In some syntheses, a solvent such as water or ethanol is employed if the carbon precursor and/or additives are solids at room temperature (*e.g.* glucose, urea);[13] in others, the carbon precursor is also the solvent (*e.g.* furfurylamine,[15] furfuryl mercaptan[16]).

Additives can be a key factor in the overall doping scheme, especially when those elements are not commonly found in carbon precursors or are difficult to synthesize. This is the case with transition metals, where, instead of using expensive, bulky metal complexes such as porphyrins,[17-21] phthalocyanines,[22-24] and phenanthroline complexes, [25-26] a practical solution is to simply dissolve the transition metal, typically as a salt, directly into the carbon precursor solution. The major difference between doping with main group elements and doping with transition metal salts is that, in the case of salts, there are two parts: the metal cation and the counter anion. The focus of Paper 1 (Section 5) is to show the profound influence of the anion on Fe/N-doped ordered mesoporous carbons (Fe-OMCs).

2.3 Surface functionalization of carbon materials

Another method to expand the utility of materials, carbon included, is to covalently bond small organic molecules to their surface, sometimes called grafting. While surface functionalization can be confused with doping since all the grafted functional groups contain one or more types of heteroatoms (see Section 6.1), in the context of this thesis, doping refers exclusively to the bottom-up, templated process using heteroatom-containing precursors, which was detailed in the previous section. In contrast to doping, surface functionalization takes a preformed material and subjects it to reactive species in either the solution or gas phase to form covalent bonds with the surface. The key distinction between the two methods is that doping changes the elemental composition of *both* the bulk material and the surface while grafting affects *only* the surface of the material, leaving the bulk material unchanged.

Surface functionalization has been used extensively for other materials: for gold, thiols are employed to attach organic groups to the surface; for TiO_2, carboxylic and phosphonic acids can add additional functionality by forming titanol esters; for silica, silanes are routinely used to graft organic functional groups to surface silanols. In the case of carbon materials, the relatively unreactive surface means that more forceful conditions are required.

One common method is oxidation with O_2, O_3, HNO_3, H_2SO_4, or H_2O_2, which forms carboxylic acids, alcohols, and ketones and other O-containing functional groups.[27-30] In a second step, organic chemistry reactions can couple small molecules to these functional groups. Examples include esterifications,[31] amidations,[32] S_N2 reactions with alkyl chlorides/bromides,[33] or silinations with organic silanes.[34-36] However, the first step involves relatively harsh conditions to oxidize the carbon surface. If such conditions are not chosen carefully, prolonged exposure to the oxidant can result in destruction of the carbon framework and loss of its porosity and electrical conductivity.[37] With gas phase oxidants like O_2 and O_3, too high of temperature and/or too long of exposure can result in complete combustion of the carbon material.

As will be discussed in Section 6.1, reactions ran on carbon surfaces are significantly simplified if the surface group contains at least one element not naturally present within the carbon substrate. Since O is almost always present in carbon materials, oxidation provides a poor “elemental handle” by which to identify the newly introduced surface groups. Moreover, the formation of multiple O-based functional groups on the surface during the first oxidation step complicates the second coupling step.

One of the more common grafting techniques is attachment *via* diazonium chemistry. Using this method, a an aniline derivative is treated with isoamyl nitrite,[38] sodium nitrite,[39] or nitrosonium hexafluorophosphate[40] usually under acidic conditions to form the diazonium salt *in situ*, which then reacts

with the carbon surface while liberating N_2. In other cases, the carbon is treated with a previously synthesized diazonium salt, which is then reduced at the carbonaceous electrode to functionalize the surface.[41-43] This approach has the advantage of avoiding the deterioration of the carbon skeleton associated with surface oxidation. However, the diazonium species is highly reactive and can react with an already grafted molecule on the surface, forming multilayers. If enough layers are attached to the surface, the carbon material will suffer from pore clogging, drastically reduced surface area, and easily detached surface groups.[40, 43] Additionally, diazonium salts are hard to synthesize and isolate and are not compatible with many functional groups.

The focus of Papers 2-4 (Section 6) is to introduce a new type of surface modification reaction to the field of carbon materials – the bromomethylation reaction. This reaction is reproducible, highly selective, and yields high surface coverages in a strictly monolayer fashion. Most importantly, the bromomethyl groups grafted onto the carbon surfaces serve as versatile attachment points for a wide variety of organic functional groups in subsequent surface reactions. The modified carbons are then applied to the field of Li-S in an effort to see how the surface groups affect the battery cycling (Section 7).

3 Methods for characterizing carbon materials

The characterization of the synthesized or surface-modified carbons can be divided into six main categories: elemental, structural, thermal, electrochemical, magnetic, and computational. Each is discussed in their own separate section.

1. Elemental: elemental or combustion analysis (EA), X-ray fluorescence (XRF), and X-ray photoelectron spectroscopy (XPS).
2. Structural: nitrogen-sorption (N_2-sorption), X-ray diffraction (XRD), small angle X-ray scattering (SAXS), and scanning electron microscopy (SEM).
3. Thermal: thermogravimetric analysis (TGA).
4. Electrochemical: rotating disk electrode (RDE), cyclic voltammetry (CV), and electrochemical impedance spectroscopy (EIS).
5. Magnetic: Electron paramagnetic resonance (EPR)
6. Computational: Density functional theory (DFT)

In many ways, both polymer electrolyte membrane fuel cells (PEMFCs) and lithium-sulfur (Li-S) batteries can also be considered characterization techniques, specifically electrochemical techniques. Indeed, this manner of thinking is used several times throughout this thesis. But given that these are also applications and determine the overall project design, the background of such devices is discussed in its own section (Section 4).

3.1 Elemental characterization

Knowing the elemental make-up of a carbon material is perhaps the single most important characterization. That is, for both heteroatom doping and surface group synthesis, the modifying groups always have new elements that are not present naturally in the carbon material (normally H, C, and O), which allows for facile determination of their presence. In principle, any other element besides these three can be used, but, in practice, certain elements are easier to use than others as detailed below. Elemental characterization falls into two broad categories: quantification (EA and XRF) or qualification (XPS).

3.1.1 Elemental analysis (EA)

Elemental or combustion analysis (EA) is a quick and simple way of analyzing the H, C, N, and S concentrations in a sample. A small quantity of sample (2-4 mg) is placed in a small piece of tin foil and loaded into the elemental analyzer. The sample is then dropped into a combustion tube where it is heated at 1100 °C in a pure O_2 atmosphere to ensure complete combustion of the sample. In subsequent steps, the excess O_2 is removed and the gases are reduced and purified such that only simple gases, products of the HCNS elements, remain. H is analyzed as H_2O, C as CO_2, N as N_2, and S as SO_2. These four gases are collected, quantified, and then presented as a weight percent of the total sample mass. The quantification happens in a single run. All other elements in the sample, whether gaseous and non-detectible (*e.g.* O, P, Cl, F) or solid and non-combustible (*e.g.* Fe, Si, Cu) are presented as the difference between the HCNS masses and 100%. EA, when combined with other techniques such as TGA, XPS, and XRF, can provide powerful combination of tools for elucidating the elemental composition of a material.

EA was conducted on an Elementar Vario MICRO Cube HCNS analyzer. In the context of this thesis, EA was used to determine the elemental content (primarily N and S) of the Fe-OMCs in Paper 1 (Section 5.2) and some the surface group loadings in Papers 2-4 (Section 6).

3.1.2 X-ray fluorescence (XRF)

X-ray fluorescence (XRF) is a technique used to quantify the heavy elements in a sample. The sample is irradiated with high-energy X-rays and the secondary or characteristic X-rays emitted from the sample are measured. Based on the intensity of these characteristic X-rays, the elemental composition of the sample can be determined. The intensity is compared to calibration data in the instrument, which yields reasonably

accurate concentrations to about 0.1 wt%. More exact concentration determinations, down to the parts per million (ppm) level, require that a calibration curve be made from similar samples with known concentrations. In principle, the lightest element that can be measured and quantified by XRF is Be, but in practice, due to low X-ray yields from lighter elements, elements lighter than Na are difficult to measure. Unlike XPS, XRF spectroscopy is conducted in transmission mode such that the entire sample is measured; thus, XRF yields bulk elemental compositions. One of its primary disadvantages of XRF, however, is that the oxidation state or any other bonding information of the element in question cannot be determined.

XRF was conducted on a Spectro Xepos HE XRF spectrometer using calibration data supplied by the manufacturer. In the context of this thesis, XRF is used to determine the Fe loadings in the Fe-OMCs in Paper 1 (Section 5.2) and many of the surface group loadings, particularly Br, in Papers 2-4 (Section 6).

3.1.3 X-ray photoelectron spectroscopy (XPS)

X-ray photoelectron spectroscopy (XPS) is a characterization tool for the study of the elemental composition, oxidation state, and electronic structure of the surface of a material. Under high vacuum, the sample is irradiated with X-rays of a known energy and electrons are ejected, called photoelectrons. Based on the energy of these electrons, a binding energy can be measured, using Equation 1.

$$E_b = h\nu - E_k \tag{1}$$

E_b = electron binding energy
$h\nu$ = energy of incident X-rays
E_k = kinetic energy of photoelectrons

The binding energy is unique to a given element and can be used to determine the elemental composition at the surface. Small variations in this binding energy reveal the oxidation state of the element. For example, the approximate binding energy of carbon in C-C bonds is 283 eV whereas in C=O bonds it is 286 eV.[44] Another important aspect of XPS is its surface sensitivity. The probing depth of XPS is typically between 1 - 5 nm. For comparison, XRD probes many microns into the sample, depending on its composition. A major strength of XPS is its ability to measure most elements, specifically Li and higher. Other X-ray techniques (XRF, EXAFS) are only applicable to heavier elements (Na and higher).

XPS analysis was ran on a Quantum 2000 scanning ESCA microprobe from Physical Electronics with a monochromatic Al K_α (1486.6 eV) X-ray source. In the context of this thesis, XPS is used to study the surface groups in Papers 2-4. It is particularly important in determining the bonding arrangements of the surface bromomethyl, amide, and lithium sulfonate groups (Sections 6.6 and 6.12).

3.2 Structural characterization

Structural characterization determines most of the non-element specific aspects of the carbon including its atomic and meso-structure, surface area, and overall porosity.

3.2.1 Nitrogen-sorption

Nitrogen-sorption (N_2-sorption), short for nitrogen adsorption-desorption, is a technique used to study the surfaces of solid materials. It can reveal useful information about surface properties of a powder including surface area, pore volume, and pore diameter distributions. Nitrogen adsorption on solid surfaces and in pore spaces is a complex phenomenon involving several energy interactions and phase changes. In a typical experiment, the pre-weighed, rigorously dried powder is placed in a tube of known volume and attached to the instrument. The sample is cooled in a liquid nitrogen bath and small aliquots of N_2 are administered by the instrument. Since the surface atoms of the solid have a bonding deficiency, it becomes energetically favorable at these low temperatures to interact with the N_2 molecules, *i.e.* physisorption. At low pressures, well below the saturation pressure (P_0), the N_2 molecules adsorb to the most energetic sites on the surface, eventually forming a monolayer. At this stage, the BET calculation is performed (Equation 6) to determine

the surface area of the material; the more N_2 adsorbed at this stage, the higher the surface area (Equation 2).

$$\frac{p}{V(p_0 - p)} = \frac{1}{V_m C} + \frac{C-1}{V_m C}\left(\frac{p}{p_0}\right) \quad (2)$$

$$S = \frac{V_m \sigma N_A}{m V_0} \quad (3)$$

p = partial pressure of nitrogen (mmHg)
p_0 = saturation pressure of nitrogen (mmHg)
V = volume of nitrogen adsorbed (cm^3 at STP)
V_m = amount of nitrogen in a monolayer (cm^3 at STP)
C = constant showing the interaction between nitrogen and the surface (unitless)
S = specific surface area ($m^2\ g^{-1}$)
σ = molecular area of nitrogen (16.2 $Å^2$ per molecule)
N_A = Avogadro's number (6.023 x 10^{23} molecules per mol)
m = sample mass (g)

Using the above equations, a plot of $P/(V(p_0 - p))$ *vs.* p/p_0 should yield a straight line with intercept $1/V_mC$ and slope of $(C-1)/V_mC$. From the line of regression, the value of C and V_m can be obtained. Subsequently, Equation 3 can be utilized to determine the surface area of the material normalized by mass.

As more N_2 is administered to the sample, multilayers begin to form. Inside the pore volume, as the multilayers come into close proximity to each other, the additional gas molecules are now bonded on multiple sides and condensation becomes very favorable. Called capillary condensation, this results in a large quantity of gas to adsorb over a short range of pressures. At this point, the BJH calculation is performed to determine the pore volume and pore size distributions of the material. The pressure is increased further to nearly the saturation pressure (p_0), at which point the pressure is reduced and the desorption isotherm is measured. For porous materials, it is common to observe a hysteresis; on desorption, the pressure must be lowered below the pressure at which the capillary condensation occurred during the adsorption isotherm (see Figure 15a for an example).

Nitrogen-sorption analyses were conducted on a TriStar 3000 Instrument. In the context of this thesis, nitrogen-sorption was used to measure surface area and study the porosity of the synthesized Fe-OMCs in Paper 1 (Section 5.3). It was also used to quantify the decrease in surface area, pore volume, and average pore diameter that accompanied surface modification of carbons in Papers 2-4 (Sections 6.5 and 6.12).

3.2.2 X-ray diffraction (XRD)

X-ray diffraction (XRD) is a technique used to probe the atomic scale of a crystalline solid. The sample is irradiated with monochromatic X-rays with wavelengths similar to interatomic spacings (*e.g.* for Cu K_α X-rays, λ = 1.54 Å), which interact with the sample and form a diffraction pattern. Typically, the sample is a fine powder so all possible crystal orientations relative to the X-rays are possible. This collapses the diffraction pattern to one dimension: the angle between the incoming and diffracted X-rays (*i.e.* 2θ). By contrast, for single crystal X-ray diffraction, the two angles between the crystal and the X-rays are considered, which yields more structural information at the cost of more complicated instrumentation and sample preparation.

The angle between the sample and the X-rays is scanned and the intensity of the reflected radiation is measured. Diffraction occurs when some of the crystallites in the sample meet the requirements of Bragg's Law (Equation 4).

$$2dsin\theta = n\lambda \quad (4)$$

n = integer (diffraction order)
d = interatomic spacing (Å)
θ = angle between sample and the incident X-rays (°)
λ = wavelength of the X-rays (Å)

Structural information about the sample is contained in the angle at which diffraction occurs (unit cell parameters, symmetry), the intensity of the reflection (atomic positions within the lattice, relative concentrations for impure samples), and shape of the peak or full width at half maximum (crystallite size and defect concentrations).

The XRD measurements were carried out on finely ground powder samples using a Bruker XRD D8 Advance instrument operated in the Bragg-Brentano geometry using Cu K_α radiation. In the context of this thesis, XRD was used to test for graphitization and crystalline Fe species in the Fe-OMCs in Paper 1 (Section 5.3). XRD was also employed to assess the damage to the carbon atomic structure in Paper 2 (Section 6.12).

3.2.3 Small angle X-ray scattering (SAXS)

Small angle X-ray scattering (SAXS) is closely related to other X-ray techniques, particularly XRD, but whereas XRD probes atomic scale periodicity (*i.e.* atomic lattices at the Ångström scale), SAXS studies periodicity on a larger scale, called the mesoscale, which is typically from 1 to 100 nm. The corresponding 2θ angles are thus much smaller; as shown in Equation 4, if d is much larger, then θ, or $\sin(\theta)$, must be much smaller to equal the same value of $n\lambda$. Typical 2θ values for SAXS are 1° to 5° while for XRD 10° to 80° is the common range. SAXS can reveal information about meso-porosity, micelles in solution, and alignment of nanofibers among others. In SAXS, the scattering contrast that X-rays experience from differences in electron density in a material is used to probe structural order in the material. This electron density difference appears, for example in a mesoporous material, between the pore walls made of SiO_2 or carbon and the pore volume filled with air. As with XRD, the diffraction peaks can be indexed using the Bragg equation, but in SAXS these peaks represent long-range order on the mesoscale.

SAXS measurements were performed on a Mat:Nordic SAXS/WAXS/GISAXS instrument from SAXSLAB using a Cu K_α radiation source. In the context of this thesis, SAXS was used to study the pore structures of the silica-templated Fe-OMCs in Paper 1 (Section 5.3) and to assess damage to the carbon meso-structure as a result of surface functionalization in Paper 2 (Section 6.12).

3.2.4 Scanning electron microscopy (SEM)

Scanning electron microscopy (SEM) is a powerful tool for studying the morphology and surface characteristics of materials. In SEM, there is an electron gun to provide high energy electrons (typically 1 – 20 kV) and a condenser system to control illumination of the sample. When the electrons interact with the sample, several signals are produced which contain information of the surface topography and elemental composition. These signals include secondary electrons, backscattered electrons, and characteristic X-rays. The most common imaging signal is the secondary electrons (SE) while the characteristic X-rays can be used to determine the elemental composition of the sample. The focused electron beam scans over the sample's surface in a raster pattern to generate an image. The resolution obtained in some SEMs can be below 1 nm, although for most SEMs a resolution of 20 nm is more common.

Scanning electron microscope (SEM) images of CMK3 powders were obtained on a LEO Ultra 55 SEM from Carl Zeiss AG using a 20-kV accelerating voltage and the InLens SE detector. Images were taken at magnifications of 1k, 5k, 10k, and 50k. In the context of this thesis, SEM was used to study the carbon morphology of CMK3 powders before and after surface functionalization (Section 6.12).

3.3 Thermal characterization

3.3.1 Thermogravimetric analysis (TGA)

Thermogravimetric analysis (TGA) is a method of thermal analysis where the mass of the sample is measured as a function of temperature. These measurements can provide information about various physical phenomena including phase transitions, solid-gas reactions (*i.e.* oxidation or reduction), chemi- and physisorptions, and thermal stability. The atmosphere can be inert (N_2, Ar), oxidizing (air, O_2), reducing (H_2 in N_2), or reactive (HCl, NH_3), depending on what properties are being studied. The temperature can be increased at a constant rate (dynamic) and/or can be held constant at a given temperature (isothermal). TGA can be coupled with other techniques such as differential scanning calorimetry (DSC), infrared spectroscopy (FTIR), or mass spectrometry to yield additional information about the processes occurring while the sample is heated.

TGA measurements in this study were performed on a Mettler TGA-DSC. In the context of this thesis, one main TGA program was ran: heating at 30 °C min^{-1} to 900 °C followed by an isotherm at 900 °C for 20 min, both in an air atmosphere. The Fe-OMCs in Paper 1 were subjected to this program to determine their hydration weight and non-combustible residual mass (Section 5.2).

3.4 Electrochemical characterization

One method of distinguishing among various electrochemical measurements is which parameter (*e.g.* voltage, current) is applied to perturb the system and which parameter is measured as the response. In battery cycling (Section 4.1.9), a constant current is applied and the resulting voltage is measured. In both CV and RDE, the voltage is scanned between two predetermined values and the resulting current is measured. For PEMFCs (Section 4.2), the voltage is also scanned and the resultant current density measured, although, in graphing PEMFC data, the voltage is plotted on the y-axis and current density on the x-axis. Finally, for EIS, the stimulus is not based on direct current (DC) as the aforementioned techniques have used, but rather alternating current (AC): EIS experiments use an alternating voltage as the stimulus and record an alternating current as the response from which the impedance can be obtained.

3.4.1 Cyclic voltammetry (CV)

Cyclic voltammetry (CV) is an electrochemical technique utilizing a three-electrode system to investigate reaction mechanisms related to redox chemistry, principally in the solution phase. In a typical set-up, the three electrodes are the reference, working, and counter:

Working electrode (WE):	Responsible for studying the reaction(s) of interest
Counter electrode (CE):	Balances the current passed to/from the working electrode; maintains electrical neutrality in the cell
Reference electrode (RE):	Provides a constant potential against which the potential of the working electrode is measured

During the CV test, the voltage of the working electrode is scanned from an initial (V_i) and final voltage (V_f) at a constant rate over the potentials during which relevant electrochemical processes should occur. Meanwhile, the current or current density is measured as the dependent variable. When V_f is reached, the direction of the scan is reversed and the voltage is changed at the same constant rate towards V_i. Many cycles between V_i and V_f are typically performed to investigate the reversibility of the electron transfer reactions. Electrochemical events such as electron transfer into or out of the electrode are recorded as increases in the current.

Cyclic voltammetry (CV) was conducted on a VMP-3 instrument from Bio-Logic Science Instruments. In the context of this thesis, CV was used to study the impact of surface modification on electrode conductivity using two battery electrolytes in Papers 2-4 (Section 6.12). CV was also employed in Paper 2 to study the redox chemistry of the two S-containing electrolytes (catholytes, Section 7.2.3). Cells for CV were constructed in the same was as for normal battery testing (Section 4.1.8). For coin cells, the C-S cathode is

the working electrode and the Li anode serves as both the counter and reference. The CV program was meant to mimic the battery cycling as much as possible (see Section 4.1.9): The cell voltage limits of 1.8 to 2.6 V were kept the same. The slow scan rate of 50 μV s^{-1} approximates the time scale (4 hrs, 26 min for one-half scan) of the constant current cycling at 0.1C (theoretical charge or discharge in 10 hrs). Cells were initially scanned from OCV (usually around 2.1 V) down to 1.8 V.

3.4.2 Rotating disk electrode (RDE)

Rotating disc electrode (RDE) is very similar to CV. RDE also uses three electrodes and the program scans the WE voltage between V_i and V_f and the current is recorded. However, in RDE, the working electrode is not static, but rather rotated at a constant angular velocity. This creates a convection force that replenishes the solution at the electrode surface, thereby making the flux of the redox active species to the surface constant (*i.e.* the flux is independent of time). The voltage (E) is scanned at a constant rate from a potential where no redox processes occur to ($E < E_{1/2}$ where $E_{1/2}$ is defined below) to one where electron transfer is very fast ($E > E_{1/2}$). During this time, the current is measured as a function of the voltage. At low potentials, the electrode kinetics dominate (*i.e.* rate of electron transfer); at high potentials, electron transfer is fast and the reaction is under mass transport control. At these high potentials, further increases in voltages do not appreciably increase the current. This limiting current (I_L) is dependent on the rotation rate; higher rotation rates yield higher currents. The I_L can be modelled with the Levich equation:

$$I_L = 0.201nFAD^{\frac{2}{3}}\nu^{-\frac{1}{6}}c^{\infty}w^{\frac{1}{2}} \quad (5)$$

n = number of electrons transferred
F = Faraday constant (96485 C mol^{-1})
A = electrode area (cm^2)
D = diffusion constant (cm^2 s^{-1})
ν = kinematic viscosity (cm^2 s^{-1})
c^{∞} = bulk concentration (mol L^{-1})
w = rotation rate (rotations per min)

Based on the I_L and rotation rates used, the number of electrons transferred (n) can be calculated, which yields insight into the mechanism of the corresponding electrochemical event. One of the most important parameters to be gained from RDE is the half-wave potential, $E_{1/2}$, or the potential at which the current is equal to one-half of I_L. This potential can reveal how well a catalyst facilitates a reaction, with better catalysts having $E_{1/2}$ closer to the thermodynamic potential (*i.e.* less overpotential).

Rotating disk electrode measurements were carried out using a three-electrode instrument (Gamry Instruments) at room temperature. A glassy carbon rotating disk electrode was used as the working electrode. A graphite-rod counter electrode and $Ag/AgCl_{sat}$ reference electrode were used. All RDE potentials are converted to the reversible hydrogen electrode (RHE). In the context of this thesis, RDE was used to assed the catalytic abilities of the Fe-OMCs in the oxygen reduction reaction (ORR) in Paper 1 (Section 5.4).

3.4.3 Electrochemical impedance spectroscopy (EIS)

Impedance is the opposition to current that circuit creates when a voltage is applied. It is similar to resistance from direct current (DC), but impedance is applied to alternating current (AC) systems. Because of this, impedance possesses both magnitude and phase while resistance only has magnitude. An alternating voltage is applied to the circuit (in this case an electrochemical cell) as the input and an alternating current is recorded as the output. Frequencies spanning many orders of magnitude (typically 1 Hz to 1 MHz) are applied to the cell to study how the cell responds. The magnitude of the input is usually small (1-10 mV) to receive a linear response from the cell (output current is directly proportional to voltage). The impedance is the quotient of the input voltage over the output current and is normally plotted on the complex plane with the real part (Z') graphed on the x-axis and the imaginary part (Z'') graphed on the y-axis (both axes have units of Ω). Each point on this type of graph, called Nyquist plots, corresponds to a

frequency. From such a graph, information about solution resistance, charge transfer resistance, and cell resistance can be obtained.

EIS spectra were recorded on Li-S batteries made in the same was as for battery cycling (Section 4.1.8) on a Multi Potentiostat VMP3 (Bio-Logic, France). The EIS were taken using a 10 mV alternating current from 1 MHz to 0.1 Hz and were fitted using the EC-Lab software (Z Fit v. 11.12). In the context of this thesis, EIS was used to measure the cell resistance as a function of time during the self-discharge test in Paper 4 (Section 7.4.4).

3.5 Magnetic methods

3.5.1 Electron paramagnetic resonance (EPR)

Electron paramagnetic resonance (EPR) is a method for studying molecules and materials with unpaired electrons. It is qualitatively similar to Nuclear Magnetic Resonance (NMR), which measures the spins of atomic nuclei. A thorough explanation of EPR as applied to the characterization of carbon materials is detailed in a colleague's PhD thesis (Caroline Janson).[45] A brief summary is given here.

Any material or molecule with at least one unpaired electron can, in principle, be studied with EPR. In EPR, the sample is placed in an external magnetic field and the spin of the electron aligns with or against the field (more often with than against). Next, the sample is irradiated with microwaves during which time the electron can flip its spin if the microwaves have the correct energy. The proportion of electrons with spins aligned against the magnetic field increases and an absorption of microwaves is recorded. The equation determining the absorption energy (hν) is shown below (Equation 6).

$$h\nu = m_s g_e \mu_B B_0 \tag{6}$$

In this equation, m_s is the spin quantum number (1/2), g_e is the electron's "g-factor," and μ_B is the Bohr Magneton, and B_0 is the strength of the external magnetic field. Since m_s and μ_B are constants, this energy depends only upon the g-factor and the external magnetic field. The g-factor is similar to the chemical shift from NMR spectroscopy and can yield insight into the paramagnetic electron's chemical environment such as with which atoms it is most closely associated. Experimentally, either the magnetic field or the radiation frequency can be changed while the other one is kept constant, but in practice, usually the frequency is kept constant and the magnetic field is scanned. When the magnetic field is reached at which Equation 6 is met, an absorption of radiation will be recorded. Based on the magnetic field strength during absorption, the g-factor of the electron can be calculated and compared with g-factors from other EPR spectra. EPR spectra are normally reported as the first derivative so that small changes in the signal become more obvious.

EPR spectra were conducted on powder samples (10 mg) in quartz tubes using a Bruker Elexsys E500 EPR. In the context of this thesis, EPR was used to study the various Fe species contained within the Fe-OMCs in Paper 1 (Section 5.5).

3.6 Computational methods

3.6.1 Density functional theory (DFT)

Not all characterization methods need be experimental. Computations can lend insight into chemical phenomena that would be very difficult or otherwise impossible to study experimentally. A detailed explanation of Density Functional Theory (DFT) as applied to batteries and carbon surfaces is detailed in a colleague's PhD thesis (Piotr Jankowski).[46] A brief summary is given here.

DFT is a computational quantum mechanical modelling method used to study multi-atom systems, including small molecules and condensed-phase materials. Using DFT, the properties of these systems can be modelled using functionals and basis sets. Functionals calculate the electronic structure of the sample in question based on the basis sets, which are sets of functions used to represent the electronic wave

functions of the constituent atoms. The foundation for DFT is the following: *all observables of the molecular system, including the system's energy, are unambiguously defined by the electron density of the system.* Therefore, choosing an appropriate functional and basis set to accurately compute the electron density of the system in question becomes of the utmost importance. For certain systems, new factors need to be taken into account to calculate an accurate electron density. For example, factors that many DFT calculations struggle to model include various types intermolecular interactions (*e.g.* hydrogen bonding and van der Walls forces), large numbers of consecutive π bonds, resulting in highly conjugated systems (*e.g.* conjugated polymers, organic dyes); and non-ground states (*e.g.* excited and transition states). Some of the possible information that DFT calculations can give are optimized chemical structures, molecular energies as a function of a geometric parameter (*e.g.* bond length or angle), NMR chemical shifts, predicted infrared (IR), Raman, and UV-Vis spectra, and interaction energies (also called binding energies, BEs).

DFT calculations were ran using Gaussian16 B.01.[47] In the context of this thesis, DFT was used to calculate the BEs between the carbon surface and various S species (Section 7.3.3). Please note that the BEs in this thesis are updated relative to the version of Paper 3 available at the time. The BEs in Paper 3 do not include dispersion corrections.

4 Applications of carbon materials

The chemical and structural malleability of carbon-based materials allows them to find applications in many areas. The two applications used in this thesis are polymer electrolyte membrane fuel cells (PEMFCs) and lithium-sulfur (Li-S) batteries. Being the application chosen for three of four papers, Li-S batteries are discussed in detail in this section. PEMFCs are discussed briefly here as well, but a more thorough analysis is given in a colleague's PhD thesis (Caroline Janson).[45]

For both applications, the goal of any carbon modification (doping or surface modification) was to increase some parameter of the device performance. However, this thought process can be reversed to re-focus the research question on the carbon material: what does the device performance say about the chosen modification? In this way, both PEMFCs and Li-S batteries can be considered as characterization techniques similar to those discussed in Section 4. In this mind set, devices can be made that probe a specific aspect or phenomenon of the application, even if it means lowering the overall performance. A good example of this are the Li-S batteries made without lithium nitrate ($LiNO_3$) in the electrolyte (Papers 2 and 4), which were made specifically to study the lithium polysulfide shuttle (LiPS shuttle, Section 4.1.4). Though these cells perform much worse than the corresponding ones with $LiNO_3$, the lack of this salt in the electrolyte allows the effect of the carbon modification on the LiPS shuttle to be studied directly. Commercially practical devices were never the goal of any study.

4.1 Lithium-sulfur (Li-S) batteries

4.1.1 Introduction to batteries

A battery is based on electrochemistry, specifically spontaneous electron transfer between an electron donor (D) and electron acceptor (A). Spontaneous, in this context, signifies that electron transfer will occur between the donor and acceptor if a viable pathway is available (*i.e.* the change in Gibbs Free Energy, ΔG, is negative). One such pathway results from putting the two in close proximity to each other; in other words, if the donor and acceptor are simply mixed together physically, sometimes with the aid of a liquid solvent, the spontaneous electron transfer occurs from the donor to the acceptor and the energy released manifests itself in the form of heat (Figure 4, left diagram). For the modern era, however, heat is not the desired form of energy, but rather electricity. The design of a battery is to allow the electron transfer to happen, but to force it to produce electricity; in this case, the viable electron transfer pathway is not direct physical contact between the donor and acceptor, but rather connecting them with an external electronic conductor (*i.e*. a metal wire). In this configuration, the negative charge carriers, the electrons, are allowed to flow through the conductor whereas the positive charge carriers, the ions, must travel a different path through the intervening electrolyte. No cations can travel through the wire just like no electrons can travel through the electrolyte. The separation of pathways for the negative and positive charges causes the production of electricity. After travelling their separate paths, the two types of charges recombine on the electron acceptor side of the cell. Using this configuration, some energy is still released as heat, but a sizeable portion is converted into the desired form of electricity (Figure 4, right diagram).

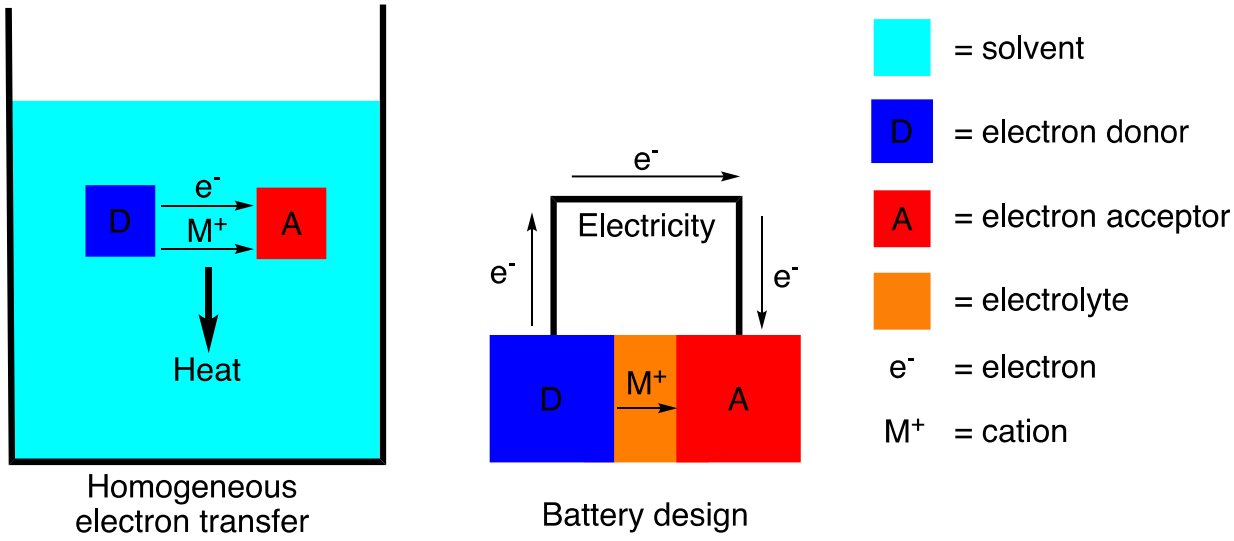

Figure 4. Comparison of homogeneous electron transfer (left) vs. battery design (right) between the donor (D) and acceptor (A). In homogenous electron transfer, both the electrons (e^-) and cations (M^+) travel the same path and the energy change, ΔG, is released as heat. In contrast, in the battery architecture, the electrons and cations take different paths and most of the energy is captured as electricity.

4.1.2 Common battery technologies

In the context of a battery, the electron donor is called the anode and the electron acceptor the cathode. The two halves of the cell are separated by the electrolyte. The circuit is completed by electronically connecting the anode and cathode with a wire. The first battery was invented by Volta in Italy in 1800 by piling zinc and silver disks together separated by a cloth soaked in a sodium chloride solution.[48] These constituted the anode, cathode, and electrolyte, respectively. Today, the basic battery concept is still the same, although with different materials for each component. Among the currently used technologies are lead acid, nickel metal hydride, and lithium-ion (Table 1). Lead acid batteries, invented in 1859, constitute the majority of the batteries today (> 80%) due to their low-cost, well-defined electrochemistry, relatively high voltage (2 V), and high recycle rate.[49] This wide-spread usage comes in spite of their modest capacities and heavy weight of their components. Nickel metal hydride (Ni-MH) batteries first appeared in Japan in 1990 as an alternative for nickel-cadmium and have found use as small, rechargeable cells.[50] Lithium-ion (Li-ion) batteries were patented in 1990 and have revolutionized the portable electronic devices market due to their high voltage and energy densities, low weight, and small size.[50]

However, even at their full theoretical capacity, Li-ion batteries exhibit an energy storage capability that is too low to meet the demands of several major markets including transportation and electrical grid storage.[51-54] Going beyond Li-ion batteries requires exploring anode and cathode materials with different electrochemistries. Li and O_2, as the anode and cathode respectively, would seem to fit the bill. As O_2 is "free" and doesn't contribute any significant weight, the Li-O_2 cell has its capacity based on Li alone. As shown in Table 1, the theoretical energy density of this cell is around 11586 Wh kg^{-1}, which is close to the energy density of gasoline (approximately 13000 Wh kg^{-1}). However, many severe problems plague this cell, which limit its prospects for the future.[55]

Table 1. Comparison of battery technologies

Technology	Capacity (mAh g^{-1})	Nominal voltage	Energy density (Wh kg^{-1})
Lead acid, ref [50]	65	2.0	170
Ni-MH, ref [49]	206	1.35	278
Li ion*, ref [49, 56]	200	3.4-3.8	720
Li-S‡, ref [57]	1675	2.15	2500
Li-O_2§, ref [50, 55]	3862	3.10	11586

*Based on $C_6Li + CoO_2 \leftrightarrow 6C + LiCoO_2$
‡Based on $16Li + S8 \leftrightarrow 8Li_2S$
§Based on $2Li + O_2 \leftrightarrow Li_2O_2$ (non-aqueous, mass of Li only)

4.1.3 The lithium-sulfur cell

An alternative system is the Li-S cell, in which the eponymous elements serve as the anode and cathode, respectively. The electrolyte consists of Li salts dissolved in organic solvents. The Li-S battery touts a theoretical energy capacity almost seven times higher than Li-ion cells and has inspired much research interest in the past few decades.[57] Besides its higher capacity and energy density, S has other distinct advantages including low cost, high abundance, and non-toxicity. However, many problems occur in this system, the majority of which stem from the insulating nature of S. Whereas elemental Li is a conductor, elemental S (octosulfur or S_8) is an excellent insulator (Table 2). To overcome this issue, conductive additives are used to "wire up" the S, thereby making it electrochemically accessible during battery cycling. This is where the aforementioned carbon materials come into the Li-S system (Figure 5). The addition of such electro-inactive materials, however, comes at a cost. In most of the cathodes described in the literature, the weight percent of S is typically below 60%, thereby lowering the overall electrode capacity. Even with the conductive additives, due to the insulating nature of S and its discharge products lithium disulfide (Li_2S_2) and lithium sulfide (Li_2S), most Li-S cells suffer from poor S utilization; in many cases, the percent of S used electrochemically is well below 70% during the first cycle and usually decreases with repeated cycling.

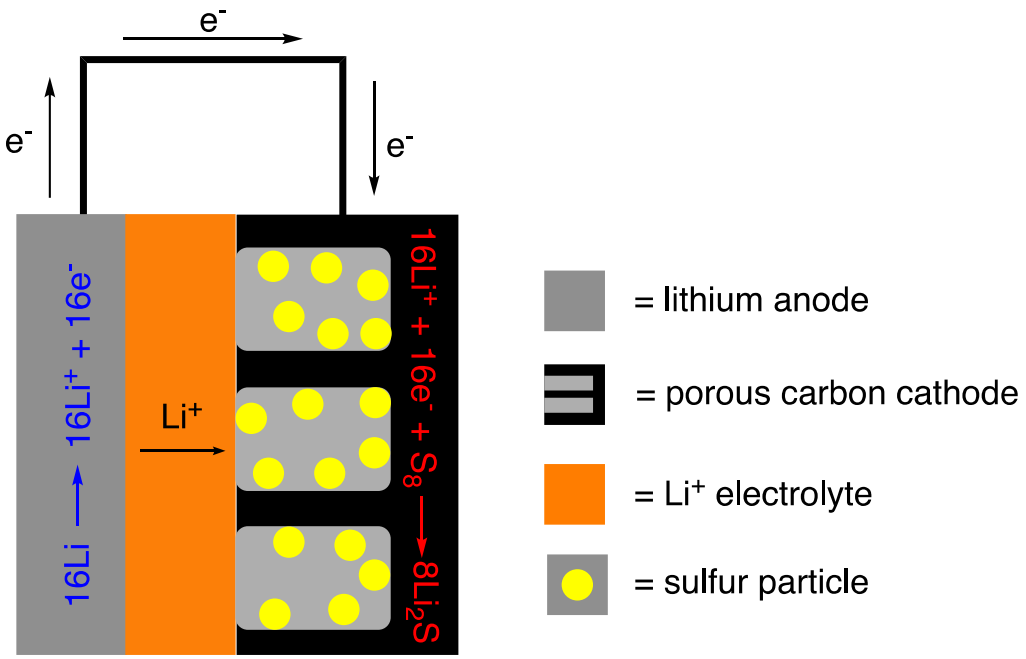

Figure 5. Illustration of a Li-S battery. One of the key components is the porous carbon, used as an additive to make the S conductive.

Table 2. Resistivities of some common elements.[58]

Material	Resistivity (Ω m)
Lithium	9.28×10^{-8}
Sulfur (S_8)	1.00×10^{15}
Copper	1.68×10^{-8}
Silicon	6.40×10^{2}
Carbon (amorphous)	$5.00 – 8.00 \times 10^{-4}$
Carbon (graphite)	$2.50 – 5.00 \times 10^{-6}$ (II basal plane) 3.00×10^{-3} (⊥ basal plane)

The dilution with carbon and underutilization of S are not the only problems associated with the Li-S cell. There is also a large volumetric change: upon complete discharge from S_8 to Li_2S, the volume increases by 80%. If sufficient space is not available, this expansion and contraction can break the carbon framework of the cathode, causing catastrophic battery failure. Additionally, the redox system that reversibly converts Li and S_8 to Li_2S, while seemingly simple, is actually quite complex (Figure 6). This process occurs through partially reduced S species called lithium polysulfides (LiPS), which have the composition Li_2S_n, where $4 \leq n \leq 8$. These LiPS are poorly characterized structurally and exist in rapid equilibrium in solution.[59] As the cell is discharged, the average LiPS chain length is reduced (n decreases) until solid Li_2S_2 and Li_2S is produced. In most of the conventional electrolytes, the starting and ending products are only sparingly soluble,[60-63] but the LiPS demonstrate a much higher solubility.[64] While a high solubility allows for better S utilization, it also permits the S to diffuse away from the electrode causing loss of active material and capacity fading. The polarity of the S species also changes dramatically as well: S_8 is covalent and non-polar, the LiPS are polar covalent, and the Li_2S_2 and Li_2S are ionic solids. Such drastic changes in volume, solubility, and polarity put stringent demands on the carbon host if it is to accommodate all S species effectively.

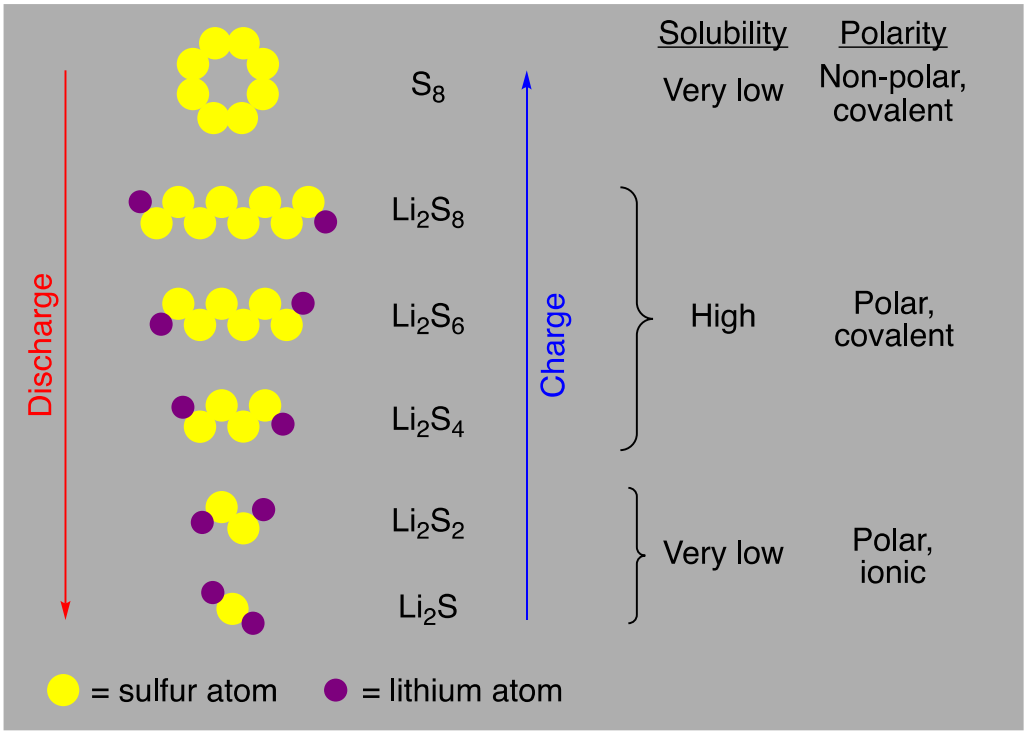

Figure 6. Illustration of the interconversion of S_8 to Li_2S during battery cycling. The complex electrochemistry is compounded with the drastic changes in solubilities, resulting in poor performing Li-S batteries despite their high theoretical capacities.

4.1.4 *The lithium polysulfide shuttle*

A special feature of Li-S batteries that merits its own section is the lithium polysulfide (LiPS shuttle). The LiPS shuttle manifests itself during the charging sequence of a Li-S battery and is due to the high solubility of the intermediate LiPS. During charging, Li_2S_2 and Li_2S are oxidized back to the soluble LiPS, which can diffuse to the Li anode, where they are partially reduced (*i.e.* n in Li_2S_n decreases). Still soluble, the reduced LiPS can diffuse back to the C-S cathode where they are partially re-oxidized (*i.e.* n in Li_2S_n increases). Overall, this back-and-forth movement of active material counteracts the applied current. A significant LiPS shuttle is clearly visible in the form of an extraordinarily long voltage plateau at *ca.* 2.35 V during the charging cycle that can last many times the theoretical maximum.[65] It should be emphasized that all charging above the maximum represents energy loss since, instead of charging the battery, it goes into powering the LiPS shuttle. Such long charging times reduce the Coulombic or charging efficiency (CE), which is the ratio of discharge over charge, to < 10%. Additionally, the LiPS shuttle was also linked to a fast self-discharge rate for Li-S cells[66] (see Section 7.4.4).

An important development in reducing the LiPS shuttle is the use of lithium nitrate ($LiNO_3$) in the battery electrolyte, which is discussed further in Section 4.1.7. A large part of this thesis goes into studying the LiPS shuttle; specifically, organic functional groups on the cathode surface were investigated for their ability to curtail the LiPS in place of electrolytic $LiNO_3$. Such tests are described in detail in Papers 2 and 4 (Sections 7.2 and 7.4).

4.1.5 *Sulfur impregnation*

In order to test a carbon in Li-S batteries, the carbon must undergo several processes to become a cathode. As shown in Figure 7, there are three major steps: S impregnation (this section), electrode fabrication (Section 4.1.6), and battery assembly with an electrolyte (Sections 4.1.7 and 4.1.8). Once the battery is made, it can be subjected to one of several tests (Section 4.1.9).

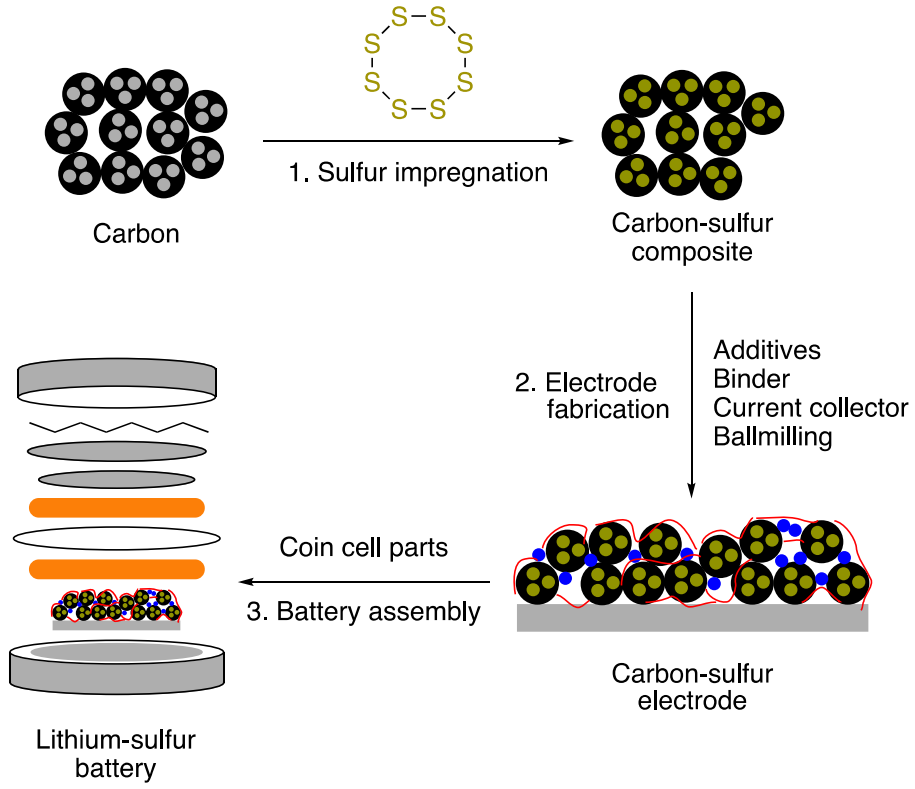

Figure 7. Overview of the processes employed in converting a carbon into a Li-S battery.

To incorporate S into the carbon host, a few impregnation methods exist.[67] This can happen either before electrode fabrication as shown in Figure 7, or the S can be added into the cell at a later point. In terms of the former, one of the main ways is to heat S_8 and the carbon together at the low viscosity point (155 °C)

of S_8 to infiltrate the active material into the carbon's pores.[68] In this thesis, this method is termed *melt diffusion*. While this procedure is simple, the high temperatures involved and reactive nature of liquid S_8 could potentially damage some of the features of the carbon, which was found in Paper 2 (see Section 7.2.2). In terms of the latter, another commonly used procedure is to incorporate the S active material into the electrolyte as soluble LiPS, typically Li_2S_8 in 0.2 to 1 M in concentration.[64] This type of electrolyte is called a *catholyte*, which is a portmanteau of the words "cathode" and "electrolyte." A catholyte avoids the high temperatures of melt diffusion and are typically quite easy to prepare from Li_2S and S_8 (1 to 7/8 molar ratio). However, its major downside is that, since all S is solubilized as LiPS in the electrolyte, the S active material initially starts in contact with Li anode. This causes deposition of S species on the Li anode and limits battery cycling. The catholyte method was used in Paper 2 (Section 7.2). The third method of S incorporation used in this thesis occurs after electrode fabrication and directly prior to battery assembly. It involves a LiPS solution too, but with subsequent evaporation of solvent. A small volume (10 µL) of a concentrated Li_2S_8 solution (1 M) was deposited onto a pre-made, pre-cut carbon cathode at 60 °C. The organic solvent dimethoxyethane (DME, see Section 4.1.7) easily evaporates leaving a residue of LiPS on the cathode. Termed *LiPS deposition*, this method was used in Papers 3 and 4 (Sections 7.3 and 7.4). Besides the moderate temperatures involved (compared to melt diffusion), LiPS deposition has the advantage of initially concentrating the LiPS near the cathode while a catholyte has them homogeneously dispersed, including in contact with the Li anode. LiPS deposition also allows for LiPS-free electrolytes to be studied.

4.1.6 Electrode fabrication

Electrode fabrication is the next step in the process, which can have drastic effects on the final battery performance; indeed, this procedure can have a larger impact on the electrochemical testing than the nature of the carbon itself. An otherwise well-performing carbon will yield subpar battery results if the electrode preparation is done poorly. In the case that the electrode preparation is extremely defective (*i.e.* the carbon falls off the Al foil current collector after drying) battery testing cannot proceed at all. Therefore, if the goal of the study is to determine the impact of the carbon modification on battery performance, then the electrode fabrication must be as simple and as reproducible as possible so as to minimize any effects of this procedure on the final battery performance.

Several procedures were tested for electrode composition, mixing methods and times, coating procedures, and electrode drying. The best, most reproducible procedure found was that detailed in Paper 2, which is summarized briefly here. First, the carbon is mixed into a slurry, forming a slurry with a paint-like consistency. In a typical slurry making process, the carbon is ball milled together with Vulcan and a polyvinylidene fluoride (PVDF) binder along with N-methyl-2-pyrrolidone (NMP) as the solvent/dispersant. The first three components are mixed in an 8:1:1 mass ratio, respectively, with extra NMP added to adjust the viscosity of the slurry (Table 3). The slurry should be homogeneously mixed with no visible particles and should have the consistency of paint. The slurry viscosity can be lowered by adding more NMP.

After the slurry is formed, it is poured onto highly polished Al foil on top of an auto-coater. With the aid of the auto-coater, a doctor blade is then pushed over the top of the slurry at a constant speed to coat the slurry with an even thickness (250 µm). The slurry is then left to dry first over night at room temperature, then 80 °C for 2 h in an air oven, then finally at 80 °C in vacuum for 1 h,if the carbon contains added S_8, or 16 h for carbons without added S_8. The shorter drying times in vacuum are to avoid excess S_8 evaporation at high temperatures and low pressures.

Table 3. Typical components of an electrode slurry

Component and description	Role in electrode	Weight percent
Carbon	This is the carbon material under investigation. This carbon could contain S, if melt diffusion was used previously.	80
Vulcan	Additional conductive additive; small carbon nanoparticles help electronically connect larger particles in the film.	10
PVDF Binder	Tethers carbon particles together, helps slurry adhere to the current collector.	10
NMP	Works as the solvent/dispersant for the slurry. The amount added must be adjusted according to the types of carbon used and amount of S in the carbon.	N/A

4.1.7 Battery electrolyte

A large volume of research in the Li-S battery field, and indeed in all battery research, is dedicated to the study of electrolytes. A short summary of battery electrolytes is given here. The electrolyte must meet several requirements including:

1. Provide fast ion (Li^+) transport
2. Form a solid-electrolyte interface (SEI), if applicable
3. Be sufficiently non-volatile for long-term cycling
4. Be cheap and environmentally benign
5. In the case of Li-S batteries, allow solvation of LiPS and facilitate S redox chemistry

Most electrolytes have three basic components: the solvent, which provides the medium for ion diffusion; a salt, which provides the ions for ionic conductivity; and additives, which are mixed with the electrolyte to improve battery performance. The solvents typical of Li-ion batteries such as alkyl carbonates are not applicable in Li-S cells due to reactions with radical LiPS.[59] Instead, the solvents for Li-S batteries are usually linear and cyclic acetals and ethers such as 1,3-dioxolane (DOL), 1,2-dimethoxyethane (DME), and tetraethylene glycol dimethyl ether (tetraglyme). A previous study[69] has shown that the linear DME provides higher LiPS solubility and reaction kinetics while the cyclic DOL forms a more stable SEI on the Li surface; therefore, using both solvents creates a synergetic effect and increased battery performance. Other, less volatile solvents, have also been employed in Li-S cells like ethyl methyl sulfone,[68] ionic liquids,[70] and equimolar Li salt – tetraglyme complexes.[71]

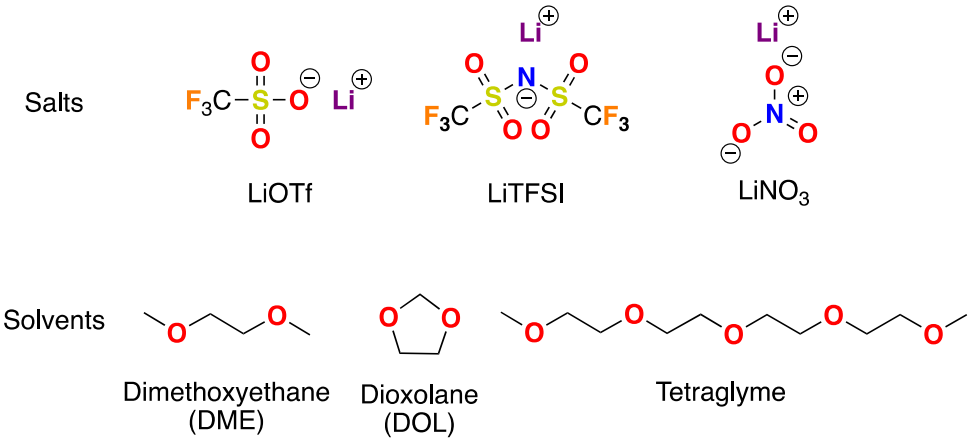

Figure 8. Chemical structures of common salts and solvents used in electrolytes for Li-S batteries

The Li salt is a central part of the electrolyte. It should be highly soluble in the solvent, provide fast Li^+ conduction, and be stable during cycling. Some of the classic Li-ion salts including lithium tetrafluoroborate ($LiBF_4$) and lithium hexafluorophosphate ($LiPF_6$) are not amenable to Li-S electrolytes due to reactions with the dissolved LiPS.[72] Two other soluble salts, lithium trifluoromethanesulfonate (LiOTf) and lithium bis(trifluoromethanesulfonyl)imide (LiTFSI) have been found to be the most suitable salts.[72] Of the two, LiTFSI is preferred because of its higher ionic conductivity and attenuated corrosion of the aluminum current collector.[73] A unique feature of Li-S battery salts is the possibility of dissolving the electroactive S material as a Li salt, namely LiPS. This was the concept of catholytes mentioned before (Section 4.1.5). Interestingly, the LiPS themselves can act as Li^+ conductors in the absence of other Li salts as shown in a recent study.[64] Such a development could obviate the need for fluorinated salts, thereby reducing the battery cost.

A key additive used in Li-S electrolytes is lithium nitrate ($LiNO_3$). A patent in 2008 revealed that by adding $LiNO_3$ to the electrolyte, the LiPS shuttle mechanism could be effectively stopped.[74] Consequently, these results have made $LiNO_3$ the single most important electrolyte additive and it is used in almost every Li-S publication after 2008.[75] The hypothesis was that the nitrate anions are reduced on the Li anode surface to Li_xNO_y, forming an SEI, which prevents anode reactions with dissolved LiPS.[76] This hypothesis, however, is being reexamined; an alternate role of the nitrate anions in the electrolyte is to act as oxidation catalysts for LiPS to S_8 within the proximity of the S cathode upon recharging.[75] Importantly, the use of $LiNO_3$ as an additive comes with a few notable downsides. Most importantly, nitrate is known to reduce on both the anode[75, 77-78] and cathode,[79-81] which makes its long term stability an issue. Because of its facile reduction, nitrate also limits the electrochemical stability window of the electrolyte with deeper discharges causing more irreversible reduction and an associated negative effect on the redox reversibility of the S cathode.[77, 82-83] $LiNO_3$, or the lack thereof, plays a key role in the Li-S batteries made in Papers 2 and 4 (Sections 7.2 and 7.4). All electrolytes used in this thesis are summarized in Table 4.

Table 4. Summary of electrolyte compositions used in this thesis. All concentrations are molar in 1:1 DOL-DME.

Electrolyte[a]	Li_2S_8	$LiNO_3$	LiTFSI	Used in Paper
1	0	0	1.0	2[b], 4
2	0	0.4	1.0	2[b], 3
3	0.2	0.4	0	2
4	0.2	0	0.4	2

a Electrolyte numbers correspond to those used in Paper 2 (SI).
b Only used for cyclic voltammetry (CV)

4.1.8 Battery fabrication

The ultimate test for a new carbon material is to test it as an electrode in a Li-S battery. The process continues from the electrode into a full cell. While in the glovebox, the electrode is built into a so-called "coin cell" whose components are shown in Figure 9. The relative sizes of the components are important, such that the S cathode becomes the limiting factor in this cell (*i.e*. Li should be in excess). To accomplish this, the cathode has the smallest diameter (13 mm) while the Li anode is slightly larger (14 mm). The separator is the largest of them all (16 mm), to minimize the risk of short-circuiting. Enough electrolyte is used (30-40 µL) to ensure that the cell is not limited by this component either.

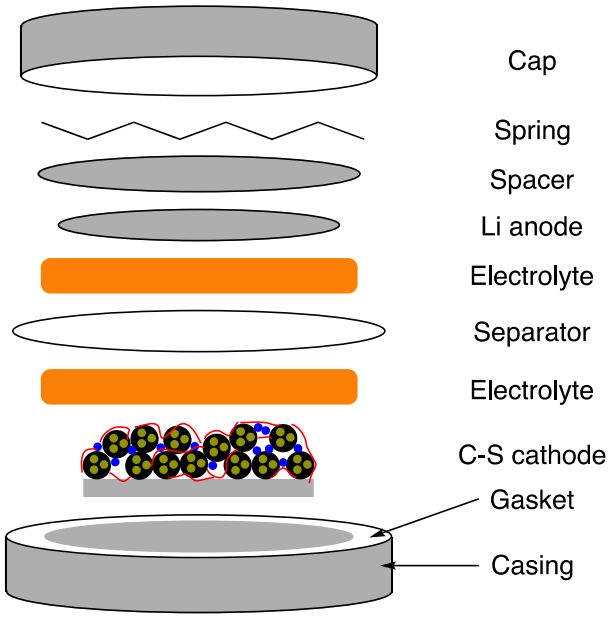

Figure 9. Construction of a Li-S coin cell with the component parts. The relative diameters of each component are taken into account.

4.1.9 Battery testing

Once made into a coin cell, a testing program can be applied to it. Several testing procedures exist including CV (Section 3.4.1) and EIS (Section 3.4.3), which can be combined together or with other techniques. The technique discussed in this section is called galvanostatic or constant current (CC) testing. As its name implies, current is drawn from the coin cell at a constant rate and the voltage is measured as the dependent variable. The current is applied until a pre-determined cut-off voltage is reached and the direction of the current is reversed. The process is the same going the other direction until the other cut-off voltage is reached and the current is again reversed. Since the current is constant with respect to time, the x-axis can be either time (hours) or charge passed into or out of the cell (mAh g^{-1}). The latter is usually preferred to determine the performance of the cell.

The amount of current applied to cell can be measured in a few ways. Many battery studies report applied current as a "C-rate." The C-rate takes into account the theoretical capacity of the electroactive material and applies a current such that it is (theoretically) 100% charged or discharged in a certain amount of time. A rate corresponding to 1C means that the battery should be completely (dis)charged in 1 hour; a rate of 5C corresponds to 1/5 of an hour or 12 minutes; a rate of 0.1 C or C/10 ("C over 10") corresponds to 10 hours. The theoretical capacity for elemental S is based on its mass and two electrons per S atom, which is calculated to be 1675 mAh g^{-1}. Therefore, a rate of 0.1C corresponds to 167.5 mA per g S. A common S loading for coin cells in this thesis was 2.56 mg, meaning that a current of 0.428 mA at 0.1 C was applied to the cell.

Battery testing was performed either on a 580 Battery Tester System from Scribner Associates or a Neware battery tester. In the context of this thesis, two main CC programs were employed. The first was 0.1C cycling for 50-150 cycles and the second was rate testing at 0.1, 0.2, 0.5, 1, and 0.1 C (10 cycles each). All cycling used 1.8 and 2.6 as the voltage cut-offs and were initially discharged from OCV (typically around 2.1 V) to 1.8 V. Battery testing constitutes a major portion of this thesis (Section 7).

4.2 Proton exchange membrane fuel cells (PEMFC)

Another field in which carbon materials have found extensive use is fuel cells. A fuel cell shares many characteristics with a battery. A fuel cell also contains an anode and cathode, which are separated by an ionically conducting electrolyte. However, unlike most batteries where the amount redox active material is

fixed (*i.e.* no material leaves or enters the cell), in a fuel cell, the electroactive materials, the fuels, are pumped in on either side and the discharge products, the exhaust, are removed. The electrons and cations are separated from each other on the anode side and the electrons travel the external circuit while the cations traverse the electrolyte. The charges recombine on the cathode side where they form the discharge product. This produces electricity, which can be drawn from the cell.

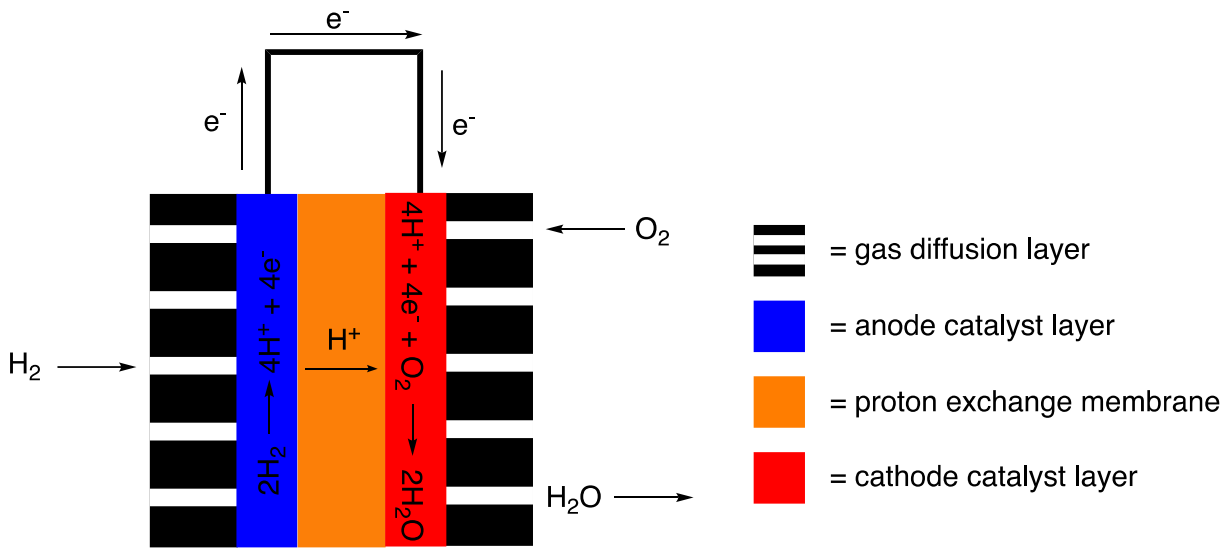

Figure 10. Illustration of a proton exchange membrane fuel cell (PEMFC).

The type of fuel cell employed in this thesis is the most common type of fuel cell, the PEMFC.[84-85] PEMFC can stand for either polymer electrolyte membrane fuel cell or proton exchange membrane fuel cell. The fuel for this type of cell can be hydrogen, methanol, ethanol, formic acid, or dimethyl ether on the anode side and O_2 is the most common oxidant on the cathode side. The PEMFC utilizing hydrogen (H_2) as the fuel is the most commonly encountered type of cell. On the anode side, H_2 is the electron donor and is split into electrons and protons (Equation 7). The electrolyte, as the two PEMFC names imply, consists of an acidic, water-based polymeric membrane; protons (H^+) are the positive charge carriers in this cell, similar to Li^+ in the Li-S system. The H^+ diffuse through the polymer electrolyte membrane while the electrons travel the external circuit. On the cathode side, O_2 acts as the electron acceptor and, together with protons from the electrolyte, forms two molecules of water (Equation 8). The overall reaction is shown in Equation 9.

$$2H_2 \rightarrow 4H^+ + 4e^- \tag{7}$$

$$4H^+ + 4e^- + O_2 \rightarrow 2H_2O \tag{8}$$

$$2H_2 + O_2 \rightarrow 2H_2O \tag{9}$$

The anode reaction is referred to as the hydrogen oxidation reaction (HOR) and the cathode reaction is referred to as the oxygen reduction reaction (ORR). It must be stressed that the overall PEMFC reaction is no different than the direct combustion of H_2 in the presence of O_2. However, since a PEMFC directly converts the chemical energy into electrical energy, the efficiency is much higher. By comparison, a combustion engine first converts the chemical energy to thermal energy, then to mechanical energy, then finally to electrical energy. With each step, energy is lost in the form of heat. Under ideal conditions, a fuel cell fed by pure H_2 and O_2 could reach an ideal efficiency of 83% (Equation 10).[84]

$$\eta_{ideal} = \frac{\Delta G_{ideal}}{\Delta H_{ideal}} = \frac{-237.2\ {}^{kJ}/_{mol}}{-285.9\ {}^{kJ}/_{mol}} = 0.83 = 83\% \tag{10}$$

Calculations have shown that a real fuel cell could reach efficiencies of up to 54%, with real life fuel cells having performances reaching 36%. This can be compared to an electric car, for which electricity has been produced from natural gas, where the overall conversion efficiency is about 24%.[85-86] Overall, the efficiency of any fuel cell can be calculated from its operating voltage (E_{cell}) as compared to its ideal voltage (E_{ideal}, Equation 11):

$$\eta = \frac{\Delta G_{cell}}{\Delta H_{ideal}} = \frac{-nFE_{cell}}{\Delta G_{ideal}/_{0.83}} = \frac{-0.83nFE_{cell}}{-nFE_{ideal}} = \frac{0.83E_{cell}}{E_{ideal}} \quad (11)$$

η = efficiency (unitless)
ΔG = change in Gibbs free energy (kJ mol^{-1})
ΔH = change in enthalpy (kJ mol^{-1})
n = number of electrons transferred (mol)
F = Faraday constant (96485 C mol^{-1})
E_{cell} = actual cell voltage during operation (V)
E_{ideal} = thermodynamic cell voltage (V)

In the case of both the HOR and ORR, the reaction does not proceed perfectly. While the theoretical or thermodynamic voltage (E_{ideal}) is 1.23 V, in practice, the cell voltage (E_{cell}) is measurably less (typically at 0.50-0.85 V). This loss in voltage exists because some of it is needed to drive both reactions to occur at a reasonable rate; indeed, as the reaction proceeds more quickly (*i.e.* more current is drawn from the cell), the voltage drop is greater (Figure 11). To attenuate this loss, catalysts are employed in both the anode and cathode. Platinum is the typical catalyst used for both reactions, but its cost and scarcity point to a need to develop cheaper, more abundant catalysts. Of the two reactions, the HOR is simpler since fewer bonds are broken and formed and only very small amounts of Pt are needed for efficient catalysis. Figure 12 shows that the voltage losses, or polarizations, are minimal from the HOR.

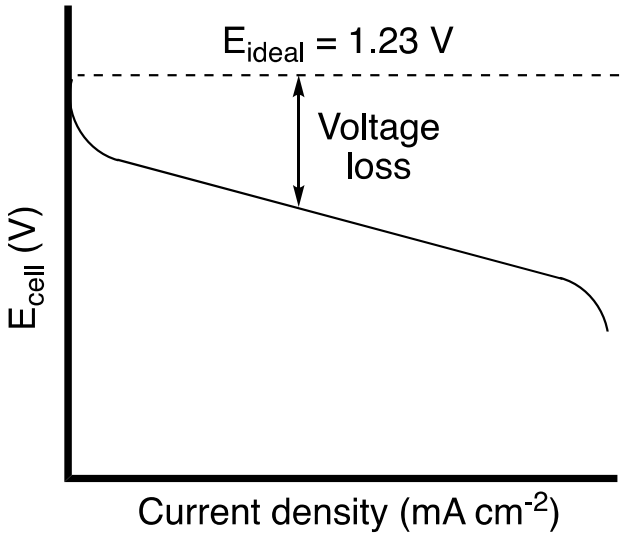

Figure 11. Illustration of ideal and actual fuel cell voltage and current characteristics. As more current is drawn from the cell, the voltage loss is greater.

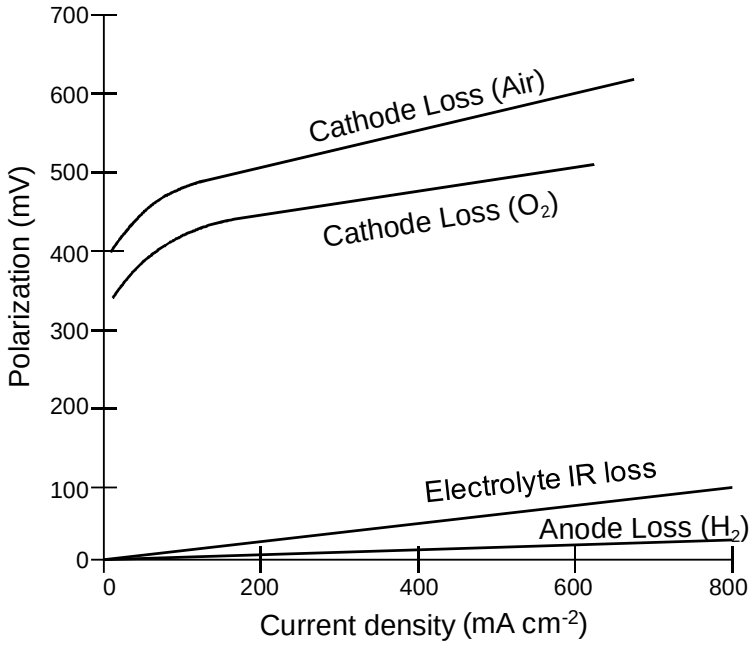

Figure 12. Contributions to the voltage loss (polarization) in a PEMFC. The majority of this loss comes from the cathode and the ORR, with smaller contributions from the electrolyte IR drop and HOR anode reaction.[85]

In the case of the ORR, the polarization is significantly higher and is the major contributor to the voltage losses in a PEMFC. Thus, a significant amount of research in this field focuses on how to minimize the voltage loss on the cathode side by catalyzing the ORR. Carbon materials, with their variable compositions, high surface area, and porous structures are well suited for this task. In a landmark study, it was found that N-doped carbon nanotubes efficiently catalyze the ORR.[87] The advantage of these carbons stems from that their synthesis uses strictly Earth-abundant elements. Additionally, various studies have found that co-doping carbons with both N and transitions metals (*e.g.* Fe, Co) could also enhance their activity towards the ORR.[26, 88]

PEMFCs tests were done in a single cell fuel cell, using a commercial 5 cm^2 PEMFC from Scribner Assoc. at 80 °C. In the context of this thesis, PEMFCs were used to test the ORR activity of the Fe-OMCs (Section 5.4).

5 Synthesis of iron/nitrogen-doped ordered mesoporous carbons using soluble iron salts for applications in PEM fuel cells

In lieu of a typical Results and Discussion section, the results in this thesis will be divided into three main sections. The first section (Section 5) discusses Paper 1 and the efforts into synthesizing Fe/N-doped ordered mesoporous carbons (Fe-OMCs) using four Fe salts and their applications in catalyzing the oxygen reduction reaction (ORR). The second section (Section 6) details how a variety of surface-bound organic functional groups can be bonded to the carbon surface using bromomethylation and the third section (Section 7) uses some of the functionalized carbon materials as cathodes in Li-S batteries. In this way, the bromomethylation results across three papers (Papers 2-4) can be compared directly and likewise with the battery data. The graphs and sample names between this thesis and the corresponding paper are the same with the exception of Section 6. In this section, some of the combined synthesis results from Papers 2-4 use different color-coding schemes and labels in an effort to distinguish among all samples.

5.1 Synthesis of iron/nitrogen-doped ordered mesoporous carbons (Fe-OMC)

The motivation behind Paper 1 stems from a 2013 paper into doping of carbon materials using transition metal (Fe, Co) salts for use in polymer electrolyte membrane fuel cells (PEMFCs, Section 4.2). One of the main goals of the current study was to increase the Fe levels in the resultant Fe-OMC which, in turn, should hopefully increase their performance. In other words, a higher Fe content should lead to more Fe-centered active sites for the ORR thereby increasing the efficiency of the Fe-OMC cathode. Many factors could plausibly affect the formation of Fe-centered active sites in an Fe-OMC including the synthesis temperature, the template, the Fe salt, and the type of carbon precursor and how many coordinating atoms it contains (*e.g.* N, O, S). Indeed, work from a colleague shows that even the hydration state of the Fe salt ($FeCl_3$ *vs.* $FeCl_3$-$6H_2O$) can have a noticeable impact on the Fe-OMC's ORR activity.[89]

The factor studied herein is the counter anion to the Fe cation of the Fe salt. The anion, while secondary to the desired Fe cation, can presumably influence the resultant Fe-OMC in at least two major ways: the solubility of the salt in the carbon precursor solution and adding new dopants to the Fe-OMC. With respect to former, a well-known "trick" in transition metal chemistry to increase the solubility of metal cation is to use a weakly coordinating anion such as trifluoromethanesulfonate (OTf^-), tetrafluoroborate (BF_4^-), or hexafluorophosphate (PF_6^-). If higher solubilities in the carbon precursor turn out to lead directly to higher Fe loadings, using such a salt could potentially be a facile pathway to increase the Fe-OMC ORR activity. With respect to the latter, under the high temperatures of carbon synthesis (500-1200 °C), the anion could, in principle, undergo many reactions: it could carbonize along with the carbon precursor if it contains sufficiently high levels of carbon (*e.g.* acetate (OAc^-), cyclopentadienyl (Cp^-)); it could decompose, forming a gaseous product, and escape from the carbonizing mixture (*e.g.* NO_3^- to NO_x, $C_2O_4^{2-}$ to CO and CO_2); or if it cannot carbonize or leave the precursor mixture, it could be incorporated into the Fe-OMC structure as an additional dopant. Overall, the choice of the anion in the Fe salt could lead to drastic differences in the resultant Fe-OMC.

While one study exists that compares directly $FeCl_3$-$6H_2O$ to ferrocene (Cp_2Fe), the organometallic nature of ferrocene makes this comparison more about inorganic *vs.* organometallic Fe instead of a direct comparison of Fe salts with various anions. In the present study, four Fe salts were selected with distinct anions (detailed below). The carbon precursor was furfurylamine (FA) with cubic ordered mesoporous silica KIT-6 as the template.[12]

1. Iron(III) chloride hexahydrate ($FeCl_3$-$6H_2O$) as the reference dopant salt.[89]
2. Iron(II) tetrafluoroborate hexahydrate ($Fe(BF_4)_2$-$6H_2O$) as a lipophilic anion without carbon.
3. Iron(II) trifluoromethanesulfonate ($Fe(OTf)_2$) as a lipophilic anion with carbon.

4. Iron(II) acetate ($Fe(OAc)_2$) as an organic anion without any additional elements (*i.e.* H, C, and O are already in the FA carbon precursor).

To distinguish among the samples, the Fe-OMCs are designated by their anion; for instance, the Fe-OMC derived from $Fe(OTf)_2$ is referred to as OTf-Fe-OMC. References to the salts themselves use their full names.

When dissolved in the FA carbon precursor, as expected, $Fe(BF_4)_2$-$6H_2O$, $Fe(OTf)_2$, and $Fe(OAc)_2$ all show greatly increased solubilities in the FA carbon precursor relative to the $FeCl_3$-$6H_2O$ reference dopant (5-7 times, Table 5). These solutions are nearly black due to the high concentrations of Fe cations whereas the reference dopant only turns the FA slightly brown. All Fe-OMC samples were prepared as detailed in Paper 1.

Table 5. Solubilities of Fe salts in furfurylamine (FA)

Fe salt	Approximate saturation limit		
	g L^{-1}	mol L^{-1}	Fe:FA molar ratio
$Fe(OAc)_2$	300	1.72	1:6
$FeCl_3$-$6H_2O$	60	0.22	1:43
$Fe(BF_4)_2$-$6H_2O$	430	1.27	1:7
$Fe(OTf)_2$	440	1.24	1:8

5.2 Determination of Fe-OMC elemental composition

To determine if the Fe levels were indeed increased, the Fe-OMCs were subjected to analysis with EA (Section 3.1.1), XRF (Section 3.1.2), and TGA (Section 3.3.1). TGA, although not an elemental technique *per se*, can be used as such if an appropriate program is chosen. In other words, by exposing the Fe-OMC to air at high temperatures (900 °C), the TGA program can mimic the combustion process in EA. The main additional datum that such a TGA program can give is the residual mass after combustion, which, importantly, EA cannot directly detect; in EA, both non-combustible solid masses and non-detectable volatile gases are not differentiated. Additionally, TGA allows for the water (hydration) mass to be determined, which also helps to increase the accuracy of the H content of the Fe-OMC (H is quantified as H_2O in EA). The overall formula is shown below and the corresponding data are summarized in Table 10.

$$100\% = Mass\ H_2O + Mass\ HCNS + \ Residual\ mass + Other\ volatiles \qquad (12)$$

The H, C, N, and S masses were determined by EA and the H_2O (hydration) and residual masses were determined with TGA. The hydration weight was taken as the mass loss at 150 °C while the residual mass was set as the remaining mass at the end of the 20 min isothermal treatment at 900 °C (Figure 13). Any remaining mass needed to reach 100 wt% is denoted other volatiles, which are undetectable by any of the techniques (*e.g.* O, Cl, F).

Table 6. Elemental and thermogravimetric analysis for Fe-OMCs.

Sample	$H_2O^{\#}$ (hydration)	H*	C*	N*	S*	Residual Mass#	Other volatiles
OAc-Fe-OMC	0.45	0.58	93.21	0.92	0.20	0.32	4.64
Cl-Fe-OMC	3.22	1.00	83.42	3.68	0.11	0.92	7.65
BF4-Fe-OMC	3.03	0.71	85.83	4.23	0.27	3.98	1.95
OTf-Fe-OMC	2.31	1.08	79.97	3.05	2.73	4.66	6.20

All units are weight percent.

* Determined by EA

Determined by TGA

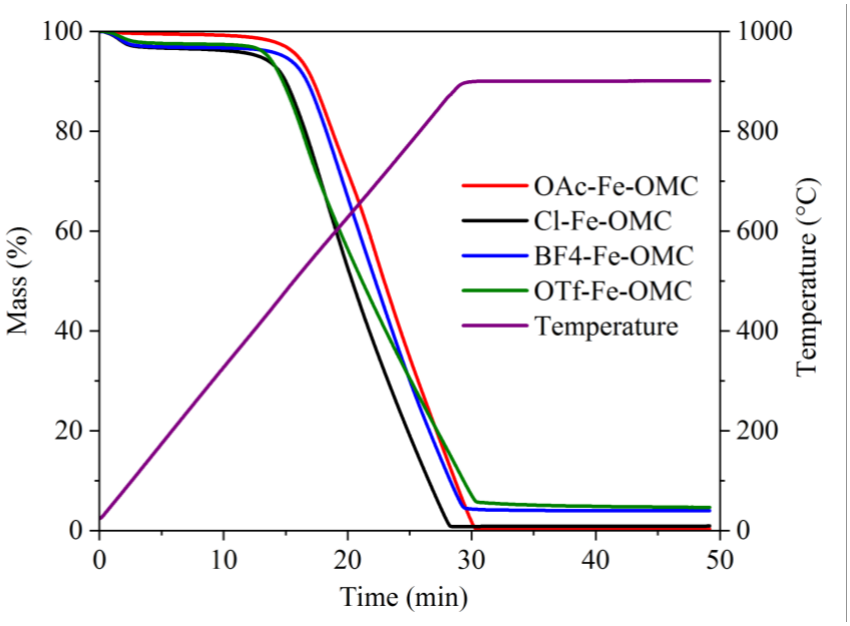

Figure 13. Thermograms for Fe-OMCs ran in air.

The use of XRF allows for the Fe content to be determined directly. All Fe mass was assumed to be entirely in the residual mass from TGA given that Fe and its oxide, Fe_2O_3, have melting points significantly above 900 °C (1538 °C and 1539 °C, respectively). As shown in the following equation, the difference between the residual mass and Fe mass was assumed to be other non-volatile elements (*e.g.* B). The corresponding data are shown in Table 7 while the elemental summary using all three techniques is displayed in Table 8.

$$Residual\ mass = Fe\ mass + Other\ nonvolatiles \tag{13}$$

Table 7. X-ray fluorescence and thermogravimetric analysis for Fe-OMCs.

Sample	Residual mass#	Fe§	Other non-volatiles
OAc-Fe-OMC	0.32	0.11	0.21
Cl-Fe-OMC	0.92	0.40	0.52
BF4-Fe-OMC	3.98	0.46	3.52
OTf-Fe-OMC	4.66	3.88	0.78

All units are weight percent.
Determined by TGA
§ Determined by XRF

Table 8. Elemental summary for Fe-OMCs.

Sample	$H_2O^{\#}$ (hydration)	H*	C*	N*	S*	Fe§	Other non-volatiles#,§	Other volatiles
OAc-Fe-OMC	0.45	0.58	93.21	0.92	0.20	0.11	0.21	4.64
Cl-Fe-OMC	3.22	1.00	83.42	3.68	0.11	0.40	0.52	7.65
BF4-Fe-OMC	3.03	0.71	85.83	4.23	0.27	0.46	3.52	1.95
OTf-Fe-OMC	2.31	1.08	79.97	3.05	2.73	3.88	0.78	6.20

All units are weight percent (wt%)
Determined by TGA
* Determined by EA
§ Determined by XRF

From the elemental summary, a few key differences appear. First and foremost, a high Fe content appears to have been achieved for OTf-Fe-OMC at nearly 4 wt%, or almost 10x higher than the reference Cl-Fe-OMC.

This large increase shows that, at least sometimes, a higher solubility in the precursor salt can lead to higher Fe loadings. Curiously, however, the other two Fe-OMCs synthesized with soluble salts, BF4-Fe-OMC and OAc-Fe-OMC, show that final Fe loading is not always correlated with solubility since similar (0.46 wt%) and lower (0.11 wt%) Fe contents relative to the Cl-Fe-OMC control were determined. The noticeably lower N doping of OAc-Fe-OMC correlates to its much lower Fe content, which is consistent with the ligating atoms being necessary for ORR active sites (*i.e.* Fe-N_x chelates). The hydration weight for OAc-Fe-OMC is also markedly lower likely indicating that both N and Fe doping make the carbon material more hydrophilic.

A few other notable differences appear, one of which is the high S content of OTf-Fe-OMC. While all Fe-OMCs had some S, which could be due to the post-carbonization treatment with H_2SO_4, OTf-Fe-OMC has a S content nearly 10x higher at *ca.* 2.7%. This additional S likely comes from the OTf^- anions, which could plausibly carbonize along with FA during the Fe-OMC synthesis. Since this Fe-OMC also has a much higher Fe content but similar N levels to BF4-Fe-OMC and Cl-Fe-OMC, it is possible that some of the extra Fe is associated, at least partially, with S as Fe sulfide species ($Fe_{1-x}S$). Another significant difference is for BF4-Fe-OMC, which had a noticeably higher concentration of other non-volatiles. This is likely due to the BF_4^- anions since the residual mass from TGA was observed to be amorphous and brown. Unfortunately, this mass adhered to strongly to the crucible for further analysis.

Interestingly, the residual mass derived from OTf-Fe-OMC was an orange-red powder, which was amenable for analysis with XRD (Figure 14). The diffractogram is consistent with Fe_2O_3, which would be expected from combustion of Fe-N_x and/or $Fe_{1-x}S$ at high temperatures. Knowing the chemical identity of the residual mass allows for a second method of determining the Fe content of OTf-Fe-OMC, which is calculated to be 3.26 wt%. While this value is a bit below that determined with XRF (3.88 wt%), both measurements demonstrate that OTf-Fe-OMC has a significantly higher Fe content than any of the other Fe-OMCs.

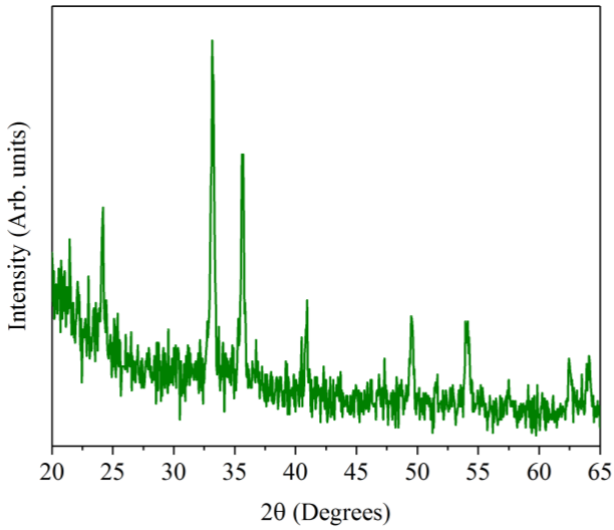

Figure 14. X-ray diffractogram of the residual mass of OTf-Fe-OMC after treatment at 900 °C in air for 20 min (TGA, see Figure 13). The diffraction peaks are consistent with Fe_2O_3.

In summary, by using a combination of TGA, XRF, and EA, the elemental compositions of all Fe-OMCs can be quantified reasonably well. The effect of the anion is apparent in these all Fe-OMC compositions, but most notably in the high Fe content of OTf-Fe-OMC.

5.3 Further Fe-OMC characterization

Before being subjected to electrochemical analysis, the Fe-OMCs were first studied by nitrogen-sorption, SAXS, and XRD to gain insight into the effect of the anion on the carbon's porosity, surface area, meso- and atomic structure. The nitrogen isotherms show clearly the impact of the Fe salt on the porosity of the carbon (Figure 15a and Table 9). Although all samples had similar BJH pore volumes, Cl-Fe-OMC has a much higher BET surface area. This could indicate that higher Fe salt concentrations lead to lower specific surface areas,

although the reason for this correlation is unknown. All four Fe-OMCs show Type IV isotherms, but only three of these (all except OAc-Fe-OMC) show a steep increase in nitrogen adsorbed over small pressure changes, which results from large numbers of pores with similar pore diameters. This difference is reflected in the pore diameter distributions (Figure 15b), in which these Fe-OMCs have well-defined maxima in the order Cl-Fe-OMC < OTf-Fe-OMC < BF4-Fe-OMC. In contrast, OAc-Fe-OMC has a very broad distribution with a shallow maximum at around 25 Å.

Table 9. Surface properties of the Fe-doped OMCs

Sample	BET surface area ($m^2\ g^{-1}$)	BJH pore volume ($cm^3\ g^{-1}$)*	Pore diameter maximum (Å)*
OAc-Fe-OMC	607	1.26	25
Cl-Fe-OMC	1035	1.29	41
BF4-Fe-OMC	572	1.19	60
OTf-Fe-OMC	709	1.02	52

*Based on the adsorption isotherm

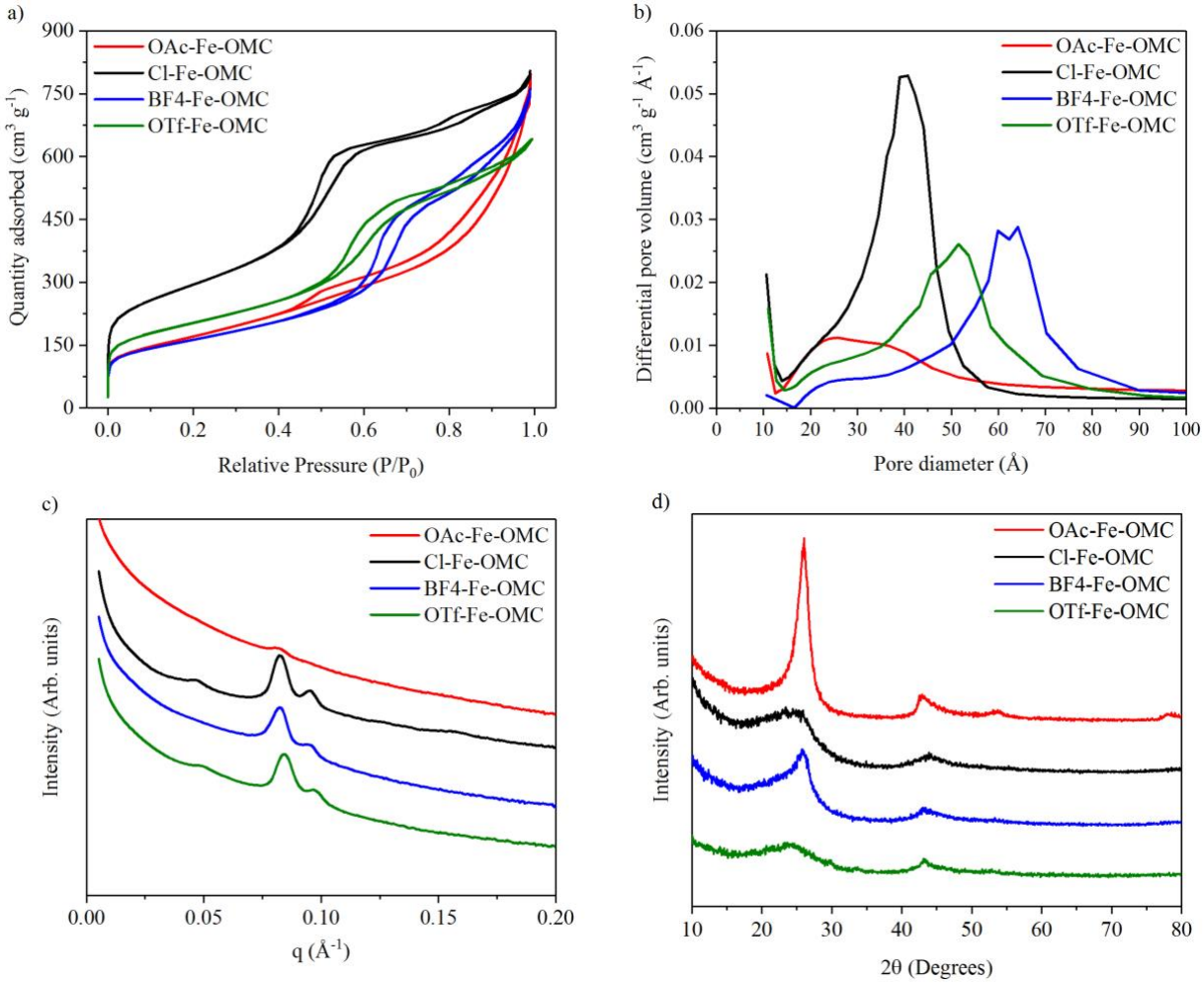

Figure 15. ***a)*** *Nitrogen isotherms,* ***b)*** *pore diameter distributions based on the adsorption isotherm,* ***c)*** *small angle X-ray scattering plots (SAXS), and* ***d)*** *X-ray diffractograms (XRD) for Fe-OMCs. In the SAXS and XRD plot, the traces have been offset in intensity for clarity.*

The SAXS patterns for the same triplet of Fe-OMCs are very similar (Figure 15c), which give a cubic *Ia3d* structure with the typical (211) and (220) reflections.[12] The lattice constants of Cl-Fe-OMC, OTf-Fe-OMC, and BF4-Fe-OMC are similar with values of 18.8, 18.7 and 18.3 nm, respectively. These sizes are consistent with the typical lattice sizes of cubic structures formed in OMCs using KIT-6 as a template. Again, distinct

from the rest, the SAXS pattern for OAc-Fe-OMC is very weak indicating a lack of order on the meso-scale. The X-ray diffractograms (Figure 15c) reveal that OAc-Fe-OMC is also the unique one. While all four samples show the expected peaks at 2θ values of 26° and 43°, corresponding to the reflections (002) and (101) of amorphous carbon,[8] the intensity of these peaks for OAc-Fe-OMC are markedly higher in addition to two additional reflections at 54° and 78°. BF4-Fe-OMC also shows more intense peaks at 26° and 43°, but less than OAc-Fe-OMC. Two very week diffraction peaks for OTf-Fe-OMC were observed between 30-35°, which could be due to some crystalline particles in the OTf-Fe-OMC sample. The high Fe and S content of this Fe-OMC suggests that these particles could be $Fe_{1-x}S$.[90]

Taken together, these data show that the OAc^- anion has a profound impact on the structure of OAc-Fe-OMC. The XRD results indicate a much more graphitic carbon as indicated by its sharp peaks. The higher degree of graphitization is consistent with its lower Fe and N loadings (Table 8), since this process is known to remove heteroatoms from the carbon structure.[8] The carbonizable OAc^- anion could facilitate graphitization and the high concentration of Fe cations could catalyze it. Apparently, graphitization also impacts strongly the meso-structure and ordered porosity of the material; both are thoroughly destroyed as evidenced by its weak SAXS pattern and broad pore diameter distributions.

5.4 Electrochemical performance of Fe-OMCs: PEMFCs and RDE

With their elemental and textural properties thoroughly characterized, the Fe-OMCs were fabricated into cathodes for use in PEMFCs (Section 4.2). The polarization plots from the PEMFCs are shown in Figure 16. In the low current density region, the reaction is kinetically controlled and Cl-Fe-OMC outperforms the other three. In the high current density region, mass transport of O_2 and H_2O exhaust becomes limiting and BF4-Fe-OMC and OTf-Fe-OMC slightly outperform Cl-Fe-OMC. Overall, despite its much higher Fe content, OTf-Fe-OMC does not perform noticeably better than the control Cl-Fe-OMC. OAc-Fe-OMC, on the other hand, performs much more poorly than the other three, which correlates well to its low levels of Fe and N since these elements are strongly associated with the active site itself and/or its formation.[15, 91-92] Overall, the performance of the other three Fe-OMCs is comparable and, therefore, are likely to contain similar concentrations of ORR active sites; the extra Fe contained in OTf-Fe-OMC is probably ORR inactive (see Section 5.5).

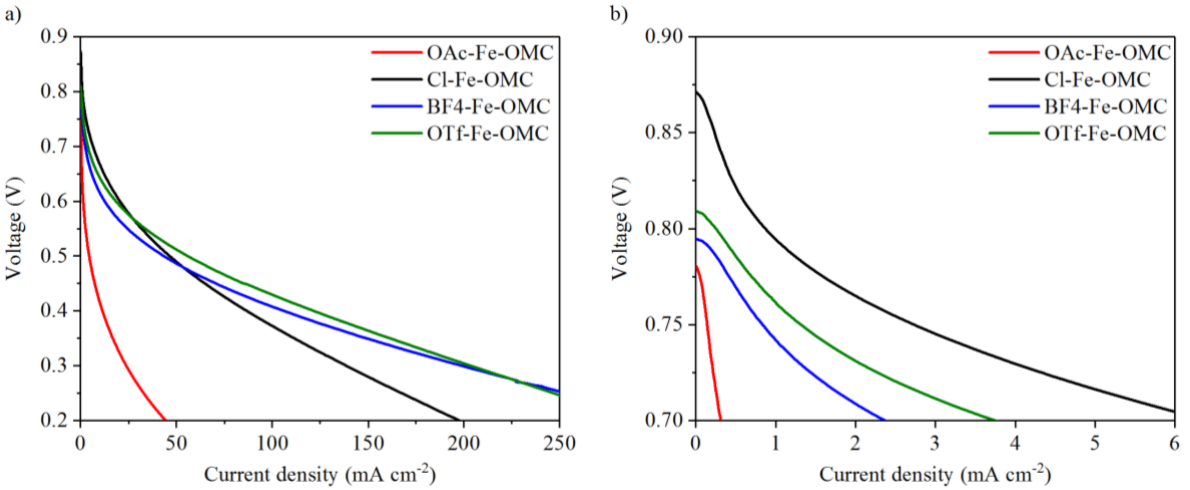

*Figure 16. **a)** Polarization curves and **b)** zoom in of low current density regions measured in a single cell PEM fuel cell for Fe-OMCs. Measured at 80 °C, 100% relative humidity, 1.5 bar backpressure on both electrodes, H_2 (100%) flow rate 100 mL min^{-1}, air flow rate 200 mL min^{-1}, Nafion membrane NRE-212 used, Fe-OMC loading on the cathode GDLs was about 1.6 mg/cm^2.*

To further study their ORR activities, the Fe-OMCs were used as working electrodes in rotating disc electrode experiments (RDE, Section 3.4.2). It is important to point out that, while PEMFCs and RDE are related in that they can both be used to test for ORR activity, they are fundamentally different experiments. PEMFCs are full cells run with an H_2 anode at 80 °C while RDE is a half cell with counter and reference

electrodes run without H_2 at 25 °C. The electrolytes of each are also distinct because an acidic polymer (Nafion) electrolyte is used in a PEMFC while in RDE aqueous electrolytes saturated with O_2 gas are used. Comprehensive RDE data and analysis can be found in the supporting information (SI) of Paper 1.

To mimic as closely as possible the acidic electrolyte of a PEMFC, the first RDE electrolyte chosen was O_2-saturated 0.1 M $HClO_4$ and the results are shown in Figure 17a. Cl-Fe-OMC shows the highest half-wave potential ($E_{1/2}$) at 0.68 V *vs.* RHE with OTf-Fe-OMC and BF4-Fe-OMC slightly lower at 0.62 V and 0.56 V, respectively. OAc-Fe-OMC faired much worse with an $E_{1/2}$ of 0.44 V, indicative of a high over-potential. The relative order of the $E_{1/2}$ match well with the relative performance at lower current densities in PEMFCs. From this similarity, it was determined that such RDE analysis is a better model for PEMFCs at lower current densities. The enhanced ORR performance of Cl-Fe-OMC could be due, at least in part, to its much higher BET surface area (Table 9).

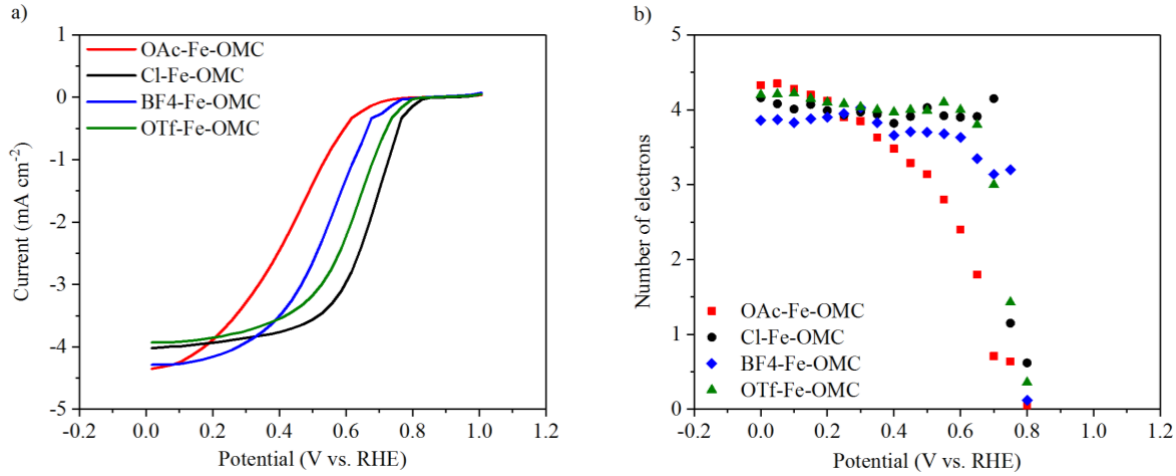

Figure 17. ***a)*** *Rotating Disk Electrode (RDE) polarization plots collected in O_2-saturated 0.1 M $HClO_4$ electrolyte at 10 mV s^{-1} with a rotation rate of 900 rpm at room temperature and* ***b)*** *number of electrons transferred for the Fe-OMC catalysts as determined by the Koutecky-Levich equation. At potentials greater than 0.8 V, the number of electrons transferred was determined to be zero for all Fe-OMC catalysts.*

The Koutecky-Levich equation was applied to the electrode current densities at different rotating rates in order to determine the number of transferred electrons per O_2 molecule as a function of applied potential (Figure 17b). From this calculation, it was determined that Cl-Fe-OMC, BF4-Fe-OMC, and OTf-Fe-OMC follow four-electron mechanisms from 0 to *ca.* 0.70 V, around which point the numbers drop precipitously to < 1. This similarity bears resemblance to their comparable performances in PEMFCs. Once again, OAc-Fe-OMC distinguishes itself from the other three, this time by following a different mechanism; the number of electrons transferred is lower for this Fe-OMC starting from 0.30 V and drops continuously thereafter. This indicates an incomplete ORR and the formation of H_2O_2 and/or other partially reduced O species. An incomplete ORR matches well to the poor performance of this catalyst in PEMFCs due to its lower N and Fe content.

A second RDE study was conducted in 0.1 M KOH, also with saturated O_2. Compared to the previous study with 0.1 M $HClO_4$, a measurable increase was recorded for all Fe-OMCs in terms of both the $E_{1/2}$ and the number of electrons transferred (Figure 18). The improved performance for all Fe-OMCs is likely due to reduced adsorption energies of anions in the basic environment, specifically of the hydrogen peroxide intermediate (HO_2^-), which reduces overpotentials for further electron transfer.[93-94] With an $E_{1/2}$ of 0.86 V, OTf-Fe-OMC barely outperforms Cl-Fe-OMC and BF4-Fe-OMC, which exhibit very similar $E_{1/2}$ of 0.845 V (Figure 18a). As before, the OAc-Fe-OMC performs the worst with an $E_{1/2}$ of 0.78 V. The number of electrons transferred is calculated to be about four for all Fe-OMCs from lower potentials until about 0.7 V (Figure 18b). At this voltage, the number decreases consistently for all catalysts with the OAc-Fe-OMC catalyst once again showing the lowest number at each potential between 0.7 – 0.9 V.

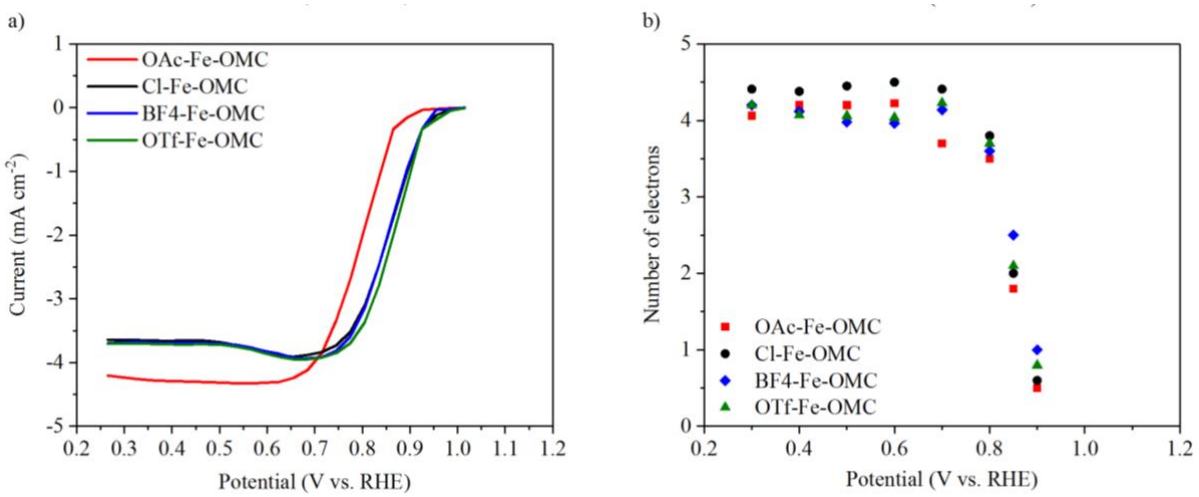

Figure 18. ***a)*** *Rotating Disk Electrode (RDE) polarization plots collected in O_2 saturated electrolyte 0.1 M KOH at 10 mV s^{-1} with rotation rate of 900 rpm at room temperature and* ***b)*** *number of electrons transferred for the Fe-OMC catalysts as determined as determined by the Koutecky-Levich equation. At potentials greater than 0.9 V, the number of electrons transferred was determined to be zero for all Fe-OMC catalysts.*

In summary, the electrochemical testing in both PEMFCs and RDE for Cl-Fe-OMC, BF4-Fe-OMC, and OTf-Fe-OMC proves to be very similar; only the performance of OAc-Fe-OMC was measurably worse. Given these performances, one can infer that, for the first three Fe-OMCs, the concentration of ORR active sites must be similar while the concentration in OAc-Fe-OMC is likely much lower. The low activity in the ORR correlates well to this Fe-OMC's low Fe and N contents (Table 8) and high level of graphitization (Figure 15d). In addition, its lack of order on the mesoscale (Figure 15c) and irregular pore structure (Figure 15b) could impede diffusion or reactants and products within the Fe-OMC structure, further lowering its ORR efficiency.

5.5 Insight into the Fe-OMC active site using electron paramagnetic resonance spectroscopy.

As a final test, electron paramagnetic resonance (EPR, Section 3.5.1) analysis was performed to gain insight into the Fe species contained within the Fe-OMCs. As EPR is not yet a common technique for characterizing carbon materials, a colleague, Dr. Caroline Janson, has spent a great deal of effort to understand which EPR signals correspond to which species and whether the signal arises from Fe or another paramagnetic source. Details corresponding to the background on EPR and its application for characterizing OMCs are given in Dr. Janson's PhD thesis.[45] In the present study, EPR was mainly used to determine the absence or presence of Fe in the Fe-OMC catalysts and to identify possible differences in types of Fe species contained within the samples.

In EPR, paramagnetic species, those with at least one unpaired electron, can be detected and sometimes quantified. Unpaired electrons can occur in Fe^{3+} and high spin Fe^{2+} species as well as in paramagnetic O species (*e.g.* O_2^-). If the ORR activity of the Fe-OMCs is indeed tied to an Fe-centered active site, the EPR signal of some Fe species is expected to change upon exposure to atmospheric O_2; for this reason, the samples were flushed with either pure N_2 or air before measurement. Additionally, EPR signals can be temperature dependent so the experiments were performed at two temperatures (295 K and 120 K). The spectra for all samples, temperatures, and atmospheres are collected in Figure 19.

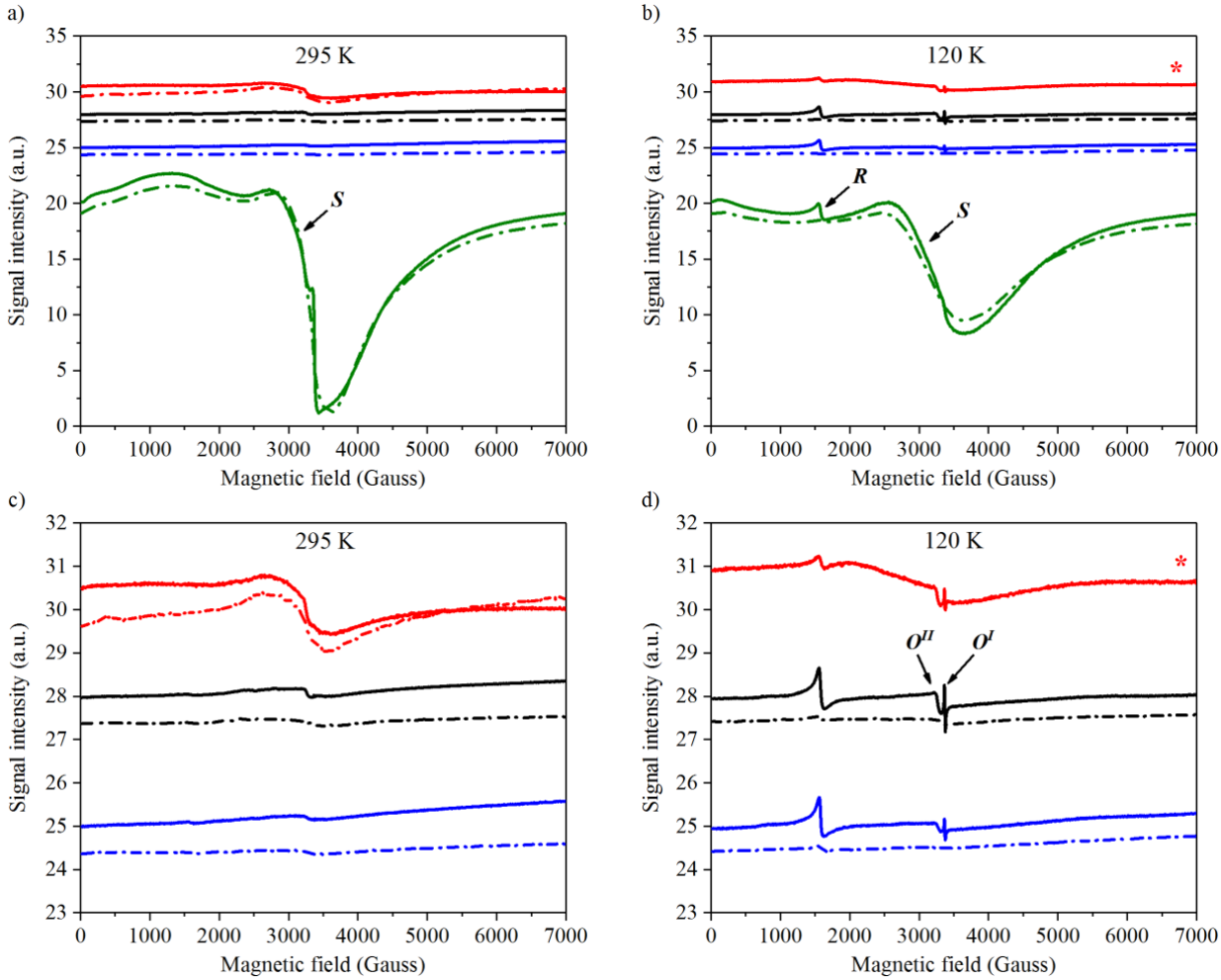

Figure 19. ***a)*** *Electron paramagnetic resonance (EPR) spectra measured at 295 K,* ***b)*** *EPR spectra at 120 K,* ***c)*** *zoom in of the spectra at 295 K, and* ***d)*** *zoom-in of spectra at 120 K for OAc-Fe-OMC (red), Cl-Fe-OMC (black), BF4-Fe-OMC (blue), and OTf-Fe-OMC (green). Spectra were taken either in air (solid line) or a nitrogen atmosphere (dotted line). The traces have been offset in intensity for clarity. *Sample OAc-Fe-OMC was not amenable for analysis in a nitrogen atmosphere at 120 K.*

For all Fe-OMC catalysts, EPR signals were observed which supports Fe incorporation into the carbonaceous structure as was determined by XRF (Table 8). However, noticeable distinctions among them lend evidence for a few types of Fe within the various Fe-OMC structures. Overall, the spectra obtained from Cl-Fe-OMC and BF4-Fe-OMC are similar, which is in line with their comparable electrochemical performance (Section 5.4). Thus, despite the much higher solubility of $Fe(BF_4)_2$-$6H_2O$ compared to $FeCl_3$-$6H_2O$ in the FA precursor solution, the resulting carbon materials end up being very similar from the perspective of EPR. The large loading of other non-volatiles (3.52 wt%, Table 8) contained within BF4-Fe-OMC, which likely result from the BF_4^- anions, apparently does not have a strong influence on Fe coordination. Instead, any variations in electrochemical performance between these two Fe-OMCs may be due to slight differences in their carbon structures, as shown in XRD and nitrogen-sorption (Figure 15).

By decreasing the temperature to 120 K in an air atmosphere, three EPR signals become apparent: one signal around 1500 G (g = 4.25) denoted ***R***, a sharp signal around ~3400 G (g = ~2.00) denoted $\boldsymbol{O^I}$, and a signal around ~3200 G (g = ~2.07) denoted $\boldsymbol{O^{II}}$. For all Fe-OMCs, the ***R*** signal is observed, but its amplitude is much smaller for OAc-Fe-OMC. Since this signal is typically attributed to a high spin Fe^{3+} in a rhombic structure,[94-97] its lower intensity in OAc-Fe-OMC is consistent with its lower Fe content and, consequently, lower ORR activity. Likewise, its similar intensity across the other three samples corroborates their comparable ORR activity.

When the sample is flushed with nitrogen, the ***R*** signal disappears. Such behavior is consistent with an EPR-silent Fe^{2+} center that is oxidized to EPR-active Fe^{3+} upon exposure to O_2. Coincidently, two more signals, ***O^{I}*** and ***O^{II}***, also arise when O_2 is present and disappear in its absence at 120 K. The ***O^{I}*** and ***O^{II}*** signals are assigned to an O radical (*e.g.* O_2^-) which is formed when O_2 oxidizes a Fe^{2+} species into Fe^{3+}.[98-99] Overall, the ***R***, ***O^{I}*** and ***O^{II}*** signals are believed to be related to the ORR active site, but this assignment has yet to be unambiguously confirmed.

Undoubtedly, the most deviating spectrum was recorded for OTf-Fe-OMC (green trace), which reveals an intense, broad spectrum between 2500 and 3500 G (Figure 19a and b, denoted ***S***). Contrary to the three previous signals, the ***S*** signal does not seem to be affected by a change in atmosphere while its intensity is lowered when the temperature is decreased from 295 K to 120 K. Because of its temperature-dependent behavior, the ***S*** signal is assigned to superparamagnetic particles.[100-101] The chemical identity of these particles could be $Fe_{1-x}S$[102-104] and/or Fe_2O_3,[100-101] since both are known to be super paramagnetic. The presence of such particles in OTf-Fe-OMC are consistent with both its weak diffraction peaks in XRD (Figure 15d) and the XRD of the combusted sample (Figure 14). The OAc-Fe-OMC also exhibits an ***S*** signal, albeit with lower intensity than in OTf-Fe-OMC, likely indicating a lower concentration of superparamagnetic particles in the former. Meanwhile, in BF4-Fe-OMC and Cl-Fe-OMC catalysts, no ***S*** signal was detectable, which suggests that these two catalysts lack this type of particle.

In light of the fact that OAc-Fe-OMC performed much worse in PEMFC and RDE tests than the other three, it is suggested that the Fe species responsible for the ***S*** signal is not related to any ORR activity; otherwise, OAc-Fe-OMC would be expected to show higher ORR activity given that it exhibited an ***S*** signal whereas BF4-Fe-OMC and Cl-Fe-OMC did not. Given the similar performance by BF4-Fe-OMC, Cl-Fe-OMC, and OTf-Fe-OMC, the extra Fe contained in OTf-Fe-OMC above the other two (3.88 wt% *vs. ca.* 0.40 wt%, Table 8) is likely ORR inactive superparamagnetic particles, which is responsible for the strong ***S*** signal in this Fe-OMC. Some amount of the ORR active Fe species must be present in OTf-Fe-OMC, however, based on its performance in PEMFC and RDE tests. Curiously, its ***O^{I}*** and ***O^{II}*** signals are missing, but these could be obscured by its large ***S*** signal, which occurs at the same place in the spectrum. Given this difference in signal intensity, it is believed that the majority of the large Fe loading in OTf-Fe-OMC arises from superparamagnetic particles (***S*** signal) while the ORR active Fe species (***O^{I}*** and ***O^{II}*** signals) is in lower concentration.

5.6 Conclusions from doping Fe-OMCs with highly soluble Fe salts

To summarize the findings in this study, the counter anion in the Fe salt has a significant impact on the synthesis and properties of Fe-OMCs. First of all, the solubility of the dopant Fe salt can be greatly enhanced in the FA carbon precursor by switching the anion from Cl^- to one more soluble in organic media including OAc^-, OTf^-, and BF_4^-. The higher concentration of Fe ions allows for a much higher Fe loading in OTf-Fe-OMC relative to Cl-Fe-OMC, but not so for BF4-Fe-OMC and OAc-Fe-OMC, which had similar and lower Fe loadings, respectively. Comprehensive elemental analysis shows that OAc-Fe-OMC has a lower N concentration, OTf-Fe-OMC has a much higher S loading, and BF4-Fe-OMC has a high concentration of unidentifiable non-volatile elements (*e.g.* B). Characterization *via* XRD, SAXS, and nitrogen-sorption reveal the much higher degree of graphitization in OAc-Fe-OMC, which leads to a lack of order on the mesoscale and a broad pore size distribution. The higher degree of graphitization also explains its lower N and Fe doping levels.

Most importantly, the higher Fe loading obtained for OTf-Fe-OMC does not translate into noticeable improvements in the ORR as measured by PEMFC and RDE experiments. Instead, it performs similarly to both BF4-Fe-OMC and the Cl-Fe-OMC control catalyst while OAc-Fe-OMC performs much worse. From this, it is deduced that the extra Fe contained in OTf-Fe-OMC over BF4-Fe-OMC and Cl-Fe-OMC is ORR inactive. To distinguish among different types of Fe contained with the Fe-OMC structures, EPR was performed. In OTf-Fe-OMC and, to a lesser extent, OAc-Fe-OMC, a broad signal is observed and is assigned to ORR inactive superparamagnetic particles. Three other signals are observed and are assigned to ORR active Fe-centered sites. Overall, these assignments are consistent with the relative Fe-OMC performances in the ORR.

Although the main goal of using soluble salts to increase the ORR efficiency was not achieved, these results highlight a potential opportunity to increase the catalytic activity of Fe-OMC: more of the inactive Fe contained in OTf-Fe-OMC could be changed into the ORR active type if some of the synthesis conditions changed favorably (*e.g.* the carbonization temperature, the Fe salt concentration, the carbon precursor, and the level of nitrogen doping). Since the Fe doping level and, consequently, its number of ORR active sites will always be limited by the solubility of the dopant salt, using soluble Fe sources has its distinct advantages. In all cases, however, more attention should be paid to the counter anion, given its large impact on the Fe-OMC properties.

6 Synthesis of diverse functional groups on carbon surfaces *via* bromomethylation and nucleophilic substitution

The two main methods of modifying carbon materials discussed in this thesis, heteroatom doping and surface modification, have distinct advantages and disadvantages. For surface modification, one of its underappreciated strengths is the relative ease with which the resultant carbon materials can be characterized. That is, by virtue of requiring much lower temperatures (25 – 110 °C) compared to the bottom-up method of carbon doping (950 °C), surface modification allows for much more accurate descriptions of the relevant surface groups since the atomic "scrambling" induced at carbonization temperatures is avoided. Indeed, a large portion of research into heteroatom doping of carbon materials for use in fuel cells focuses on identifying and characterizing the active site,[84] which was one of the goals of Paper 1 and its use of electron paramagnetic resonance (EPR) to gain insight into Fe-centered active sites of the Fe-OMCs (Section 5.5).

6.1 "Organic" chemistry: running organic chemistry reactions on carbon surfaces

The lower temperatures involved with surface modification of materials, specifically of carbon materials, bears resemblance to solution-phase organic chemistry. Many of the reactions discussed in this section are commonly performed in organic chemistry at the undergraduate level (*e.g*. electrophilic aromatic substitution, nucleophilic substitution).[105] The main difference is that, in this case, both the "reactants" and "products" are surface-bound organic functional groups. Because both are tied to the surface, characterization of the surface groups, despite being easier than heteroatom doping, is still a challenge relative to the corresponding small molecules in the solution phase. The increased difficulty is due to that the typical methods used by organic chemists to pinpoint the structure of small molecules, in particular Nuclear Magnetic Resonance (NMR), are not applicable for surface groups on carbon materials. This allows for some ambiguity when assigning absolute structures to the surface groups. However, the "silver lining" in this case is that, compared to many organic reactions, the purification of carbon materials is considerably simpler and is always the same: the functionalized carbons are simply vacuum filtered and washed with the appropriate solvents followed by drying in vacuum. No chromatographic columns or thin layer chromatography (TLC) is required!

Given the lack of NMR and similar organic chemistry techniques, accurately determining the structure and quantity of the surface groups on carbon becomes the highest priority. Competent organic chemists think about the purification scheme before setting up the reaction in order to simplify the purification process as much as possible; competent "organic" chemists think about possible surface group characterizations before setting up their reactions in order to unambiguously confirm their structure and concentration on the carbon surface. Such characterizations rely heavily on the elemental make-up of the carbon substrate, which usually contains large amounts of O and H in addition to the bulk carbon.[8] Therefore, should the surface groups contain other elements, their presence can be easily confirmed since many characterization techniques for solid materials can qualify and/or quantify the elemental content (*e.g.* EA, XRF, and XPS, Section 3.1). Other characterization methods, including nitrogen-sorption, SAXS, XRD, SEM, and CV (Sections 3.2 and 3.4), were used to determine the impact of surface modification on other properties of the carbon material.

In principle, any element besides H, C, and O can be used in this analysis, but, in practice, certain elements provide better characterization "handles" than others; these elements are those amenable for EA quantification (N and S, Section 3.1.1) or are heavy enough for reliable XRF quantification (Fe, Br, and I, Section 3.1.2). XPS (Section 3.1.3), since it can detect all elements except H, He, and Li and can determine their oxidization state and bonding arrangement, is perhaps the most powerful technique for surface group characterization. All of the surface groups synthesized *via* the two-step method of bromomethylation and nucleophilic substitution (*vide infra*) provide at least one of these elements to the carbon substrate.

6.2 Background on surface modification of carbons and bromomethylation

As mentioned in the Background (Section 2.3), there exist several ways to functionalize the surface of a given material and, for materials such as TiO_2, SiO_2, and gold, an efficient reaction or scheme to modify their surfaces has already been discovered. However, in the case of carbon materials, a standard method for functionalizing its surface has not been established.[37, 106-108] Indeed, the two main methods of modifying carbon surfaces, oxidation and diazonium salt grafting, have significant caveats including damage to the carbon structure in the former and multilayer formation in the latter. An alternative reaction (or series of reactions) to efficiently, mildly, and reproducibility functionalize the carbon surface in a monolayer fashion would therefore be of great utility to any application requiring the use of carbon materials.

Herein, we propose a two-step reaction scheme as a viable alternative to other methods for the surface functionalization of carbon materials. The first step is bromomethylation and the second step is nucleophilic substitution (Figure 20). One of the main advantages of this scheme is the elemental composition of the surface groups, which allows for efficient "organic" chemistry as detailed in the last section; the use of bromomethyl groups in the first step combined with N-, S-, or halide-based nucleophiles in the second step allow for accurate determination of the surface group structures and loadings at each stage of the synthesis. The mild conditions of both reactions also prevent degradation of the surface groups and bulk material (Section 6.12) and the diversity of the surface groups synthesized for these studies demonstrates the flexibility of this two-step method.

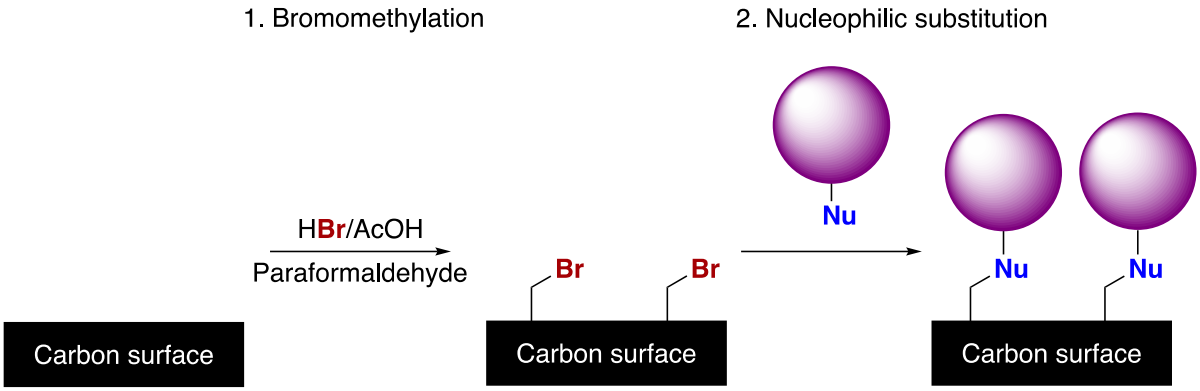

Figure 20. Depiction of the two-step reaction scheme for the surface modification of carbon materials. The purple sphere in the second step represents the choice for the nucleophile, resulting in diverse surface functional groups. For simplicity, surface groups in synthesis figures such as this one are shown attached to an unspecific carbon surface since, in principle, multiple bonding arrangements could be present including bonded to the edge or top of a graphitic sheet. The mechanism and bonding to the surface are discussion in detail in Section 6.7. However, the mixed sp^2/sp^3 hybridization of amorphous carbons[8] such as AC, Vulcan, and CMK3 makes the exact nature of the bonding to the surface ambiguous.

The overall goal of Papers 2, 3, and 4 is to establish the usefulness and applicability of the two-step scheme. In Paper 2, the focus is on the bromomethylation and substitution reactions in order to gain insight into the nature of the surface species, the reaction mechanisms, and the surface group reactivity. In Papers 3 and 4, the focus shifts to the application, in this case Li-S batteries, but unique surface group syntheses still constitute a large portion of these studies. The surface-modified carbons from all three papers are summarized in this section and are discussed and analyzed collectively. The Li-S battery results for four of these carbon materials are discussed in Section 7.

6.3 The reaction conditions for bromomethylation of carbon materials

The first objective was to determine the optimal reaction conditions for first step of bromomethylation and, in turn, achieve the highest possible bromomethyl loading on the carbon surface. Br-based surface groups

are easily quantified relative to the weight of the whole material with XRF (*i.e.* wt% or mmol g^{-1}). The units *mmol* g^{-1} are used throughout this thesis and Papers 2-4 to make direct comparisons between surface group loadings and calculate the corresponding yields. As emphasized previously, the use of heteroatom-based surface groups (*i.e.* anything but H, C, and O) makes this absolute quantification possible. The surface Br groups can be characterized further with XPS (Sections 6.6 and 6.12) but, for these preliminary studies, only bulk Br loadings from XRF were considered in order to efficiently screen as many reaction parameters as possible.

The previous studies from which bromomethylation is derived were used as the starting points for determining its optimal reaction conditions. The first study is about the bromomethylation of small molecules, namely methylated benzenes (Figure 21)[109] and the second is about the *chloro*methylation of activated carbon (AC, Figure 22).[110] The version of bromomethylation described in this thesis and used in Papers 2-4 is simply applying the reaction conditions of the former to make similar surface groups to the latter. The resultant chloro- or bromomethyl groups should be very similar, but the bromomethyl groups should be more reactive to substitution by virtue of bromide being a better leaving group than chloride.[105]

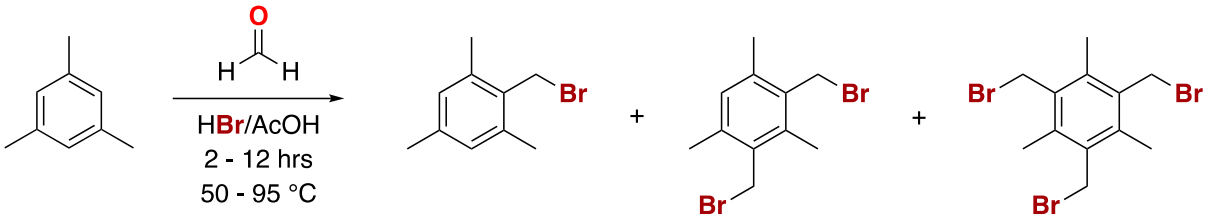

Figure 21. Bromomethylation of mesitylene.[109]

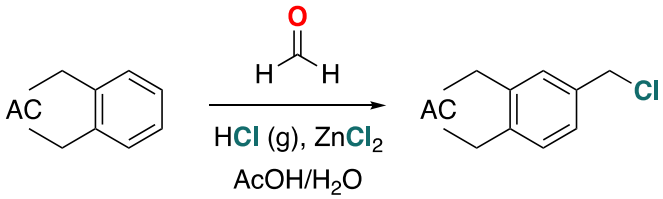

Figure 22. Chloromethylation of activated carbon (AC).[110]

The reaction conditions for bromomethylation of methylated benzenes are centered on using hydrogen bromide (HBr) dissolved in acetic acid (AcOH) as both the reaction medium and source of Br for the -CH_2Br groups. Additionally, for the source of carbon in the -CH_2Br groups, paraformaldehyde, the polymer of formaldehyde, is used. In this procedure, no catalyst was added. In the case of chloromethylation of activated carbon, the reaction conditions also use AcOH as the solvent, but use both gaseous hydrogen chloride (HCl) and concentrated aqueous HCl as the sources of chlorine. This procedure uses aqueous formaldehyde (37 wt%) for the carbon source and zinc chloride ($ZnCl_2$) as the catalyst.

One of the goals of bromomethylation was to simplify the overall procedure, so some aspects of each procedure were taken. The gaseous HCl from chloromethylation was replaced with dissolved HBr in AcOH and solid paraformaldehyde was used in place of an aqueous formaldehyde solution. For the catalyst, the exact role of $ZnCl_2$ was never discussed in detail so two different catalysts were tested (Section 6.4). In the previous bromomethylation procedure, the number of bromomethyl groups on the benzene substrate can be increased by increasing the temperature (95 °C) and duration (12 hrs) of the reaction (Figure 21). Since high surface loadings are almost always desired, the trials for bromomethylation of carbon materials were ran at high temperatures (110 °C) for long times (24 or 48 hrs). The summary of reaction conditions tested during the first study of bromomethylation of AC is shown in Figure 23.

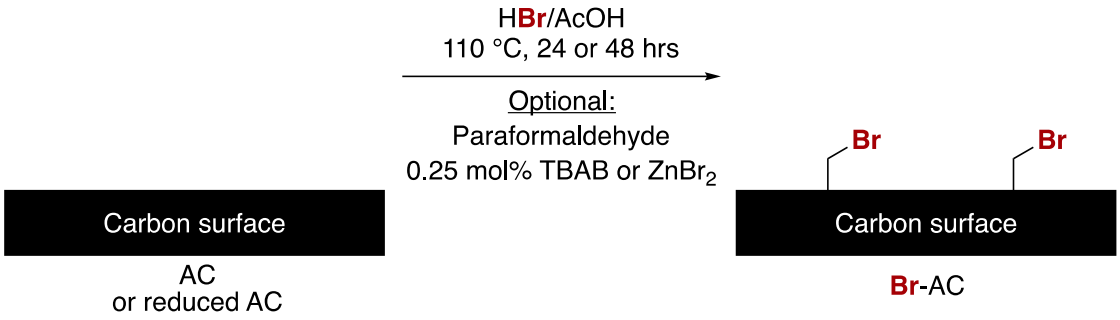

Figure 23. Summary of reaction conditions tested during the first bromomethylation study.

6.4 Factors influencing the bromine loadings in Br-AC

Several aspects of bromomethylation were studied to determine its optimal conditions and achieve the highest possible Br loadings. Additionally, by changing certain parameters of the reaction, one can gain insight into the bromomethylation mechanism (Section 6.7). The initial bromomethylation study used Darco© activated carbon (AC) due to its high surface area (BET surface area = 1000 m^2 g^{-1}) and low cost (approximately 200 USD per kg).

The first factor studied was pre-reduction of the AC substrate followed by treatment in HBr/AcOH with or without paraformaldehyde. The pre-reduction determines how much Br AC can incorporate onto its surface with or without its native oxide layer while the addition of paraformaldehyde reveals how this polymer affects the surface oxide layer and resultant Br loadings. Importantly, this analysis serves as a "baseline" measurement; any changes to the reaction conditions (*e.g.* increased time, addition of catalysts) should increase the Br level well above this level. The reduction conditions were the same as reported for carbon discs[111] (5% H_2 in N_2 at 1000 °C for 90 min) and the results are summarized in Table 10.

Table 10. Trials of bromomethylation on reduced/non-reduced AC substrates with or without paraformaldehyde.

Entry	Reduced	Paraformaldehyde	Br loading (mmol g^{-1})§
1	Yes	No	0.14
2	Yes	Yes	0.34
3	No	No	0.39
4	No	Yes	0.39

§ -Determined by XRF

Reaction conditions: AC (200 mg), 33 wt% HBr in AcOH (2 mL) at 110 °C for 24 hrs. Reactions were run with and without paraformaldehyde (500 mg, 16.6 mg). Reduced AC substrates were treated with 5% H_2 in N_2 at 1000 °C for 90 min.[111]

In the case of reduced AC without paraformaldehyde (Table 10, Entry 1), a very low Br content is measured while non-reduced AC incorporates over 2x the amount of Br after refluxing in HBr/AcOH for 24 hrs (Table 10, Entry 2). This lends evidence to the native oxide layer of AC containing sites for Br incorporation (*e.g.* a benzylic alcohol, see Section 6.7). Adding paraformaldehyde to the reaction mixture allows for the reduced AC to take up a much larger quantity of Br, similar to levels in non-reduced AC (Table 10, Entry 3). Inclusion of paraformaldehyde to non-reduced AC does not change its Br levels appreciably (Table 10, Entry 4). From these measurements, it is determined that paraformaldehyde can, in effect, substitute for the native oxide layer of AC and allow for higher Br levels. However, since pre-reduction of AC represents another synthetic step and only seems to reduce the final Br loading, this step was removed for future studies of bromomethylation.

The second factor studied was adding a catalyst. In the chloromethylation study, $ZnCl_2$ was used;[110] thus, zinc bromide ($ZnBr_2$) was an obvious choice of catalyst. As a catalyst, $ZnBr_2$ could potentially serve two roles: as a Lewis acid (Zn^{2+}) and/or as a source of bromide (Br^-) anions. To test this hypothesis, tetrabutyl-

ammonium bromide (TBAB) was also employed as a catalyst because it serves as a source of soluble bromide anions but lacks the Lewis acid capabilities of $ZnBr_2$. The results are summarized in Table 11.

Table 11. Trials of bromomethylation using either a zinc bromide ($ZnBr_2$) or tetrabutylammonium bromide (TBAB) catalyst.

Entry	Reduced	Paraformaldehyde	Catalyst	Br loading (mmol g^{-1})§
1*	No	No	None	0.39
2*	No	Yes	None	0.39
3	No	No	$ZnBr_2$	0.38
4a	No	Yes	$ZnBr_2$	0.74
4b				0.56
5	No	No	TBAB	0.43
6a	No	Yes	TBAB	1.01
6b				0.97

§ -Determined by XRF

* -For easier comparison, Entries 1 and 2 are reproduced from Table 10, Entries 3 and 4, respectively.

-Reaction conditions: AC (200 mg), 33 wt% HBr in AcOH (2 mL) at 110 °C for 24 hrs. Reactions were run with and without paraformaldehyde (500 mg, 16.6 mg). For reactions containing catalysts, 0.25 mol% of either TBAB or $ZnBr_2$ was used (relative to paraformaldehyde, 0.0417 mmol).

The addition of either catalyst without paraformaldehyde (Table 11, Entries 3 and 5) results in similar Br loadings to non-reduced AC with or without paraformaldehyde (Table 11, Entries 1 and 2). With addition of the polymer, however, the Br loadings are significantly increased (Table 11, Entries 4 and 6). Two trials of each were performed in an effort to establish the superior catalyst for Br incorporation: $ZnBr_2$ allows for an average uptake of 0.65 mmol g^{-1} of surface Br (a 61% increase) while TBAB averages at 0.99 mmol g^{-1} (a 154% increase). The significantly higher loadings achieved with TBAB over $ZnBr_2$ suggest that TBAB is the superior catalyst. Additionally, the observation that the improvements realized for both catalysts occurred only in the presence of paraformaldehyde points to their possible role: to facilitate paraformaldehyde de-polymerization and/or incorporation onto the AC surface. These potential roles are discussed in Section 6.7. For future reactions, only TBAB was used.

The final condition tested was extension of the reaction time from 24 to 48 hrs and the results are shown in Table 12. Curiously, extending the reaction time to 48 hrs but with omission of paraformaldehyde and TBAB (Table 12, Entry 2) results in a drastic decrease in the Br loading by nearly 50% relative to the 24 hr reaction with both of these reagents (Table 12, Entry 1). For the 48 hr trials, inclusion of only TBAB does not increase the Br level significantly (Table 12, Entry 3) while inclusion of only paraformaldehyde returns the Br levels to *ca.* 1 mmol g^{-1} (Table 12, Entry 4). Using both reagents results in a small increase to *ca.* 1.13 mmol g^{-1} (Table 12, Entry 5). These loadings demonstrate that, for 48 hr reactions, paraformaldehyde is more important than TBAB since a large Br loading was still obtained in the absence of TBAB (Table 12, Entry 4), which stands in contrast to the 24 hr reaction, where inclusion of both reagents was needed to achieve high Br loadings (Table 11).

Table 12. Trials of bromomethylation of AC at 24 or 48 hrs.

Entry	TBAB	Paraformaldehyde	Reaction time (h)	Average Br loading (mmol g^{-1})§
1*	Yes	Yes	24	1.01
2	No	No	48	0.58
3	Yes	No	48	0.51
4	No	Yes	48	0.99
5#	Yes	Yes	48	1.13

§ -Determined by XRF

* -For easier comparison, Entry 1 is reproduced from Table 11, Entry 6a.

-Entry 5 is the average of 12 Trials.

-Reaction conditions: AC (200 mg), 33 wt% HBr in AcOH (2 mL, 11.4 mmol HBr), TBAB (0.25 mol%, 13.4 mg), paraformaldehyde (500 mg, 16.6 mg) at 110 °C for 48 hrs. The reactions were ran with and without paraformaldehyde (500 mg, 16.6 mg) and TBAB (0.0417, 13.4 mg). For 48 hr reactions, an additional 2 mL of 33 wt% HBr in AcOH was added after the first 24 hrs.

Overall, the optimal reaction conditions for bromomethylation of AC are: no pre-reduction, inclusion of paraformaldehyde, use of TBAB as the catalyst, and running the reaction for 48 hrs (Figure 24). The reaction under these conditions was ran a total 12 times to obtain a sense of its variability and reproducibility (Table 12, Entry 5; Table A23 in Appendix). Br loadings between 0.84 and 1.37 were realized, showing that the reaction is prone to some variability, but the average Br loading of 1.12 mmol g^{-1} is comparable to the chlorine loadings for chloromethylation (*ca.* 1.5 mmol g^{-1}).[110] These optimized bromomethylation conditions were applied to other materials as shown in the next section.

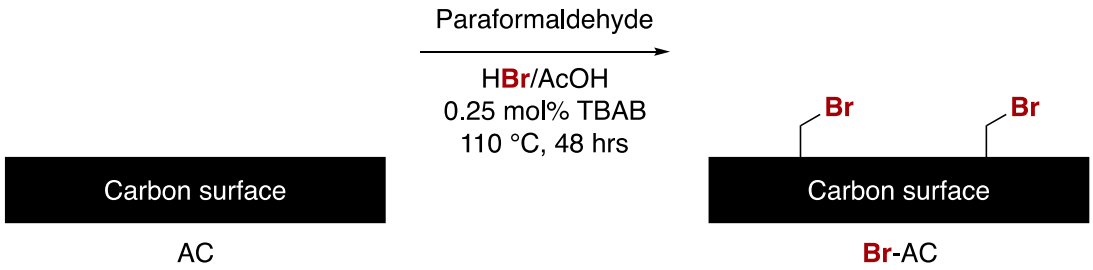

Figure 24. Summary of the optimal reaction conditions for the bromomethylation of AC.

6.5 Bromomethylation of other carbon materials

So far, only AC has been considered as the substrate for bromomethylation. The reaction was applied to other, differently structured carbon materials to see how the obtained Br loadings are affected. Two other amorphous carbon materials were selected: CMK3, a high surface area, hexagonal ordered mesoporous carbon (OMC) derived from ordered mesoporous silica SBA-15;[112] and XC-72R (Vulcan) a lower surface area, but highly conductive carbon black consisting of 50 nm nanoparticles.[113] The carbons are commercially available from ACS Materials© and The Fuel Cell Store©, respectively. When ran on the same scale as AC (200 mg), both of these materials bromomethylate efficiently and Br loadings of 1.04 and 0.30 mmol g^{-1} are achieved for CMK3 and Vulcan, respectively (Table 13, Entries 2 and 3). When studied by nitrogen-sorption (Section 3.2.1), a small decrease in the BET surface area is measured for the bromomethylated carbons relative to starting material (Figure 25, left and Table 13). The Br loadings of these carbons correlate well with their initial BET surface areas and the regression line is shown in Figure 25, right. Based on the slope of this line, the bromomethyl groups each occupy about 1.5 nm^2 on average, or about 7 x 10^{13} molecules cm^{-2}. This coverage compared to a flat surface is rather low; a closest-packed monolayer of surface-bound ferrocenes is about 4x denser at 3 x 10^{14} molecules cm^{-2}.[114-115] Additionally, since ferrocene is expected to be larger than a bromomethylgroup, the low coverage of bromomethyl groups is especially telling. Possible explanations could be that diffusion of all necessary reactants into the small micropores is hindered and/or that bromomethylation only occurs at specific places on the carbon surface (*e.g.* the edge of a graphitic sheet, see Section 6.7).

Table 13. Bromomethylation of AC, Vulcan, and CMK3 and the impact on the BET surface area.

Entry	Substrate	Scale	Br loading[§]	Initial BET surface area ($m^2 g^{-1}$)	Final BET surface area ($m^2 g^{-1}$)	Decrease in surface area (%)
1[#]	AC	200 mg	1.13	1000	840	16
2	Vulcan	200 mg	0.30	240	220	8
3	CMK3	200 mg	1.04	885	750	15
4	CMK3	3 g	0.60	885	815	8
5	CMK3	10 g	0.65	832	732	12

§ -Determined by XRF

-Entry 1 is the average of 12 Trials and is reproduced from Table 12, Entry 5 for comparison.

-Reaction conditions: AC, Vucan, or CMK3 (200 mg), 33 wt% HBr in AcOH (2 mL, 11.4 mmol HBr), TBAB (13.4 mg, 0.0417 mmol), paraformaldehyde (500 mg, 16.6 mmol) at 110 °C for 48 hrs. After 24 hrs, an additional 2 mL of 33 wt% HBr in AcOH was added. For the Entries 4 and 5 with larger batches of carbon, all reaction components were scaled proportionally.

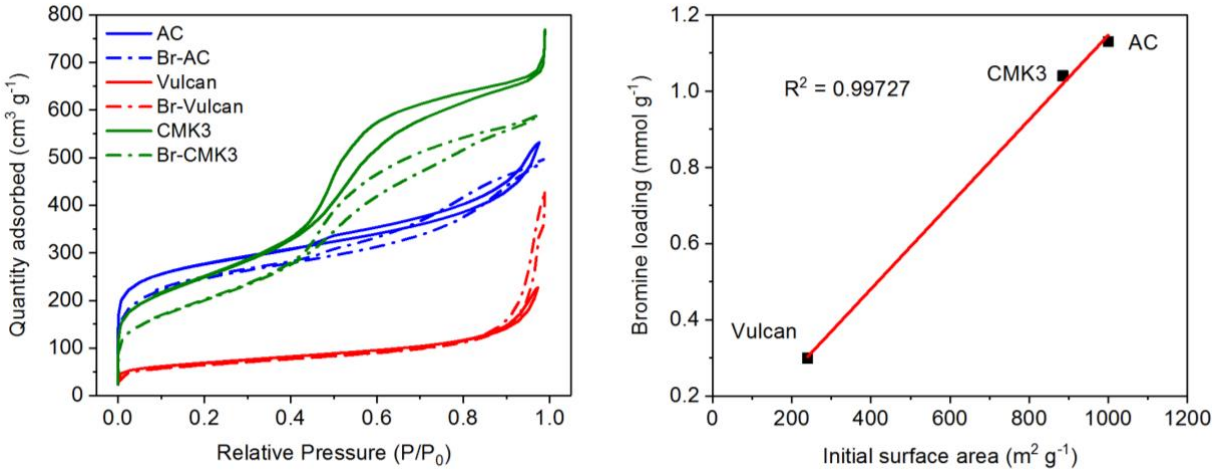

Figure 25. Nitrogen isotherms for AC, Vulcan, and CMK3 and their bromomethylated derivatives (left) and the resulting correlation between their Br loadings and surface areas (right). All reactions were ran with 200 mg of carbon (Table 13, Entries 1-3).

Two more batches of bromomethylated CMK3, Br-CMK3, were synthesized, both on larger scales of 3 and 10 grams (Table 13, Entries 4 and 5). The first batch is for Paper 2 and the second batch for Papers 3 and 4 (Table 16). For both trials, about 60% of the previous Br loading was obtained, which could indicate that the bromomethylation reaction becomes less efficient as it is scaled up. However, the loadings for each batch are still reasonable meaning that the reaction is amenable to larger scale preparations. For all materials and scales, a reasonable decrease in the BET surface area is observed. Further analysis on nitrogen-sorption analysis of functionalized carbons is given in Section 6.12.

6.6 Characterization of the surface bromine species

Up to this point, only the quantity of Br incorporated into AC was considered. Indeed, X-ray fluorescence (XRF, Section 3.1.2) can only determine the amount of Br and cannot differentiate among different oxidation states and/or bonding arrangements of various Br species. To further characterize the surface Br species, X-ray photoelectron spectroscopy (XPS, Section 3.1.3) was employed. The binding energy reveals the oxidation state of the Br species; previous work has shown that bromide anions have binding energies around 68 eV,[116-117] while aryl bromides have binding energies around 70-71 eV.[118] The difference in binding energy comes as the result of the Br atom being bonded to, and thus sharing electron density with, a carbon atom, which effectively oxidizes the Br atom relative to an unbonded, monoanionic bromide ion (Figure 26).

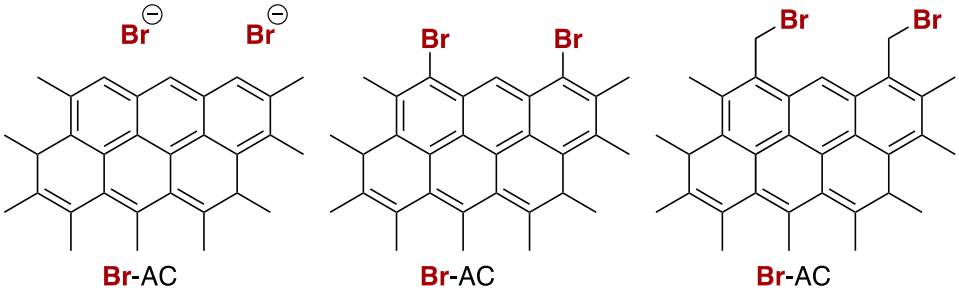

Figure 26. Possible surface Br species on Br-AC: non-covalently bonded anionic bromide (left), aryl bromides (center), and alkyl bromides (right). The species are shown bonded to the edge of a graphitic sheet, which is discussed in Section 6.7. The XPS spectra and reactivity of the surface Br species in Br-AC and other bromomethylated carbons (Br-CMK3) are consistent with an alkyl bromide.

In the Br 3d spectra for Br-AC and two trials of Br-CMK3 (Figure 27), one main peak around 70.5 eV is observed, which likely means that the Br species is bonded to a surface carbon atom in all three cases. While an aryl bromide is a possibility, which could conceivably come from direct bromination of the carbon surface (Figure 26, center), its reactivity under substitution conditions is most consistent with an alkyl bromide (*i.e.* a bromomethyl group, see Sections 6.8-6.10). A small to negligible difference in binding energy is expected between aryl and alkyl bromides given that, in both cases, the Br atom is bonded to a carbon atom in similar oxidation states. In the case of two trials for Br-CMK3, their lower Br loadings are reflected in their weaker signals of the main peak and a relatively large shoulder peak is also observed at around 68 eV. The peak at 68 eV could indicate the presence of a reasonable quantities of bromide anions trapped in the pores of both Br-CMK3 samples. In principle, Br-AC could also have some bromide anions, but the lack of a noticeable shoulder peak makes this unlikely. The different pore structures and synthesis methods for AC and CMK3 could potentially explain this difference.

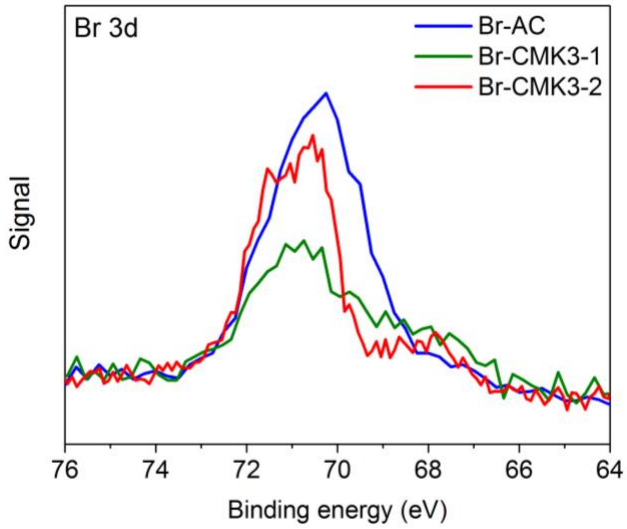

Figure 27. Br 3d X-ray photoelectron spectra of Br-AC and Br-CMK3. The labels for Br-CMK3-1 and Br-CMK3-2 correspond to Table 13, Entries 4 and 5, respectively. The same labels are used later in their characterization (Section 6.12 and Table 16).

6.7 Mechanism of bromomethylation

Understanding the mechanism behind bromomethylation is critically important. By knowing how the surface groups are formed, one can gain insight into characteristics of the reaction including: its potential to form multilayers; how to maximize surface group loadings while maintaining the carbon's integrity; how to transform one functional group into another; what its potential limitations could be; and the nature of the bonding to the amorphous carbon surface. The reaction mechanism for chloromethylation offers a

starting point.[110] The reaction is proposed to happen in two steps: one to form a benzylic alcohol intermediate and two to replace the benzylic alcohol with benzylic chloride. For the first step, formaldehyde is proposed to react with the edge of a graphitic sheet *via* electrophilic aromatic substitution, which forms the benzylic alcohol intermediate (HO-AC, Figure 28). Although not discussed explicitly, protonated formaldehyde as the reactive species is a possibility given the highly acidic conditions.

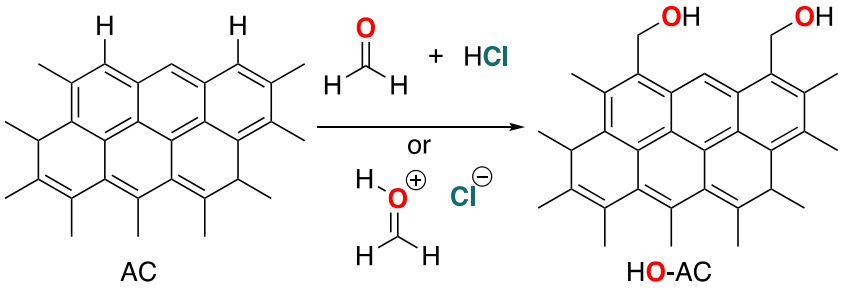

Figure 28. First step of the proposed mechanism for the chloromethylation of AC.[110] Electrophilic aromatic substitution (EAS) occurs at the edge of a graphitic sheet with a formaldehyde (top) or protonated formaldehyde (bottom) as the electrophile. The aromatic proton is replaced with a benzyl alcohol group forming the intermediate surface of HO-AC.

In the second step, the benzylic alcohol groups on HO-AC become protonated due to the strongly acidic conditions, which transforms the hydroxyl group (OH) into a good leaving group (OH_2^+). Subsequently, chloride anions can displace H_2O *via* a nucleophilic substitution reaction (S_N2) on the protonated alcohol, thereby forming the desired chloromethyl groups (Figure 29).

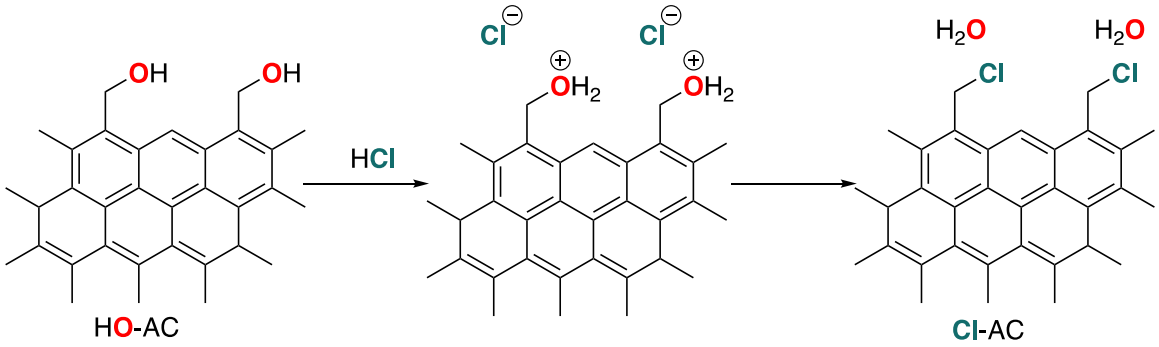

Figure 29. Second step of the proposed mechanism for the chloromethylation of AC.[110] Protonation of the benzyl alcohol groups of the intermediate surface HO-AC makes them into good leaving groups and subsequent nucleophilic substitution by chloride displaces water and forms the chloromethyl groups on Cl-AC.

Overall, given the similarity between the reaction conditions for chloro- and bromomethylation of AC, there is no reason to suspect that the reaction mechanism for bromomethylation deviates in any meaningful way. As evidence for the proposed mechanism, a large mass increase between 23 and 66% (average 45%) was recorded for all twelve trials of bromomethylation (Table A23 in Appendix). This mass uptake is consistent with the proposed reaction mechanism of first forming a benzyl alcohol functional group with subsequent bromide substitution on the protonated alcohol; both reactions should increase the mass of the carbon substrate. The average mass increase for bromomethylation is also consistent with the mass increase reported for chloromethylation (*ca.* 17%).[110] In other words, given the similar surface group loadings obtained from chloro- and bromomethylation (*ca.* 1.1 – 1.5 mmol g^{-1}) and the heavier mass of Br relative to chlorine (2.2x), a larger mass increase of about 38% is expected for bromomethylation. The individual mass increases for bromomethylation of AC roughly correlate with their respective Br loadings (Figure 30).

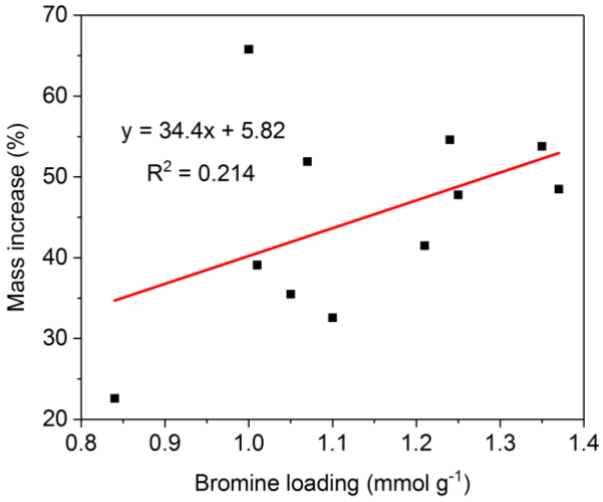

Figure 30. Correlation between the mass increase and the Br loadings for 12 trials of bromomethylation of AC to form Br-AC (Table 13, Entry 1).

Assuming similar reaction mechanisms, one can infer the roles of each reaction component: HBr, AcOH, paraformaldehyde, and TBAB. For HBr, this strong mineral acid (pKa = -9)[105, 119] can protonate both formaldehyde and the benzylic alcohol intermediate. It also provides the bromide anions for the substitution step. For AcOH, this weaker organic acid (pKa = 4.76) could also conceivably provide protons, but its main role is the solvent. Importantly, as a solvent, AcOH is a considerably weaker *base* than H_2O; the pKas of protonated AcOH and H_3O^+ are *ca.* -8 and -1.7, respectively.[119] This means that, due to solvent leveling,[120] the effective pKa of the protons in HBr will be lowered to -8 and -1.7 in AcOH and H_2O, respectively; the higher effective acidity of HBr in AcOH should facilitate greatly the necessary protonation reactions. Additionally, by excluding excess H_2O from the system, the last step of removing H_2O from the carbon surface becomes easier *via* Le Chatelier's Principle. Since many unoxidized carbons are somewhat hydrophobic,[8] the choice of a polar organic solvent such as AcOH should also help to disperse the carbon material in the reaction mixture allowing for more efficient functionalization.

For paraformaldehyde, its role is to provide formaldehyde monomers to form the benzylic alcohol intermediate (Figure 28). For this to occur, it must first de-polymerize. The higher Br loadings recorded when a catalyst ($ZnBr_2$ or TBAB) was used in conjunction with paraformaldehyde for 24 hr reaction times suggest a synergistic effect between the polymer and either catalyst (Table 11 and Table 12). Part of this effect could be facilitating the de-polymerization of paraformaldehyde. For 48 hr reactions, the synergistic effect appears to be less important since high Br loadings were still recorded when only paraformaldehyde was used (Table 12, Entry 4). Importantly, since reasonably high Br loadings were recorded in the absence of both paraformaldehyde and a catalyst (Table 10, Entry 3 and Table 12, Entry 2), some benzylic alcohol groups are likely present on the AC surface as part of its native oxide layer.

For TBAB, its role is as a catalyst. Since very little N was found on the Br-AC or Br-CMK3 surface for any trial, the TBA^+ cation is likely a "spectator ion" during the entire reaction (TBA^+ and N_2 were the only sources of N during bromomethylation). Thus, any catalytic activity is likely due to the bromide anion: one plausible role of TBAB is providing bromide anions to facilitate the second step of bromide substitution on the protonated benzylic alcohol. By virtue of containing a weakly coordinating cation, the bromide anions in TBAB are likely more nucleophilic compared to the more coordinated HBr species in the reaction mixture. This reasoning is supported by the lower Br loadings recorded when $ZnBr_2$ was used as the catalyst instead of TBAB (Table 11). Specifically, even though $ZnBr_2$ provides twice the number of bromide anions compared to TBAB, the much higher Lewis acidity of Zn^{2+} compared to TBA^+ could cause it to coordinate to bromide anions. The coordination of bromide anions to Zn^{2+} would conceivably lower their nucleophilicity and, therefore, their catalytic activity in the second substitution reaction (Figure 29).

By understanding the previously described two-step mechanism to form the surface bromomethyl groups, one can start to answer some of the questions asked at the beginning of this section. Most importantly, as to its potential to form multilayers, the bromomethylation reaction mechanism would seem to restrict all functionalization to a monolayer. That is, the reactive formaldehyde species cannot add a second time to a previously formed benzylic alcohol or bromide; such a reaction could not occur *via* Electrophilic Aromatic Substitution since the formaldehyde species would need to react with an aliphatic -CH_2OH or -CH_2Br group. The reaction mechanism for nucleophilic substitution of bromide in the second synthetic step also restricts all functionalization to a monolayer (Sections 6.8-6.10). Monolayer functionalization in both steps is supported by nitrogen-sorption and SAXS analysis of surface modified CMK3 (Section 6.12).

As to how to maximize surface Br loadings, employing both paraformaldehyde and TBAB is key. Extending the reaction time to 48 hrs (Table 12) also increases the Br loadings. Importantly for extended reaction times, since the two steps for bromomethylation involve only substitution reactions with non-oxidizing acids (HBr and AcOH), it is unlikely that prolonged bromomethylation could remove a significant amount of material (*e.g.* as CO_2, CO, CH_4) from the surface. This prevents etching or pitting from occurring into the bulk of the material, thereby maintaining the carbon's structural integrity during long reaction times. Analysis using SEM, SAXS, and XRD confirms retention of the CMK3 morphology, meso- and atomic structure after bromomethylation and substitution (Section 6.12).

As to how to transform the bromomethyl groups into other functional groups, benzylic bromides are excellent substrates for nucleophilic substitution reactions, which is the subject of Sections 6.8-6.10.

As to the potential limitations of this reaction, the multi-step nature of the bromomethylation mechanism implies that, under certain conditions, the reaction could be rather slow. Diffusion of all necessary reactants into the micro- and meso-pores of a high-surface area carbon material could be hindered, resulting in sluggish functionalization and low surface group loadings. By comparison, functionalization *via* diazonium salts requires only one facile step involving the favorable release of N_2 gas, and, because of this, such surface reactions are notable for their fast reaction times and high loadings.[41-43] The 4x lower surface coverages of bromomethyl groups compared to ferrocenes on a flat surface (Section 6.5) are consistent with a slower mechanism. The lower Br loadings obtained for large batches of Br-CMK3 also indicate a slower reaction mechanism as the reaction scale is increased (Table 13, Entries 4 and 5).

Finally, as to the exact nature of the bonding to the surface, it is still not yet fully understood. At the beginning of this section, the surface groups were proposed to bond to the edge of a graphitic sheet (Figure 28). However, as amorphous carbons, AC, CMK3, and Vulcan have mixed sp^2/sp^3 hybridization[8] and, as such, knowing exactly how the surface groups are bonded the amorphous carbon surface becomes difficult to state. Even with a strictly graphitic carbon, alternate bonding motifs are plausible: the surface groups could be bonded to the face of the graphitic sheet (Figure 31). For the Density Functional Theory (DFT) calculations for Paper 3, this is the bonding used for all surface groups (Figure 61). For face-bonding, the carbon atom bonded directly to the surface group undergoes a hybridization change from sp^2 to sp^3. If the reactive formaldehyde species is a strong enough electrophile, it could possibly add to the graphitic sheet in this manner, even though the aromaticity of the sheet is damaged or destroyed in the process. In the case of edge-bonding, a H^+ is lost from the surface to maintain charge balance. Since H^+ loss is not possible with face-bonding, it is unknown what effects this charge would have on the carbon structure. In the case of the DFT calculations, a proton was added to one of the neighboring carbons and the calculation was ran on a neutral, singlet species.

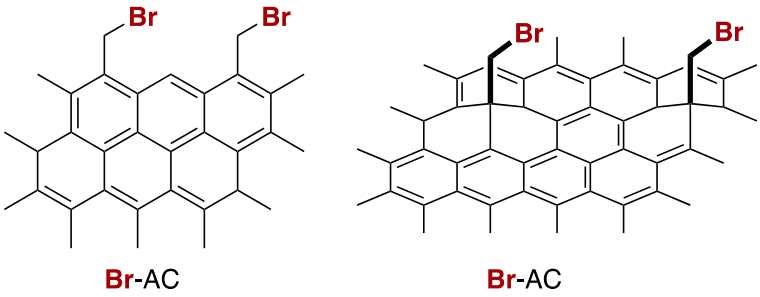

Figure 31. Depiction of the bromomethyl groups of Br-AC bonded to the edge (left) or face (right) of a graphitic sheet. In the case of face bonding, the bromomethyl groups are shown in bold bonds for clarity.

To further complicate potential bonding arrangements to the surface, most carbon materials exhibit high electrical conductivity and a native oxide layer. Such properties could affect potential mechanisms of bromomethylation that would not apply to solution-phase, organic analogues such as fused benzenes (*e.g.* anthracene and pyrene), which lack both characteristics. In summary, the nature of the bonding to the surface of AC, CMK3, and Vulcan is ambiguous; hence, from this point forward, in all figures depicting surface groups in this thesis, the functional groups will be shown bonded to an unspecific carbon surface (Figure 32).

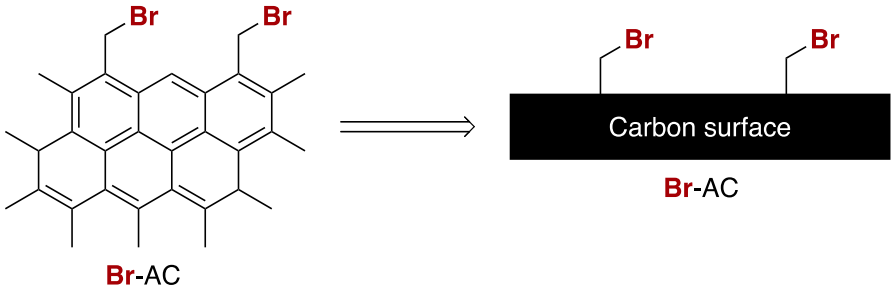

Figure 32. Depiction of the surface groups of Br-AC bonded to edge of a graphitic sheet (left) versus to a non-specific carbon surface (right). Due to the ambiguous nature of the bonding to the surface and for simplicity, all synthesis figures use the non-specific carbon surface.

For future studies on bromomethylation, using carbon materials with a better defined atomic/crystal structure could yield valuable information on the reaction mechanism. To determine which bonding motif (edge or face) dominates in graphitic carbons, one could subject graphite nanoparticles to bromomethylation. If higher Br concentrations are determined on the face or edge, this could give strong evidence for the possible mechanisms of bromomethylation. Likewise, running bromomethylation on a diamond surface could reveal if sp^3 hybridized carbon could contribute to possible bonding arrangements to the surface.

6.8 Substitution of bromide with azide nucleophiles

While the bromomethyl groups themselves could conceivably provide a useful surface for some applications, their true strength lies in their ability to be easily and quantitatively transformed into other functional groups. As is taught in solution-phase organic chemistry,[105] primary alkyl bromides such as benzyl bromides are susceptible to nucleophilic substitution reactions (*i.e.* S_N2) given the good leaving group ability of bromide (leaving group ability is inversely proportional to basicity; weaker bases are better leaving groups). The nucleophile in such reactions can be any species with a weakly bonded pair of electrons but is normally a non-bonding pair. Example nucleophiles include amines, hydroxide, halides, azide, alkoxides, and thiolates. The diversity of nucleophiles used in the solution phase demonstrates that the surface bromomethyl groups could potentially be transformed into a wide range of functional groups (Figure 33). Indeed, this was found to be the case as shown below.

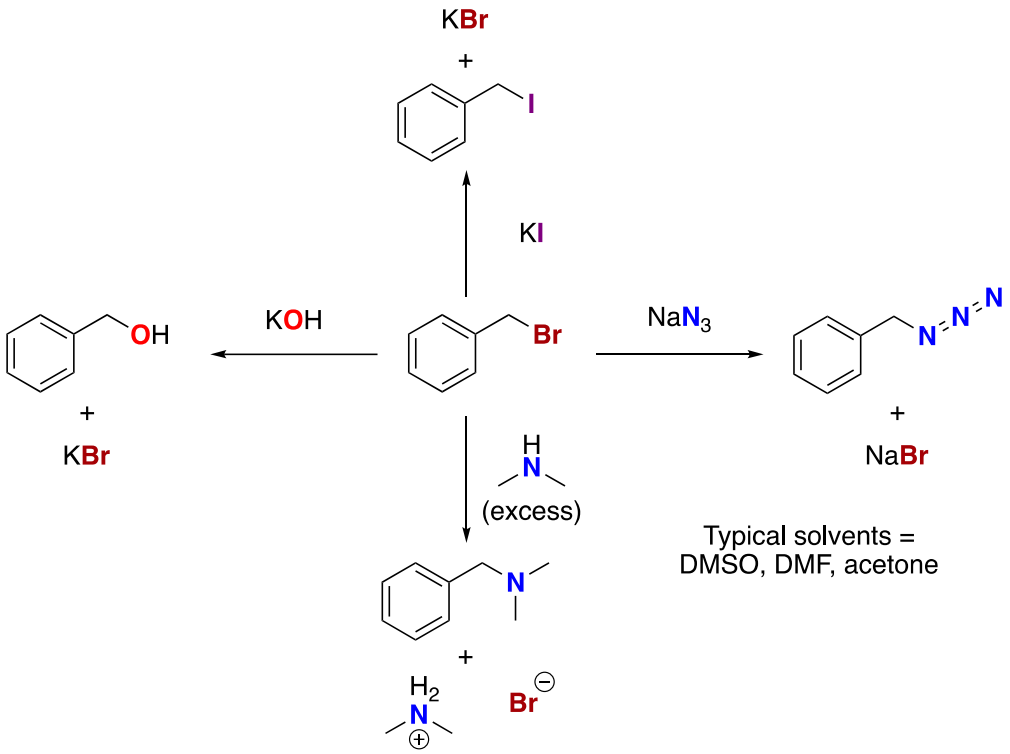

Figure 33. Illustration of the synthetic utility of primary alkyl bromides like benzyl bromide. The bromomethyl group of benzyl bromide can be easily and efficiently transformed into other functional groups via nucleophilic substitution reactions. The surface bromomethyl groups of Br-AC and Br-CMK3 are proposed to react similarly to benzyl bromide.

The first nucleophile studied was azide (N_3^-) since organic azides (R-N_3), including those bound to surfaces, can be coupled to a plethora of terminal alkynes by way of the Cu(I)-catalyzed azide-alkyne cycloaddition reaction (CuAAC reaction, Figure 45).[111, 115, 121-123] The solvent used for nucleophilic substitutions is normally a polar aprotic liquid such as dimethylsulfoxide (DMSO), N,N-dimethylformamide (DMF), or acetone. This class of solvents can dissolve the salt, in this case sodium azide (NaN_3), but without hydrogen bonding to the anion. Hydrogen bonding to anions is known to decrease considerably the rate of S_N2 reactions.[105] Thus, the reaction conditions chosen were NaN_3 dissolved in a dispersion of Br-AC in DMSO at 110 °C for 24 hrs (Figure 34). The concentration of NaN_3 was 0.5 M with an approximate azide-to-bromomethyl molar ratio of 80 assuming 1 mmol g^{-1} of Br on Br-AC. The large excess of azide should help the substitution reaction reach completion.

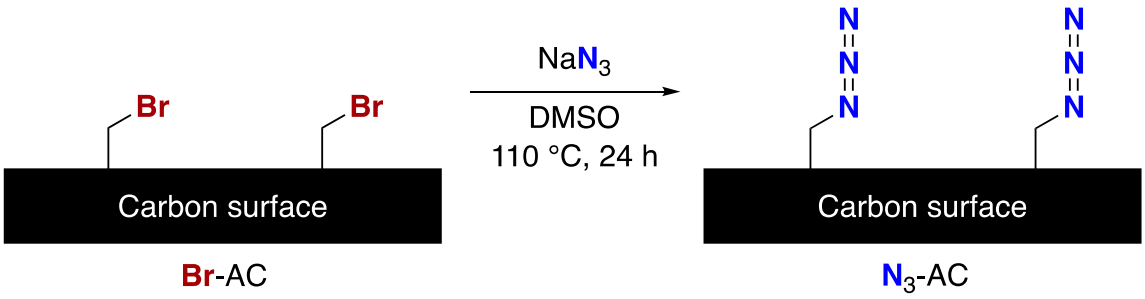

Figure 34. Synthesis of N_3-AC from Br-AC using nucleophilic substitution.

A total of seven trials of azide substitution on Br-AC were run and the azide loadings on the resultant N_3-AC materials were determined by N elemental analysis (EA, Section 3.1.1; Table A24 in Appendix). Based on the starting Br content determined from XRF, an average yield of 85% was obtained, which suggests an efficient reaction mechanism for the conversion of bromomethyl to azidomethyl surface groups (Figure 34). Coincidently, the residual Br content as determined by XRF is very low, around 5 - 8% of its original value, which also supports an efficient substitution mechanism. XPS analysis corroborates azide substitution of Br

on N_3-AC: the N 1s spectrum of N_3-AC exhibits the diagnostic features of azide (401 and 405 eV)[111, 121-122] and shows a greatly reduced intensity of the Br 3d peak at 70.5 eV (Figure 35). Similar to the bromomethylated surfaces, the stability of the azide-terminated surface of N_3-AC is remarkable with a less than 5% loss of N after storage for 100 days in air. This stands in contrast to other methods for the synthesis of surface-bound azide groups, which found significant azide decomposition after several days of storage.[111]

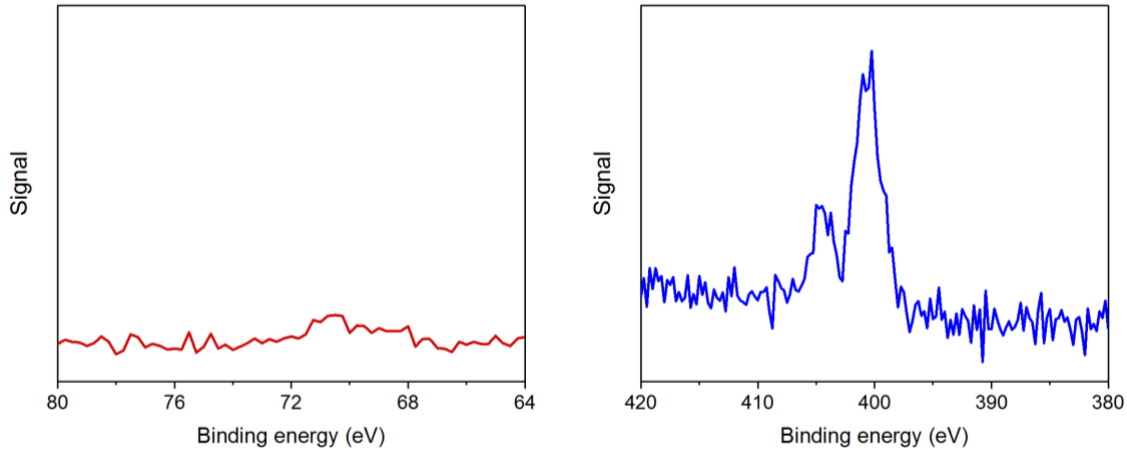

Figure 35. X-ray photoelectron spectra of N_3-AC: Br 3d region (left) and N 1s region (right).

6.9 Substitution of bromide with iodide and amine nucleophiles

To increase the scope of the substitution reaction and therefore the range of potential surface groups, other nucleophiles were employed to replace azide (Figure 36 and Table 14). Iodide is a strong nucleophile and so sodium iodide (NaI) was used in place of NaN_3 under identical reaction conditions to synthesize I-AC. In this case, a lower yield of 58% for one trial of I-AC (Table 14, Entry 1) was recorded compared to an average of 85% for N_3-AC. The residual Br loading in this case was 15%, which leaves about 25% of the Br content unaccounted for. The lower yield suggests that, under these conditions, azide is better nucleophile than iodide. The disappearance of 25% of the Br content could be due to the excellent leaving group ability of iodide; water and/or alcohol displacement of iodide during the washing and drying steps is a plausible explanation.

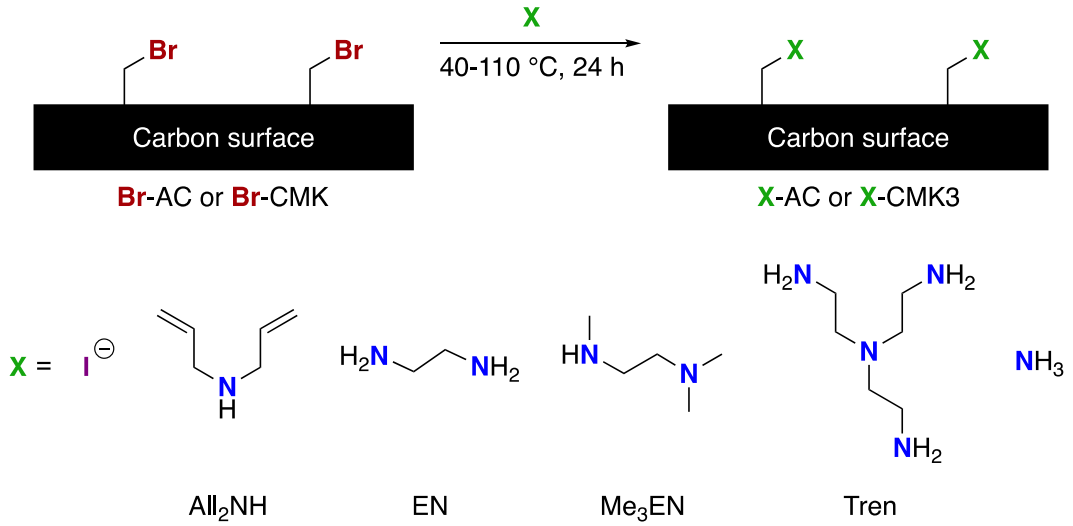

Figure 36. Nucleophilic displacement of bromide on Br-AC or Br-CMK3 with various nucleophiles.

Table 14. Substitution of Br on Br-AC and Br-CMK3 using iodide and amine nucleophiles.

Entry	Substrate	Initial Br loading (mmol g^{-1})	Nucleophile (X)	X loading (mmol g^{-1})	Yield (%)
1	Br-AC	1.01	Sodium iodide	0.59[§] (0.15)[#]	58 (15)
2	Br-AC	1.12	Diallylamine (All_2NH)	1.02*	91
3a	Br-AC	1.05	Ethylenediamine (EN)	1.29*	123
3b		1.37		1.72*	126
4	Br-AC	1.12	N,N,N'-trimethylethylenediamine (Me_3EN)	0.81*	72
5a	Br-CMK3	0.60	Ethylenediamine (EN)	0.80* (<0.1)[#]	133 (<17)
5b		0.65		0.91* (0.14)[#]	140 (22)
6a	Br-AC	1.10	Tris(2-aminoethyl)amine (Tren)	0.99*	90
6b		1.05		0.65*	62
7	Br-AC	1.00	Ammonium hydroxide (NH_4OH)	2.00* (1.15)[▽]	200 (115)

§ -Determined by iodine XRF
# -Residual bromine loading determined by XRF
* -Determined by nitrogen EA
▽-Determined by EA two months after preparation

The nucleophile to displace bromide need not be an anion: neutral, free base amines are also competent nucleophiles. Since many amines are liquids at room and elevated temperatures (20 - 110 °C), the amine can also serve as its own solvent. In other words, the bromomethylated carbons were simply dispersed in neat amine and were heated at elevated temperatures to induce bromide displacement and C-N bond formation. Several liquid amines were employed to reveal how such a treatment affects the surface of the carbon. The first was diallylamine amine (All_2NH), a secondary amine, to form All_2N-AC which resulted in a high yield (91%; Table 14, Entry 2). Similar treatment of Br-AC with ethylenediamine (EN) to form EN-AC resulted in higher-than-expected yields of 123% and 126% over two trials (Table 14, Entries 3a and 3b). Interestingly, EN's trimethylated counterpart, N,N,N'-trimethylethylenediamine (Me_3EN), exhibits a yield of close to 70% under the same reaction conditions with Br-AC (Table 14, Entry 4) while two trials of EN substitution on Br-CMK3 resulted in yields of 140% and 125% (Table 14, Entries 5a and 5b). The >100% yield with EN appears to be reproducible on different bromomethylated carbon substrates.

The high yield with EN suggests the possibility of side reactions occurring between it and Br-AC that apparently do not occur for Me_3EN. The different reactivities of primary amines (EN) compared to secondary and tertiary amines (All_2NH, Me_3EN) could account for this difference. Possible side reactions are likely to occur with one or more of the O-based functional groups present naturally in the oxide layer of Br-AC since pure amines do not normally show strong reactivity with aromatic or aliphatic hydrocarbons.[105] It is also important to point out that the previous bromomethylation reaction could have a strong effect on this oxide layer before EN substitution; indeed, a significant change in the O 1s XPS spectrum was found for the first batch of modified CMK3 and is discussed in Section 6.12.

Possible side reactions with primary amines include a condensation with an aldehyde or ketone to form an imine and nucleophilic acyl substitution with an ester or carboxylic acid to from an amide (Figure 37). Secondary and tertiary amines are not expected to undergo these reactions or to only a very limited extent,[105] which would account for the disparity in yields. Other, non-covalent interactions between EN and the oxide layer are possible such as hydrogen bonding to an alcohol and acid-base reactions with a carboxylic acid. However, the observation that EN-AC does not lose a significant amount of N after sonication in water for several hours suggests that the vast majority of surface groups are covalently

attached. In both EN-AC and EN-CMK3, the N content does not decrease significantly after being stored in ambient conditions, which further supports covalent bonding to the surface.

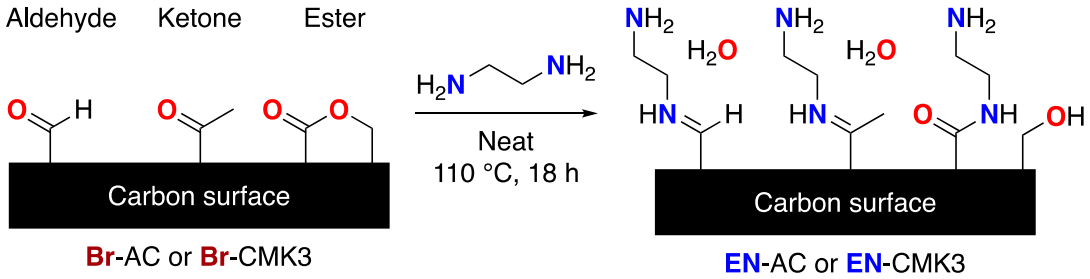

Figure 37. Possible side reactions between EN and the native oxide layer of Br-AC or Br-CMK3 to account for the >100% yields of EN-AC and EN-CMK3. Compatible O-based functional groups include aldehydes and ketones, which would result in an imine and water byproducts, and esters, which would result in an amide and an alcohol byproduct. Given the reducing conditions of neat EN, the imine groups could conceivably be reduced to the corresponding amine.

The nucleophile set was increased to include tris(2-aminoethyl)amine (Tren), a tetraamine with 3 primary amines. When two batches Br-AC were boiled in neat Tren, yields of 90% and 62% were obtained (Table 14, Entries 6a and 6b). While both EN and Tren contain multiple primary amines and, in principle, can undergo the same side reactions, the decidedly lower yields recorded for Tren suggest that one Tren nucleophile can displace multiple bromides. This would lower the N content of Tren-AC relative to single point attachments. The much larger size and higher flexibility of tren make these bridging structures more likely (Tren*-AC, Figure 38). Similar structures are possible with EN and its two primary amines, but this would require a clustered arrangement of bromomethyl groups so that at least two are in close enough proximity to each other to form a bridging EN group.

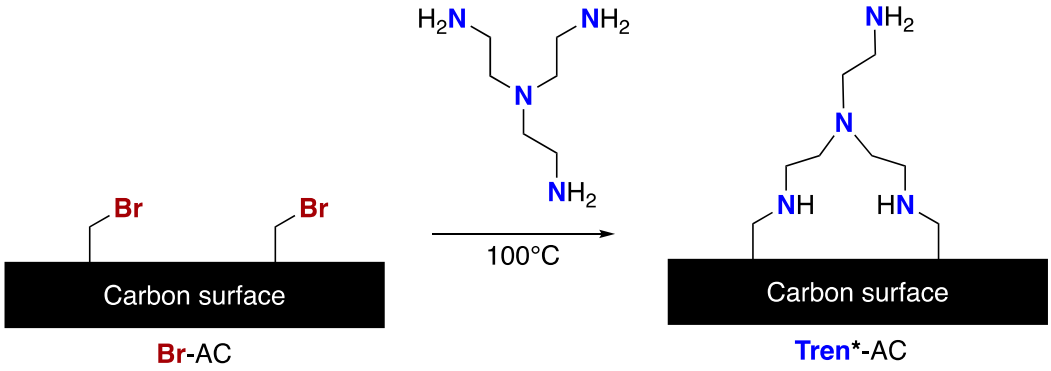

Figure 38. Formation of Tren bridging structures on Br-AC via displacement of two bromides by a single Tren molecule.

Last of all, concentrated ammonium hydroxide (NH_4OH) in water was used in place of a neat liquid amine for substitution of bromide. In many ways, inorganic ammonia (NH_3) bears similar reactivity to organic primary amines; the side reactions mentioned previously (Figure 37) are also possible with ammonia, except the organic carbon chain on N is replaced with a hydrogen. Thus, as expected, when Br-AC was treated in concentrated NH_4OH at 40 °C to form NH_2-AC, a 200% yield was obtained (Table 14, Entries 7). However, unlike EN-AC and EN-CMK3, NH_2-AC undergoes a large decrease in N content two months after preparation to a yield of 115%. This drastic change could be the result of a few factors including the presence of unstable N-based functional groups and/or slow release of trapped NH_3 from the carbon's pores. Even with the large decrease in N, the yield of NH_2-AC is still measurably above 100%, which indicates that some NH_3, like EN, reacts with other surface functionality besides the bromomethyl groups.

6.10 Expanding the nucleophile set: amide and sulfite nucleophiles

For two of the Li-S battery studies, the nucleophile set was expanded to include amides and sulfite. The reasons behind wanting these groups on the carbon surface is detailed in their appropriate sections (Sections 7.3 and 7.4). In the case of sulfite, using it as a nucleophile is very similar to both NaN_3 and NaI: sodium sulfite (Na_2SO_3) was dissolved in a suspension of Br-CMK3 in DMSO and was heated to 110 °C for 24 hrs to form $NaSO_3$-CMK3 (Figure 39). The main difference for this nucleophile is that a NaI catalyst is used to increase the rate of sulfite displacement of bromide: iodide can first substitute for bromide as done with NaI on Br-AC (Table 14, Entry 1) to form iodomethyl groups, which, in turn, contain better leaving groups for sulfite substitution.[105, 119] In a second synthetic step, the alkali metal cation is exchanged for Li to form $LiSO_3$-CMK3 in order to match the Li salts in the battery electrolyte. This is performed by stirring a suspension of $NaSO_3$-CMK3 in a 1 M lithium bis(fluorosulfonyl)imide (LiFSI) aqueous solution for 24 hrs at room temperature; the sheer excess of lithium relative to sodium (*ca.* 40 Li to Na molar ratio) should statistically drive this reaction to completion.

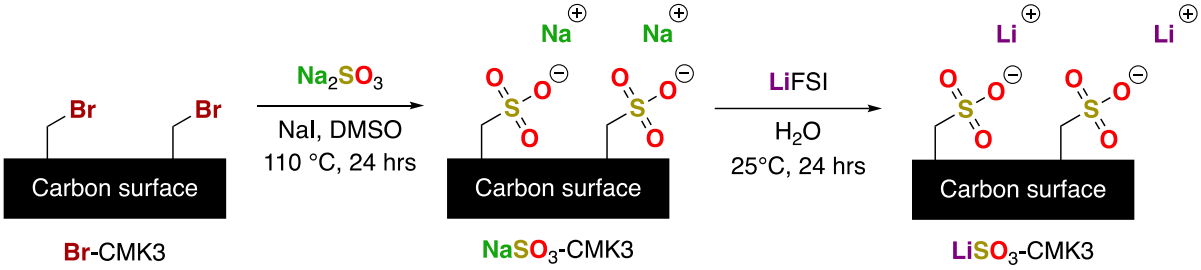

Figure 39. Synthesis of LiSO3-CMK3. Sulfite substitution of bromide occurs with Na_2SO_3 and a NaI catalyst to form NaSO3-CMK3. The alkali metal cations are exchanged by stirring in a LiFSI solution.

For the synthesis of amide surface groups, a much different procedure is required. Distinct from all the nucleophiles used so far, the nucleophilic form of an amide must be generated *in-situ* given the unreactive nature of neutral amides.[105] This is performed by taking advantage of the relatively acidic α C-H protons (*i.e.* adjacent to the carbonyl) of a tertiary amide like N,N-dimethylacetamide (DMA); these protons usually have pKas around 30 compared to 45 for an unfunctionalized alkane.[119] A strong base such as lithium diisopropylamide (LDA, pKa of conjugate acid ~36) is appropriate for this procedure, which is performed on a suspension of Br-CMK3 in tetrahydrofuran (THF) solution at lower temperatures (-8 °C, Figure 40).

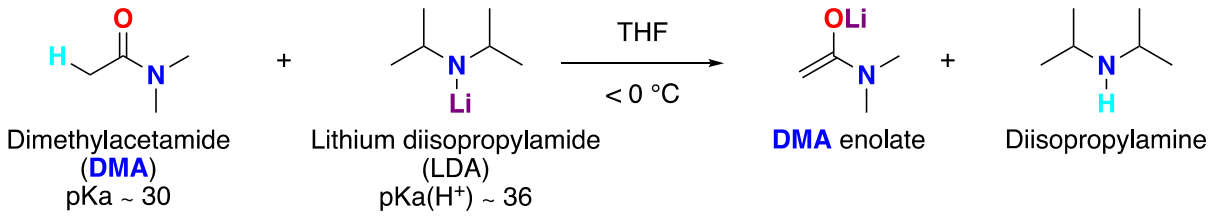

Figure 40. Formation of the DMA nucleophilic species by deprotonation with LDA to form an enolate.

The choice of LDA is important since it is non-nucleophilic, which decreases its chances of direct bromide displacement on Br-CMK3. Once added, LDA can remove the acidic α C-H proton from DMA forming an *enolate*. Amide enolates are potent nucleophiles,[124] which can displace bromide from the Br-CMK3 surface and create a C-C bond (Figure 41). For this reaction to run efficiently, it is of the utmost importance to establish and maintain anhydrous conditions since H_2O (pKa ~15.7) will prematurely quench both LDA and the DMA enolate *via* proton transfer. Subsequent warming of the reaction to room temperature allows the reaction to proceed more quickly while a large excess (10 equivalents relative to Br in Br-CMK3) of LDA neutralizes any acidic groups on the Br-CMK3 surface (*e.g.* alcohols, carboxylic acids). A small excess of DMA (3 equivalents relative to Br in Br-CMK3) and a tetrabutylammonium iodide (TBAI) catalyst help to maximize the surface group yield. TBAI is expected to behave similarly to NaI for sulfite substitution (Figure 39). After stirring at room temperature for 24 hrs, the reaction is quenched first with ethanol (EtOH) then H_2O.

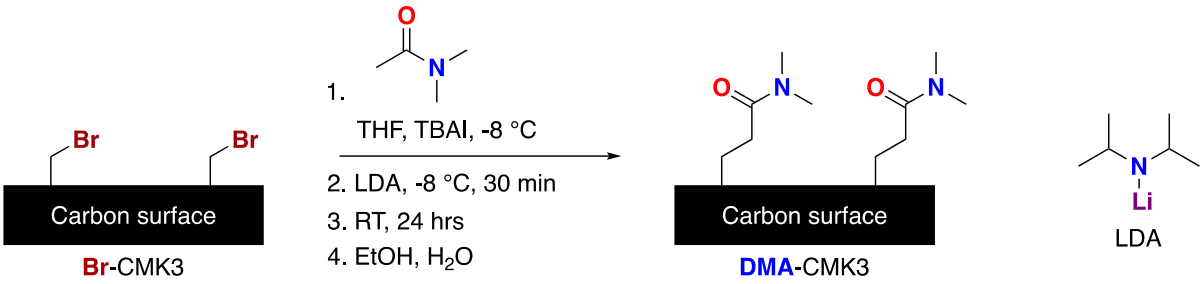

Figure 41. Synthesis of DMA-CMK3 by nucleophilic substitution with a DMA enolate.

A similar reaction can be performed with a diamide like N,N,N',N'-tetramethylmalonamide (TMMA). In this case, two amide carbonyl groups flank the same methylene (CH_2) group, making these α C-H protons even more acidic; TMMA is estimated to have a pKa between 18 and 20. The increased acidity allows a weaker base like lithium hexamethyldisilamide (LiHMDS, pKa of conjugate acid ~26) to be used (Figure 42).

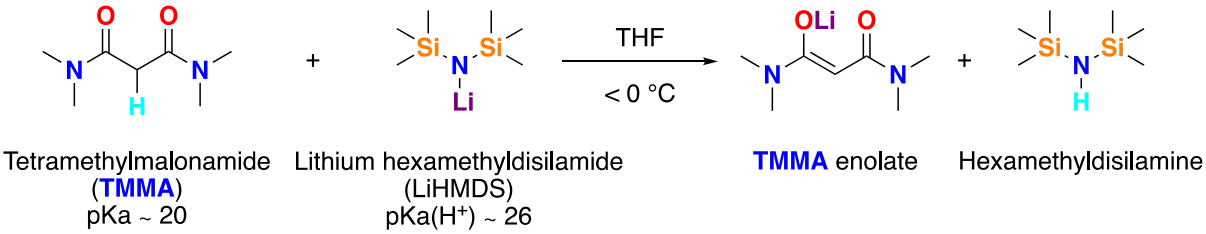

Figure 42. Formation of the TMMA nucleophilic species by deprotonation with LiHMDS to form an enolate.

The increased acidity comes at a cost, however, since the same group also makes the TMMA enolate bulkier and hence less reactive for substitution reactions. Therefore, this reaction was heated to reflux (80 °C) with an extra-large excess of both LiHMDS and TMMA (> 13 equivalents relative to Br in Br-CMK3) to increase the rate of the reaction (Figure 43). As with the DMA, a tetrabutylammonium iodide (TBAI) catalyst is used to further facilitate TMMA substitution.

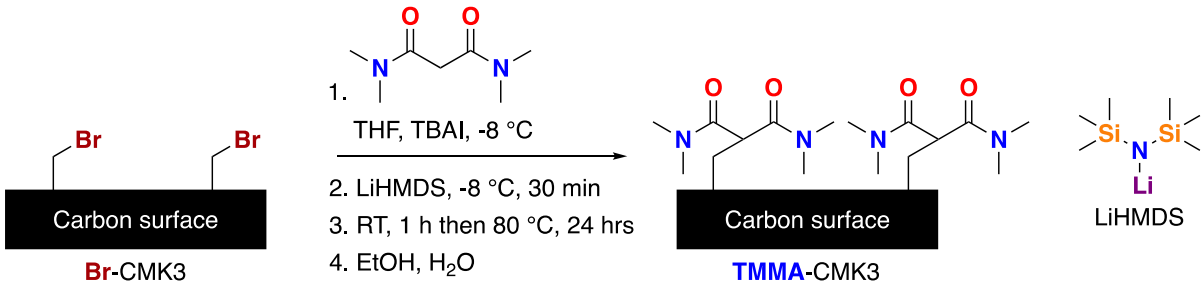

Figure 43. Synthesis of TMMA-CMK3 by nucleophilic substitution with a TMMA enolate.

As before, these carbons were studied by EA and XRF to quantify their yields and residual Br loadings (Table 15). The starting Br-CMK3 sample had a Br loading of 0.65 mmol g^{-1} and sulfite substitution using Na_2SO_3 resulted in a rather low yield loading of 0.34 mmol g^{-1} or of *ca.* 50% (Table 15, Entry 1). This yield indicates that, under these conditions, sulfite is a weaker nucleophile compared to azide but similar to iodide, which had yields of *ca.* 85% and 59%, respectively (Table A24 in Appendix; Table 14, Entry 1). The similar performance between NaI and Na_2SO_3, which contained a NaI catalyst, suggests that NaI could be the limiting factor in sulfite substitution. Exchanging the counter cation on $NaSO_3$-CMK3 for Li only results in a 2% decrease in the sulfite loading, providing evidence for covalent attachment to the surface since any unbound sulfite species would be washed away. The residual Br loading for both was 31%, demonstrating an incomplete reaction, although a large portion of this Br is likely anionic bromide, as determined by XPS (Figure 48a). The combined yield of sulfite and residual Br is *ca*. 80%, which leaves about 20% of the starting Br unaccounted for.

Table 15. Substitution of Br on Br-CMK3 using sulfite and amide nucleophiles.

Entry	Initial Br loading (mmol g^{-1})	Nucleophile (X)	X loading (mmol g^{-1})		Yield (%)	
1	0.65	Sodium sulfite (Na_2SO_3)	0.34 §,* (0.20)$^{\S,\#}$	0.32$^{\nabla}$ (0.20)$^{\nabla,\#}$	52§ 31§	49∇ 31$^{\nabla}$
2	0.65	N,N-dimethylacetamide (DMA)	0.74^ (0.20)$^{\#}$		115 (31)	
3	0.65	N,N,N',N'-tetramethylmalonamide (TMMA)	0.37^ (0.27)$^{\#}$		57 (42)	

§ -Determined for $NaSO_3$-CMK3
∇-Determined for $LiSO_3$-CMK3
-Residual bromine loading determined by XRF
* -Determined by sulfur EA
^ -Determined by nitrogen EA

In the synthesis of DMA-CMK3, a higher than expected yield was achieved (115%, Table 15, Entry 2). Together with a non-negligible residual Br content (31%), this yield indicates that a large portion of DMA enolate nucleophiles react with other functionality on the carbon surface. Different side reactions are possible for DMA compared to EN and include addition to a surface aldehyde, ketone, or ester (Figure 44). In contrast to DMA, the synthesis of TMMA-CMK3 results in a much lower yield of 57% (Table 15, Entry 3). Thus, as expected, TMMA is a worse nucleophile compared to DMA even at higher temperatures and concentrations. With a residual Br content of 42%, a total of 99% of the Br can be accounted for indicating few side reactions on TMMA-CMK3.

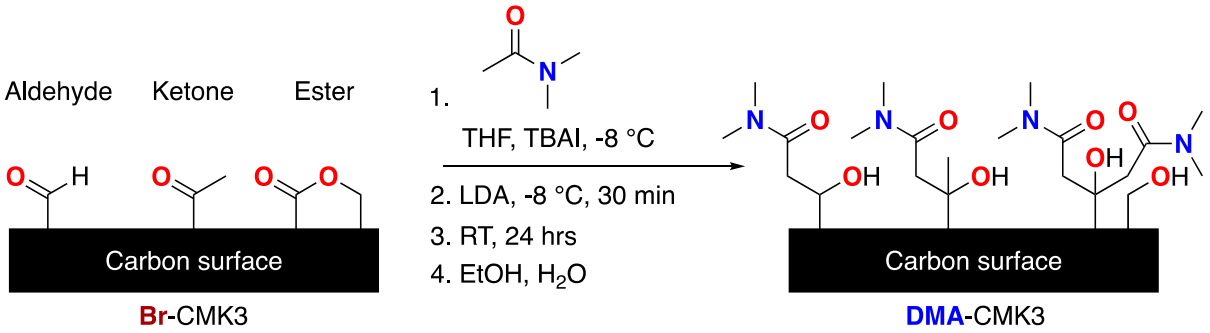

Figure 44. Possible side reactions between the DMA enolate and the native oxide layer of Br-CMK3 to account for the >100% yield of DMA-CMK3. Possible side reactions include addition to aldehydes, ketones, and esters, resulting in a covalently bonded amide group with an alcohol side product. The DMA enolate would presumably add twice to an ester group as the intermediate ketone is more reactive towards addition than the starting ester.

6.11 CuAAC functionalization of N_3-AC

The presence of surface azides on N_3-AC allows for the possibility of surface functionalization by a means other than direct nucleophilic substitution. The copper(I)-catalyzed azide-alkyne cycloaddition reaction (CuAAC) is an efficient, robust coupling reaction *via* which attaching nearly any group to the carbon surface becomes possible. That is, terminal alkynes, the coupling partner to the surface azides on N_3-AC, are easy to incorporate into most molecules,[105] which drastically increases the number of possible functionalities one could graft to the carbon surface.[111, 115, 122] As a model coupling partner, ethynylferrocene (Fc) was chosen as an elemental tag since Fe is easily quantified with XRF. Electrochemistry experiments are also possible with ferrocenes tethered to electrode surfaces, but this option was not explored.[111, 115] Two trials of CuAAC on N_3-AC with Fc to form Fc-AC resulted in yields of nearly 90% as determined by Fe XRF (Table A25 in Appendix, Figure 45). Encouragingly, the matching of the N loadings by EA (0.77 and 1.03 mmol g^{-1}) to the Fe loadings by XRF (0.78 and 1.02 mmol g^{-1}) reveals near quantitative coupling of Fc to the surface

with limited physisorption of Fc. In XPS, the Fe $2p_{3/2}$ region exhibits the distinct features of Fe(II), supporting the incorporation of Fc onto the AC surface (Figure 46, right). Additionally, the N 1s region of the XPS spectrum of Fc-AC displays features consistent with previous azide to triazole conversions on a carbon surface (Figure 46, left).[111] The two-step yield in converting Br-AC to N_3-AC then to Fc-AC averages near 75%, showing the synthetic efficiency of these reactions.

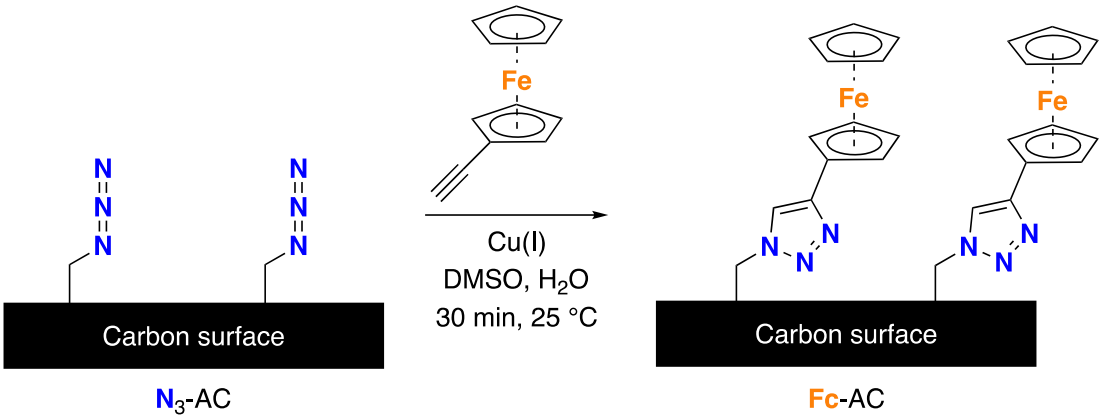

Figure 45. Copper(I)-catalyzed azide-alkyne cycloaddition reaction (CuAAC) of ethynyl ferrocene on N_3-AC.

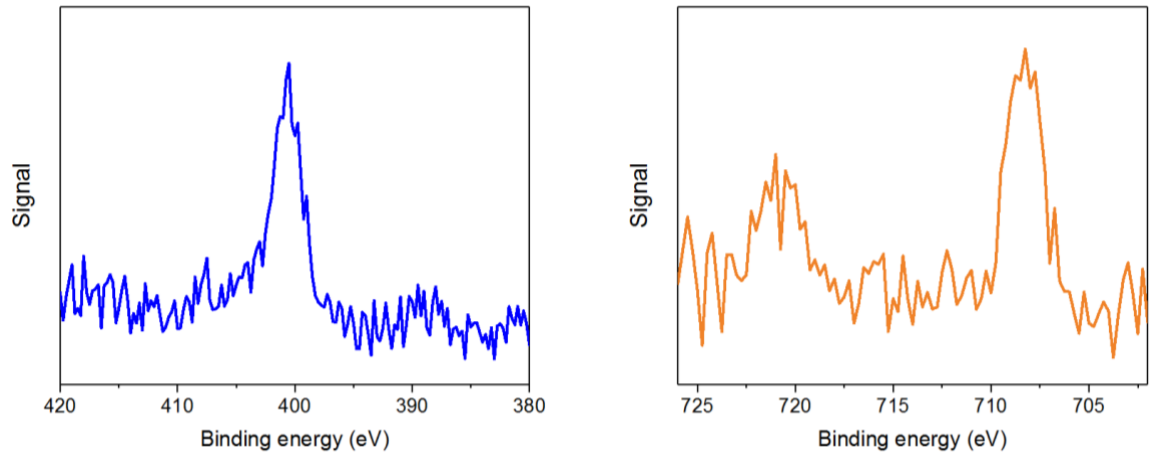

Figure 46. XPS spectra of Fc-AC: N 1s region (left), and Fe $2p_{3/2}$ region (right).

6.12 Further characterization of surface functionalized CMK3

By virtue of being used as battery electrodes, the functionalized CMK3 carbons were subjected to additional characterization to see the effects of functionalization on their porosity, morphology, atomic structure, and electrochemistry. The techniques chosen were XPS, nitrogen-sorption, SAXS, XRD, SEM, and CV. The samples are analyzed in the two batches as shown in Table 16 since each synthesis started from a different CMK3 batch. Both sets contain CMK3, Br-CMK3, and EN-CMK3, which are distinguished by the number 1 or 2 after their name. The second set of these carbons, CMK3-2, Br-CMK3-2, and EN-CMK3-2, were used in both Paper 3 and 4.

Table 16. Summary of CMK3 samples for Li-S battery cathodes.

Batch	Used in papers	Sample name in thesis	Surface group loading (mmol g^{-1})	Yield (%)	Residual Br loading# (mmol g^{-1})	Previous reference
1	2	CMK3-1	0	N/A	N/A	N/A
		Br-CMK3-1	0.60#	N/A	N/A	Table 13, Entry 4
		EN-CMK3-1	0.80	133	<0.1	Table 14, Entry 5a
2	3 and 4	CMK3-2	0	N/A	N/A	N/A
		Br-CMK3-2	0.65#	N/A	N/A	Table 13, Entry 5
		EN-CMK3-2	0.91*	140	0.14	Table 14, Entry 5b
	3	DMA-CMK3	0.74*	115	0.20	Table 15, Entry 2
		TMMA-CMK3	0.37*	57	0.27	Table 15, Entry 3
	4	$NaSO_3$-CMK3	0.34^	52	0.20	Table 15, Entry 1
		$LiSO_3$-CMK3	0.32^	49	0.20	Table 15, Entry 1

-Determined by bromine XRF
* -Determined by nitrogen EA
^ -Determined by sulfur EA

In XPS, the previous discussion in Section 6.6 shows that the Br species on Br-AC and Br-CMK3 is bonded to a carbon since it has binding energy of *ca.* 71 eV (Figure 27). For both batches of Br-CMK3, a small shoulder peak around 68 eV was observed. As this binding energy corresponds to anionic bromide,[116-117] the presence of this peak shows that both batches of bromomethylated starting material likely have reasonable quantities of bromide anions trapped in their pores. In the case of Br-CMK3-1 (Figure 47, left), all Br, both bromomethyl and anionic, is removed upon boiling in neat EN and large N signal is observed (Table 17). In the N 1s spectra (Figure 47, right), a signal at *ca.* 400 eV is observed, which is consistent with an amine.[44, 125]

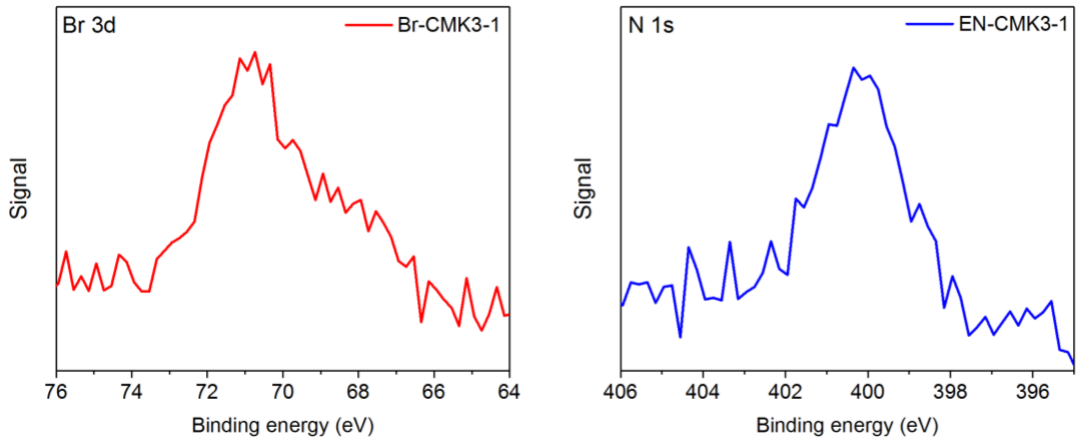

Figure 47. XPS spectra of Br-CMK3-1 (Br 3d region, left) and EN-CMK3-1 (N 1s region, right). The spectrum for Br-CMK3-1 is reproduced from Figure 27.

Table 17. XPS of the first batch of functionalized CMK3. Units are atomic %.

Sample	C 1s	N 1s	O 1s	Br 3d
CMK3-1	95.98	0	4.02	0
Br-CMK3-1	91.95	0	7.74	0.32
EN-CMK3-1	94.66	1.32	4.01	0

In the second batch, this Br content is not reduced to zero upon substitution with any nucleophile, including EN (Table 18). The relative Br content as determined by XPS agrees well with the relative residual Br loadings as determined by XRF (Table 16). In the Br 3d spectra (Figure 48a), the intensity of the peak at 70.5 eV is reduced considerably upon substitution, similar to the Br 3d peak for N_3-AC (Figure 35), while the peak at 68 eV retains its intensity. The constant intensity of the 68 eV peak suggests that Br-CMK3-2 has bromide anions trapped within its pores but, unlike Br-CMK3-1, the nucleophilic substitution conditions are not enough to dislodge these anions from the carbon surface. The relative intensities of the peak at 70.5 eV match well to the substitution efficiencies as determined by the yields (EA) and the residual Br content (XRF) of the substituted carbons (Table 16). The results from all three techniques indicate that, under the conditions used, the order of nucleophilic substitution efficiency on Br-CMK3 is EN > DMA > Na_2SO_3 > TMMA. The super high efficiency of EN could be due, at least in part, to the fact that it was used as a neat reagent, which gives it a much higher effective concentration (*ca.* 15,000 mM or 30,000 mM in terms of primary amines) compared to that used for DMA (*ca.* 50 mM), TMMA (*ca.* 180 mM), and Na_2SO_3 (*ca.* 500 mM).

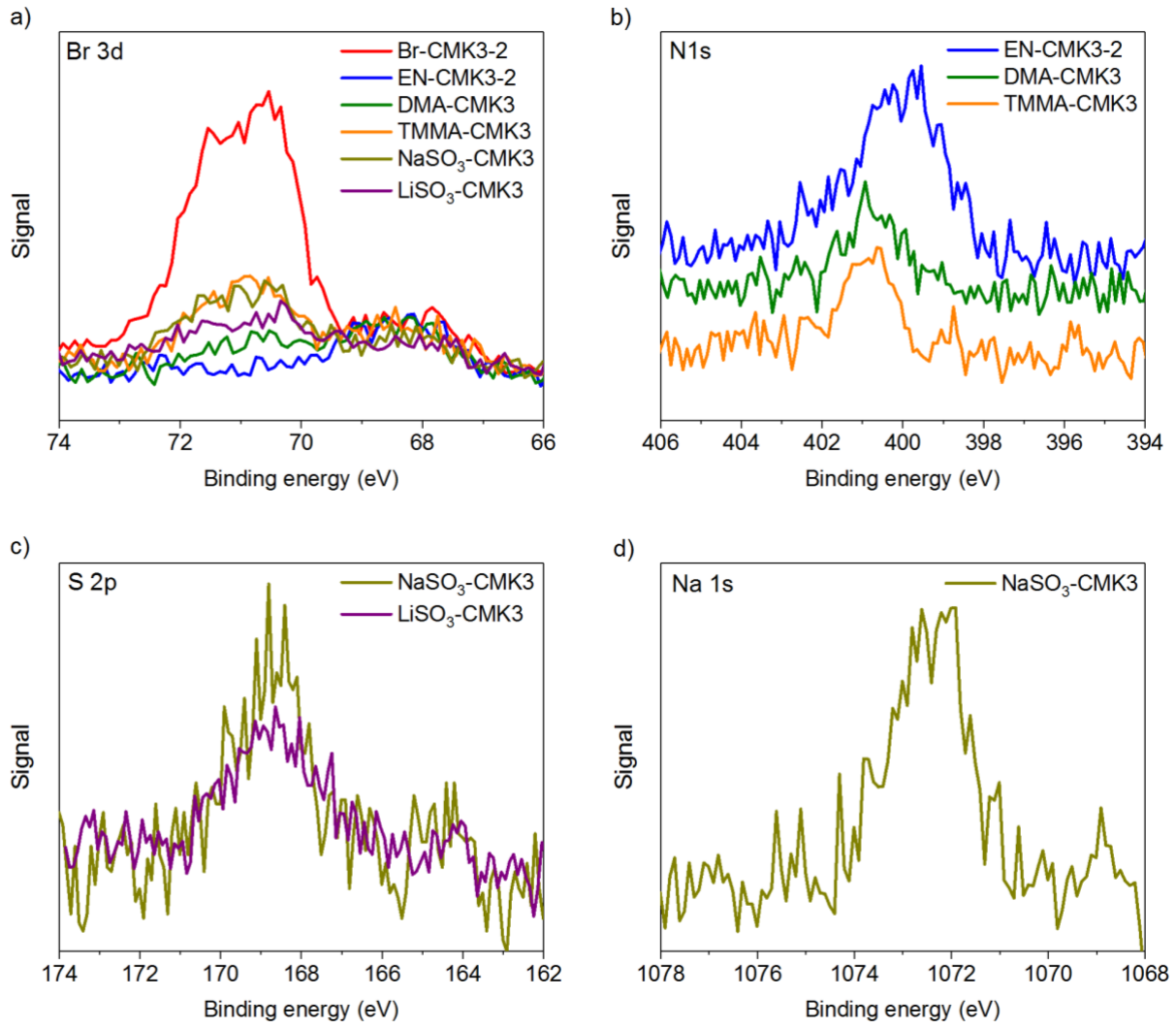

Figure 48. Summary of XPS spectra for the second batch of functionalized CMK3: ***a)*** *Br 3d spectra for Br-CMK3-2 and all substituted samples,* ***b)*** *N 1S spectra for EN-CMK3-2, DMA-CMK3, and TMMA-CMK3,* ***c)*** *S 2p spectra for $NaSO_3$-CMK3 and $LiSO_3$-CMK3, and* ***d)*** *Na 1s spectrum for $NaSO_3$-CMK3.*

Table 18. XPS of the second batch of functionalized CMK3. Units are atomic %.

Sample	C 1s	N 1s	O 1s	Br 3d	Na 1s	S 2p
CMK3-2	94.00	0	6.00	0	0	0
Br-CMK3-2	93.66	0	5.82	0.52	0	0
EN-CMK3-2	92.25	2.35	5.29	0.11	0	0
DMA-CMK3	92.53	0.80	6.51	0.16	0	0
TMMA-CMK3	92.53	0.83	6.43	0.21	0	0
$NaSO_3$-CMK3	92.05	0	7.03	0.17	0.35	0.40
$LiSO_3$-CMK3	90.69	0	9.03	0.10	0	0.17

The N content of EN-CMK3 in XPS is much higher compared to both DMA-CMK3 and TMMA-CMK3 (Table 18) in line with its higher yield and overall N content (EA, 1.88 mmol N g^{-1}). The two amide-functionalized samples have very similar N contents as determined by XPS, which closely matches their N loadings (EA, each at 0.74 mmol N g^{-1}). In the N 1s spectra (Figure 48b), both DMA-CMK3 and TMMA-CMK3 show weaker signals than EN-CMK3 as expected, but their spectra are also shifted to higher binding energies by about 1 eV. This shift is likely a result of the electron-withdrawing carbonyl group adjacent to the N atom. Such a change in the spectrum is consistent with an amide group relative to an amine.[44] This 1 eV shift gives strong evidence for amide substitution of bromide as opposed to other potential N-based nucleophiles such as the LDA or LiHMDS bases. Additionally, the complete lack of iodine from the TBAI catalyst and silicon from LiHMDS as determined by both XPS and XRF supports amide grafting to the CMK3 surface.

For the sulfite-substituted carbons, somewhat weak signals are observed at *ca.* 169 eV (Figure 48c) in the S 2p XPS spectra, which is consistent with an oxidized S center such as sulfonate or sulfone.[126] For $NaSO_3$-CMK3, sodium was detected (Figure 48d) but not for $LiSO_3$-CMK3, which supports cation substitution on the surface groups. The lack of any fluorine on $LiSO_3$-CMK3 indicates that very little of the LiFSI salt used for ion exchange remains. Overall, the XPS spectra for $NaSO_3$-CMK3 and $LiSO_3$-CMK3 provide strong evidence for lithium sulfonate ($LiSO_3$) grafting to the CMK3 surface.

The last element to be studied is O, which can be compared across all samples within a given batch due to the native oxide layer of amorphous carbons. Shifts in this spectrum could indicate significant changes in the oxide layer and/or presence of the desired O-containing functional groups (*e.g.* sulfonate, amides). In the first batch (Figure 49, left), the spectrum for Br-CMK3-1 is noticeably different from either its predecessor (CMK3-1) or successor (EN-CMK3-1). The higher intensity of the Br-CMK3 spectrum relative to either sample reveals an increased density of O species, which is reflected in its much higher O content (*ca.* 2x, Table 17), while its shift to lower binding energies suggests that more of these groups contain carbonyls.[44] As discussed in Section 6.9, the yield for EN-CMK3-1 was 133% with minimal decrease in the N content recorded over months indicating covalent bonding to the surface. Therefore, some side reactions resulting in the covalent attachment of EN to the CMK3 surface must have occurred. The higher concentration of carbonyl groups on Br-CMK3-1 could account for these side reactions, since plausible reactions include EN condensation with aldehydes and ketones (Figure 37). Because such reactions remove O (as H_2O) from the surface, condensation reactions can also account for the drastic decrease in O species after treatment with EN.

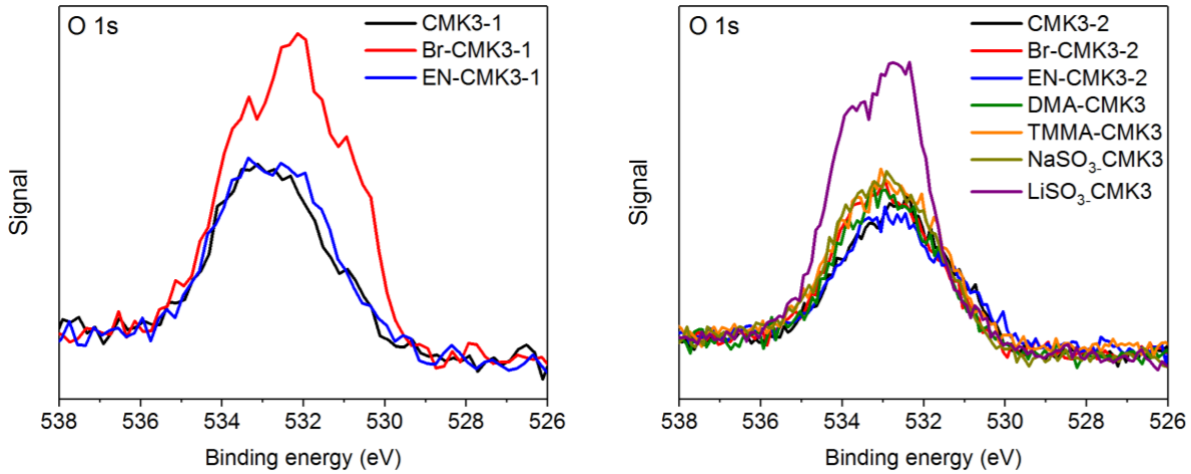

Figure 49. XPS O 1s spectra for the first (left) and second (right) batches of CMK3.

In the second batch of CMK3 (Figure 49, right), no significant shift in the O 1s spectra were observed, but differences in their intensities reflect possible side reactions as well as support grafting of O-containing groups to the carbon surface. Most importantly, no large increase in the O content or shift in the spectrum was recorded for Br-CMK3-2, signifying that the previous changes might not be reproducible. Nevertheless, a slight decrease in the O content was recorded for EN-CMK3-2 compared to both Br-CMK3-2 and CMK3-2 (Table 18), so condensation reactions could still be the reason behind the >100% yield for EN-CMK3-2. The higher O content of DMA-CMK3, TMMA-CMK3, $NaSO_3$-CMK3, and $LiSO_3$-CMK3 relative to both CMK3-2 and Br-CMK3-2 is also consistent with attaching O-containing amide and sulfonate groups to the carbon surface. The reason for the abnormally high O content of $LiSO_3$-CMK3 is unknown.

The next technique performed was nitrogen-sorption to see the effect of the two-step functionalization scheme on the carbon's porosity. The previous discussion on nitrogen-sorption (Section 6.5) showed that bromomethylation reproducibly lowers the amount of N_2 adsorbed. Substitution with any nucleophile further lowers the carbon's N_2 capacity (Figure 50a and c). The trend in N_2 adsorption is reflected in that, for both the first (Table 19) and second batch (Table 20), the smallest BET surface areas, BJH pore volumes and diameters were found for the substituted samples, followed by Br-CMK3, then finally the CMK3 starting material. The overall trend is that larger surface groups lead to lower surface areas, pore volumes and diameters since the starting bromomethyls are expected to be the smallest among all surface groups studied. Most importantly, however, the largest decreases in specific surface area were recorded for DMA-CMK3 and EN-CMK3-1 at *ca.* 22%, which is much less than the decrease found for other surface modification techniques, especially multi-layers formed from diazonium salts (*ca.* 50%).[40, 43] In both pore diameter distributions (Figure 50b and d), the CMK3 starting material has the largest pores at *ca.* 40 Å. Bromomethylation then substitution incrementally shift the distributions towards smaller pores with an equally consistent decrease in the overall area, the latter of which reflects the smaller pore volumes of the functionalized samples. The small decrease in pore diameter is consistent with monolayer functionalization of the CMK3 surface with minimal damage to the porous structure. Between the two batches, a small difference is observed. For both batches, modification of the carbon surface results in disappearance of the larger pores (> 35 Å) but, for the second batch, a higher number of smaller pores (< 35 Å) appears, which does not occur for the first batch. Instead, the distributions for the smaller pores overlap well in the first batch. This difference could indicate that the large pores in the first batch are "eaten up" or "disappear" during functionalization while in the second batch the large pores are "replaced" with smaller ones. The reasons behind this difference are unknown.

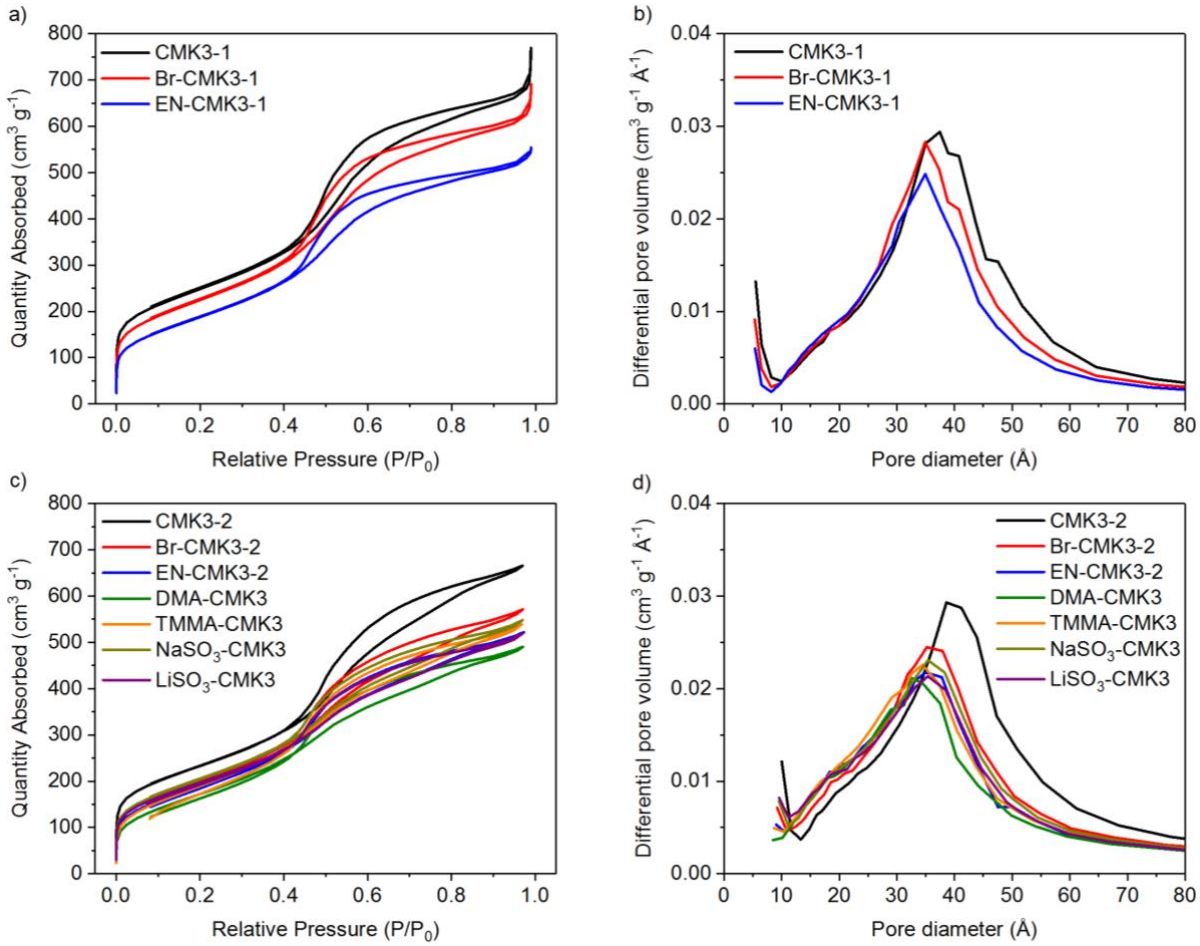

*Figure 50. Summary of nitrogen-sorption for both functionalized CMK3 batches: **a), c)** nitrogen isotherms and **b), d)** pore diameters distributions for the first (**a** and **b**) and second (**c** and **d**) batches. Pore diameter distributions are based on the adsorption isotherm.*

Table 19. Nitrogen-sorption of the first batch of functionalized CMK3.

Sample	BET surface area ($m^2\ g^{-1}$)	BJH pore volume ($cm^3\ g^{-1}$)*	BJH pore diameter (Å)*
CMK3-1	885	1.21	42.8
Br-CMK3-1	815	1.09	41.0
EN-CMK3-1	690	0.87	37.6

*Based on the adsorption isotherm

Table 20. Nitrogen-sorption of the second batch of functionalized CMK3.

Sample	BET surface area ($m^2\ g^{-1}$)	BJH pore volume ($cm^3\ g^{-1}$)*	BJH pore diameter (Å)*
CMK3-2	832	1.06	39.8
Br-CMK3-2	741	0.90	37.0
EN-CMK3-2	700	0.81	35.2
DMA-CMK3	645	0.77	34.7
TMMA-CMK3	704	0.84	35.0
$NaSO_3$-CMK3	732	0.87	35.8
$LiSO_3$-CMK3	715	0.82	34.9

*Based on the adsorption isotherm

The first batch of CMK3 carbons were also studied by SAXS, XRD, and SEM to reveal the impact of the two-step functionalization scheme on the CMK3 meso-structure, atomic structure, and morphology, respectively. The SAXS patterns for all three carbons are similar with no major shifts in the main peak at 1.2° (Figure 51, left), meaning that the decrease in pore diameter measured by nitrogen-sorption is not visible with SAXS. The similar intensities for all three traces signify that the CMK3 meso-structure is unperturbed. This stands in contrast to other surface modification techniques including oxidation[125] and diazonium functionalization,[43] both of which showed a drastic decrease in the SAXS intensity. In XRD, similar diffractograms are obtained for all three carbons (Figure 51, right), which show the two broad peaks of amorphous carbon near 23° and 43°.[8] Thus, the atomic structure of the carbon remains unchanged during bromomethylation and subsequent substitution. SEM images obtained at several magnifications (1k, 5k, 10k, and 50k) show no discernable differences in particle size or shape (see SI in Paper 2), demonstrating that both reactions have minimal impact on the CMK3 morphology. Overall, the results from all three techniques showcase the mild reaction conditions of this two-step method as no damage to the carbon's structure was detected.

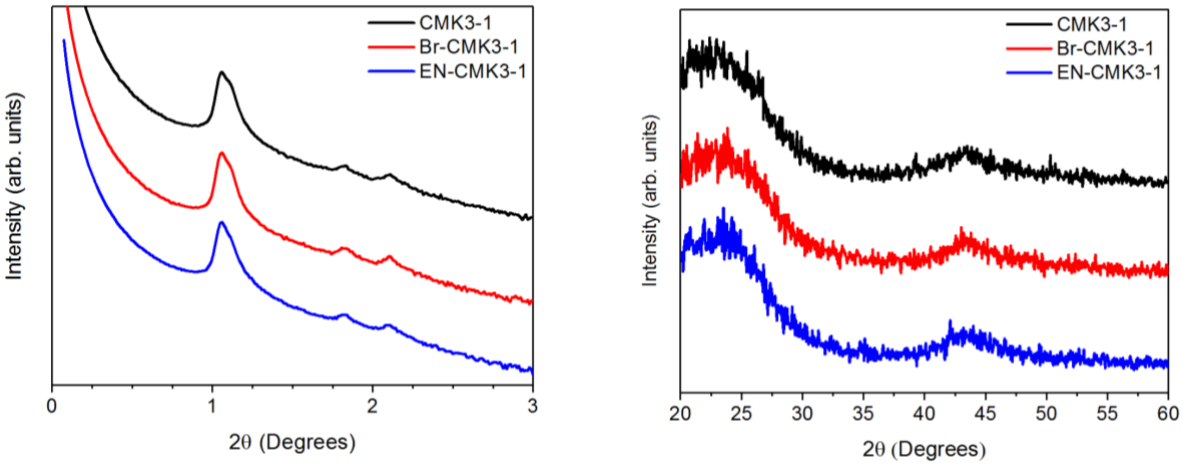

Figure 51. SAXS patterns (left) and XRD plots (right) for the first batch of CMK3.

Given the application of Li-S batteries, the CMK3 carbons were also studied electrochemically *via* CV. Cells for CV were constructed in the same way as for Li-S batteries except the electroactive S (in the form of Li_2S_8) was excluded from fabrication and CV was conducted with a blank electrolyte. This analysis was performed in order to determine the background electrochemical signal from both the cathode and the electrolyte. Two electrolytes were 1 M lithium bis(trifluoromethanesulfonyl)imide (LiTFSI) in 1:1 dioxolane-dimethoxyethane (DOL-DME) with or without 0.4 M lithium nitrate ($LiNO_3$) (electrolytes 1 and 2, Table 4). The samples studied as the working electrode in CV were: CMK3-1, EN-CMK3-1, DMA-CMK3, TMMA-CMK3, and $LiSO_3$-CMK3. Br-CMK3 and $NaSO_3$-CMK3 were not tested since they are synthetic intermediates and were not used in Li-S batteries. CMK3-2 and EN-CMK3-2 were not tested as very little difference was expected between batches. The CV program was meant to mimic battery cycling (see Section 3.4.1).

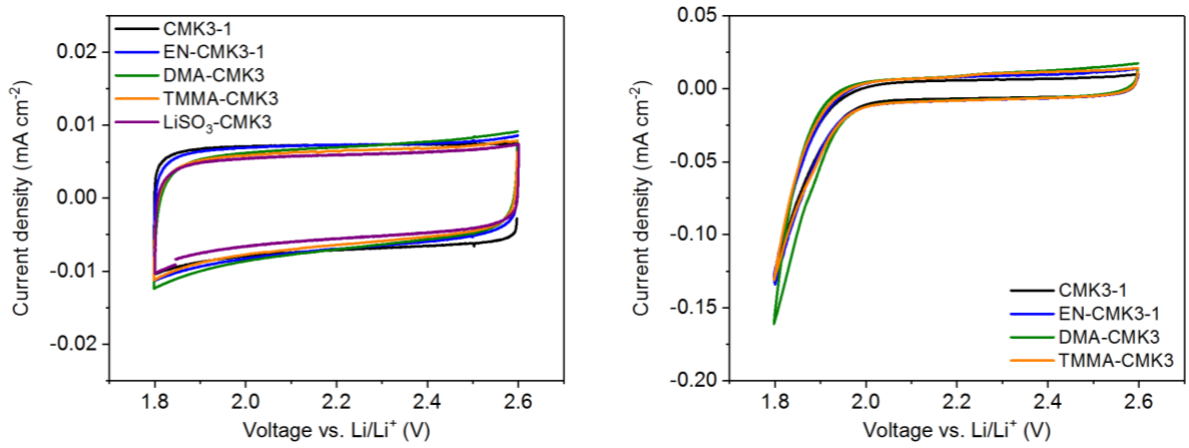

Figure 52. Cyclic voltammograms (CV) for modified CMK3 using two Li-S battery electrolytes. The CV on the right does not contain $LiNO_3$ while the one on the right contains 0.4 M $LiNO_3$.

For the electrolyte without $LiNO_3$ (Figure 52, left), rectangular voltammograms are obtained for all CMK3 working electrodes, which is indicative of a charging current, similar to a capacitor. The lack of any redox peaks demonstrates that the native oxide layer and all surface groups as well as all electrolyte components are redox inactive under the conditions and voltages used. The overlapping traces also show that the carbon's conductivity is not greatly altered from the CMK3 starting material, again demonstrating the mild reaction conditions used to make the functionalized carbons. With the addition of 0.4 M $LiNO_3$ (Figure 52, right), an irreversible peak is observed between 2.0 and 1.8 V, which is almost certainly due to nitrate reduction. Since this peak is similar among all CMK3 electrodes, the surface groups do not seem to impact nitrate reduction significantly.

In summary, the CMK3 characterization quantifies (EA and XRF) and confirms (XPS) the identities of the desired surface groups. It also reveals the retention of the CMK3 porosity and surface area (nitrogen-sorption), meso-structure (SAXS), atomic structure (XRD), particle morphology (SEM), and electrical conductivity (CV) after bromomethylation and substitution, highlighting several of the major advantages of this two-step method. Given this thorough characterization, the functionalized CMK3 carbons should serve well as a means to study surface chemistry in the context of Li-S batteries, which is the topic of the next section.

7 Applications of surface-modified carbons in lithium-sulfur batteries

7.1 Overview of the Li-S battery studies

The previous section discussed the synthesis of novel surface groups on high surface area carbon materials including AC, Vulcan and CMK3, which was made possible by the discovery of the two-step method of bromomethylation and nucleophilic substitution. In the current section, some of the modified CMK3 materials listed in Table 16 are used in lithium-sulfur (Li-S) batteries (Section 4.1). While Li-S are a next generation battery technology that holds promise for complementing the Li-ion energy storage technologies already available today, in the context of Papers 2-4 and this thesis, the Li-S cell was used more often as a platform on which to study these new carbon materials and the effect that the surface groups have on the cell cycling. In other words, certain battery metrics important to commercialization (*e.g.* areal S loading, electrolyte-to-S ratio) were not stressed and, instead, improving the relative performance compared to the unfunctionalized control was always the main objective. By doing so, we hoped to gain insight into the electrochemical processes within the Li-S cell.

The Li-S battery results are discussed in the order Paper 2, then 3, then 4 and are then discussed collectively at the end. The names and trace colors are the same as those used in the publications. Since the two batches of CMK3 and EN-CMK3 are not compared directly (*i.e.* the same electrolyte was not used), the -1 or -2 after their names is removed. Moreover, no significant difference is expected between the batches given their similar properties (Section 6.12).

7.2 Initial testing of modified CMK3 in Li-S batteries (Paper 2)

7.2.1 Selection of the first functionalized surface: EN-CMK3

The first application of modified CMK3 carbons in Li-S batteries was purely proof-of-concept so only two carbons were selected: the control and its two-step functionalized derivative. The control would be, of course, unmodified CMK3. The question was which group to install on the functionalized surface to best benefit battery cycling. The key for selecting an effective group lies in understanding the Li-S chemistry (Section 4.1.3, Figure 6). When it undergoes reduction, elemental sulfur (S_8) has its solubility and polarity changed drastically; while S_8 is a poorly soluble, non-polar molecule,[60-63] the partially reduced intermediates, called lithium polysulfides (LiPS, Li_2S_n, $4 \leq n \leq 8$), typically dissolve well and are much more polar.[64] The final discharge products lithium disulfide (Li_2S_2) and lithium sulfide (Li_2S) are poorly soluble ionic solids.[39]

Since most carbons, including CMK3, are naturally hydrophobic, S_8 possesses reasonably strong interactions with the carbon surface. The polar discharge products, on the other hand, experience weaker interactions.[127] In selecting a group to attach to the CMK3 surface, it was postulated that a polar group would help benefit the battery cycling most. That is, such a group would allow the carbon surface to bind more strongly with the LiPS and other polar S species, thereby facilitating electron transfer at the electrode-electrolyte interface.

With its synthetic simplicity and strongly polar nature, ethylenediamine (EN) was selected as the first nucleophile. The high surface loadings of EN should also amplify its effects on the cell cycling (Table 16). The attachment of amines to the carbon surface also follows directly from a previous study, which used a diazonium salt functionalization to graft aniline groups to the CMK3 surface.[39] In this study, it is hypothesized that the aniline groups bind Li cations and facilitate the formation of Li_2S on the surface. If true, then the more basic aliphatic amines of EN (pK_a of conjugate acid, EN = 10; aniline = 4) and chelating ability should enhance interactions with lithium cations. In addition, hydrogen bonding between the anionic LiPS and the EN N-H groups could further increase LiPS retention (Figure 53).

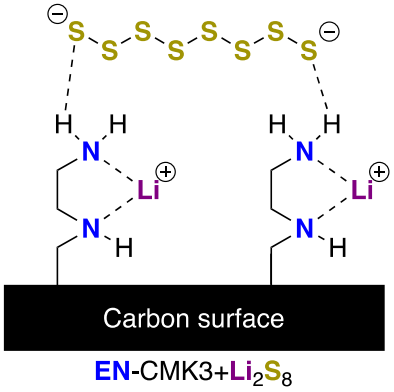

Figure 53. Illustration of the polar interactions between the surface EN groups of EN-CMK3 and a LiPS (Li_2S_8).

7.2.2 Sulfur impregnation: melt diffusion vs. catholytes

To use any given carbon in a Li-S battery, S must be incorporated into the battery architecture in some fashion. S impregnation can occur *via* a variety of methods (Section 4.1.5). One of the most common methods is melt diffusion of S_8 into the pores of the carbon before it is fabricated into a cathode for use in a battery. This procedure involves heating the carbon-sulfur mixture at the low viscosity point of S_8 (155 °C). The S-infused samples are denoted with a *+S* at the end of their name to distinguish them from their S-free precursors.

Although this procedure is relatively simple, the high temperatures and liquid state can make S_8 reactive, including deteriorating the surface groups of EN-CMK3. Indeed, upon heating CMK3 or EN-CMK3 with S_8, strong gas evolution was observed for the latter but not for the former, which is likely indicative of S reacting with the EN surface groups. Nevertheless, EN-CMK3+S had an EN loading of 0.39 mmol g^{-1} as determined by EA, so EN, in some form, must remain in the C-S composite. After fabrication into cathodes, CMK3+S and EN-CMK3+S were tested in cells using 1 M LiTFSI with 0.4 M $LiNO_3$ in 1:1 DOL-DME as the electrolyte (Electrolyte 2, Table 4). Both cells started at initial discharging capacities of *ca.* 1080 mAh g^{-1}, but the EN-CMK3+S cell loses more capacity more quickly compared to its unfunctionalized counterpart and does not reach a stable capacity after 50 cycles (Figure 54). The gas evolution combined with poor performance suggests that S_8 melt diffusion significantly degrades the EN groups of EN-CMK3+S. For all future battery studies with functionalized CMK3 and Li-S batteries, S_8 melt diffusion was not attempted.

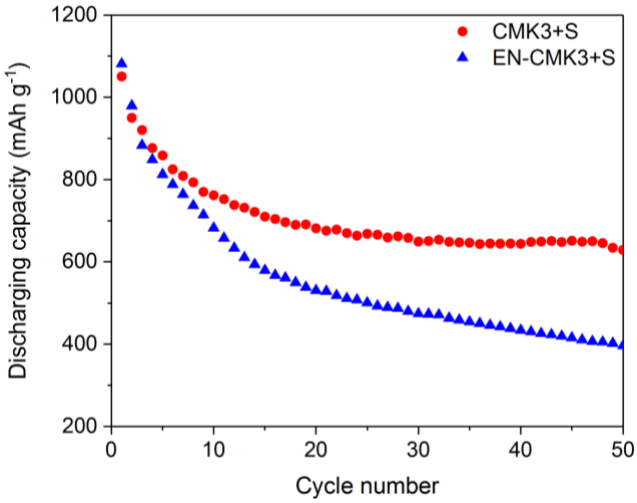

Figure 54. Discharging capacities at 0.1C of the S-infused CMK3 and EN-CMK3 cathodes.

Fortunately, many alternatives to melt diffusion are available which are much less likely to degrade the surface groups of the functionalized carbons. One such method is a catholyte cell, wherein the electroactive S is dissolved in the electrolyte; no direct impregnation of the cathode is necessary. Using a catholyte, the carbon surface is exposed to S species at only room temperature. The two catholytes chosen for this first

study contained 0.2 M Li_2S_8 with either 0.4 M $LiNO_3$ or 0.4 M LiTFSI as the supporting electrolyte salt and both use 1:1 DOL-DME as the solvent (Electrolytes 3 and 4, Table 4).

The catholyte with 0.4 M $LiNO_3$ was tested first given this salt's ability to greatly attenuate the LiPS shuttle (Section 4.1.4). Encouragingly, during the first cycle, the cell using EN-CMK3 cathodes now displayed about a 300 mAh g^{-1} higher capacity relative to unfunctionalized CMK3 when cycled at 0.1 C (Figure 55, left). This was the first instance of surface groups derived from bromomethylation benefiting battery performance. During subsequent cycles, both cells experience a large increase in capacity, the majority of which happens during the second cycle. This increase is ascribed to starting from unreduced S_8 instead of the partially reduced Li_2S_8 in latter cycles, thereby permitting additional reduction of S during subsequent discharges. As evidence for the new S starting material, the waveforms for both cells reveal that the first discharge voltage plateau near 2.4 V, which corresponds to S_8 reduction to Li_2S_8,[39, 59] becomes pronounced during the second cycle (Figure 56). Because of the extra charge compared to discharge in the first cycle, the initial Coulombic or charging efficiencies (ICEs) are 80-85% for both cells. Afterwards, the Coulombic or charging efficiencies (CEs) increase to >97% (Figure A67 in appendix). For all 50 cycles, EN-CMK3 maintains a *ca.* 300 mAh g^{-1} advantage over its unfunctionalized precursor.

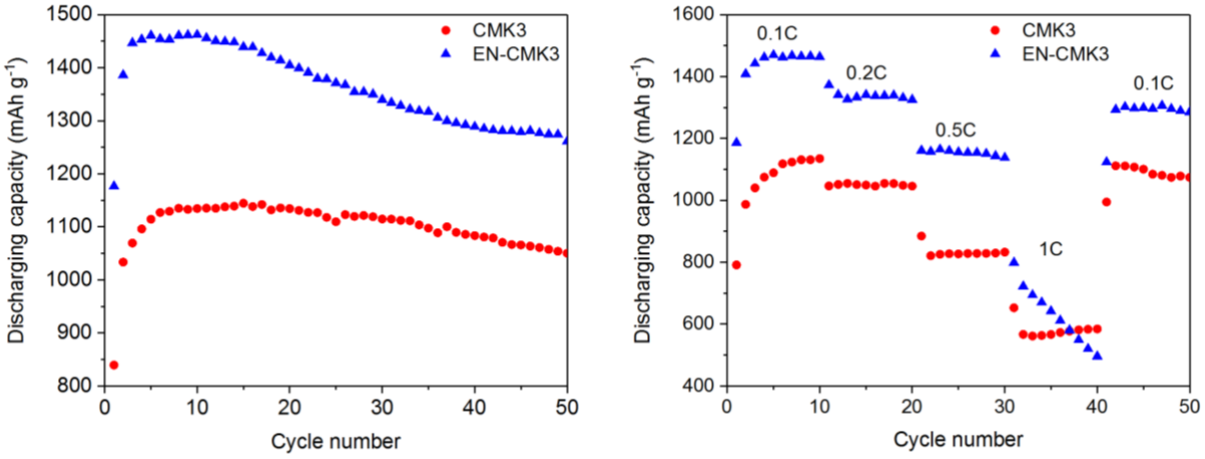

Figure 55. Discharging capacities at 0.1 C (left) and at variable C-rates (right) of catholyte/$LiNO_3$ cells and with a CMK3 or EN-CMK3 cathode.

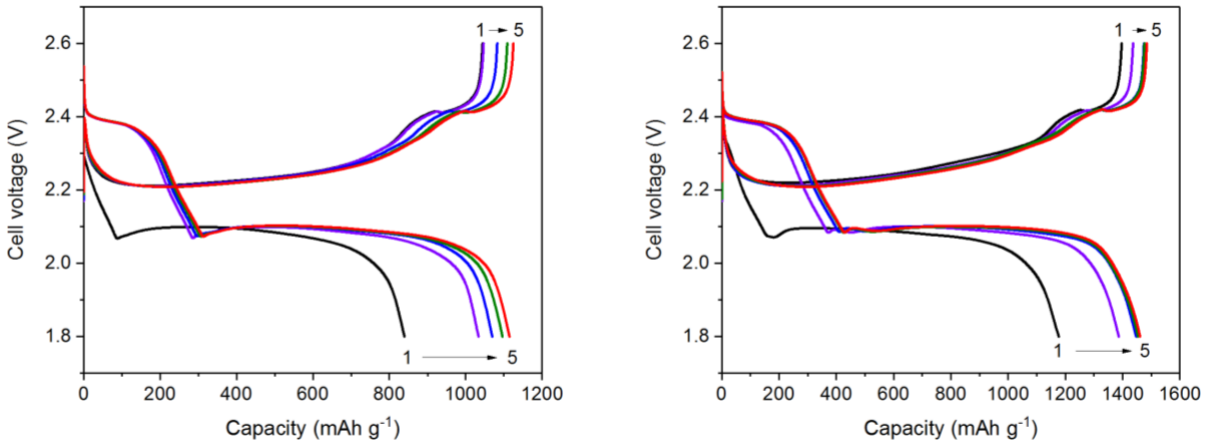

Figure 56. Waveforms at 0.1 C of catholyte/$LiNO_3$ cells for CMK3 (left) and EN-CMK3 (right). The cycles are color coded as follows: 1st black, 2nd violet, 3rd blue, 4th green, and 5th red.

Rate testing of duplicate cells showed that the surface EN groups increase the discharging capacity at all but the highest rate tested (1C; Figure 55, right). The reason for the steady loss of capacity during the ten cycles at 1C is unknown, but a plausible explanation could be that the surface groups struggle to keep up

with the S redox chemistry at higher applied currents. Nevertheless, returning to 0.1C showed that the loss of capacity at higher currents is reversible: the capacities for the final 10 cycles at 0.1C are similar for both cells using EN-CMK3 cathodes (*ca.* 1300 mAh g^{-1}). Overall, the functional groups of EN-CMK3 benefit the cell cycling by allowing for higher S utilization.

The second catholyte used LiTFSI as the supporting electrolyte in place of $LiNO_3$. The goal of this exchange was to see how the surface groups impact the LiPS shuttle. As discussed in Section 4.1.4, a strong LiPS shuttle manifests itself in the form of an extraordinarily long voltage plateau at *ca.* 2.35 V during charging and can last many times (> 10) the theoretical maximum. The long charging cycle results in a low ICE (< 10%). The importance of $LiNO_3$ is that it is known to attenuate the LiPS and greatly increase the ICEs to >95% (Section 4.1.7). Thus, by purposeful exclusion of this salt, the effect of the EN groups on the LiPS shuttle become readily apparent. The first cycles for CMK3 and EN-CMK3 cells using catholyte/LiTFSI cells are shown in Figure 57a and b.

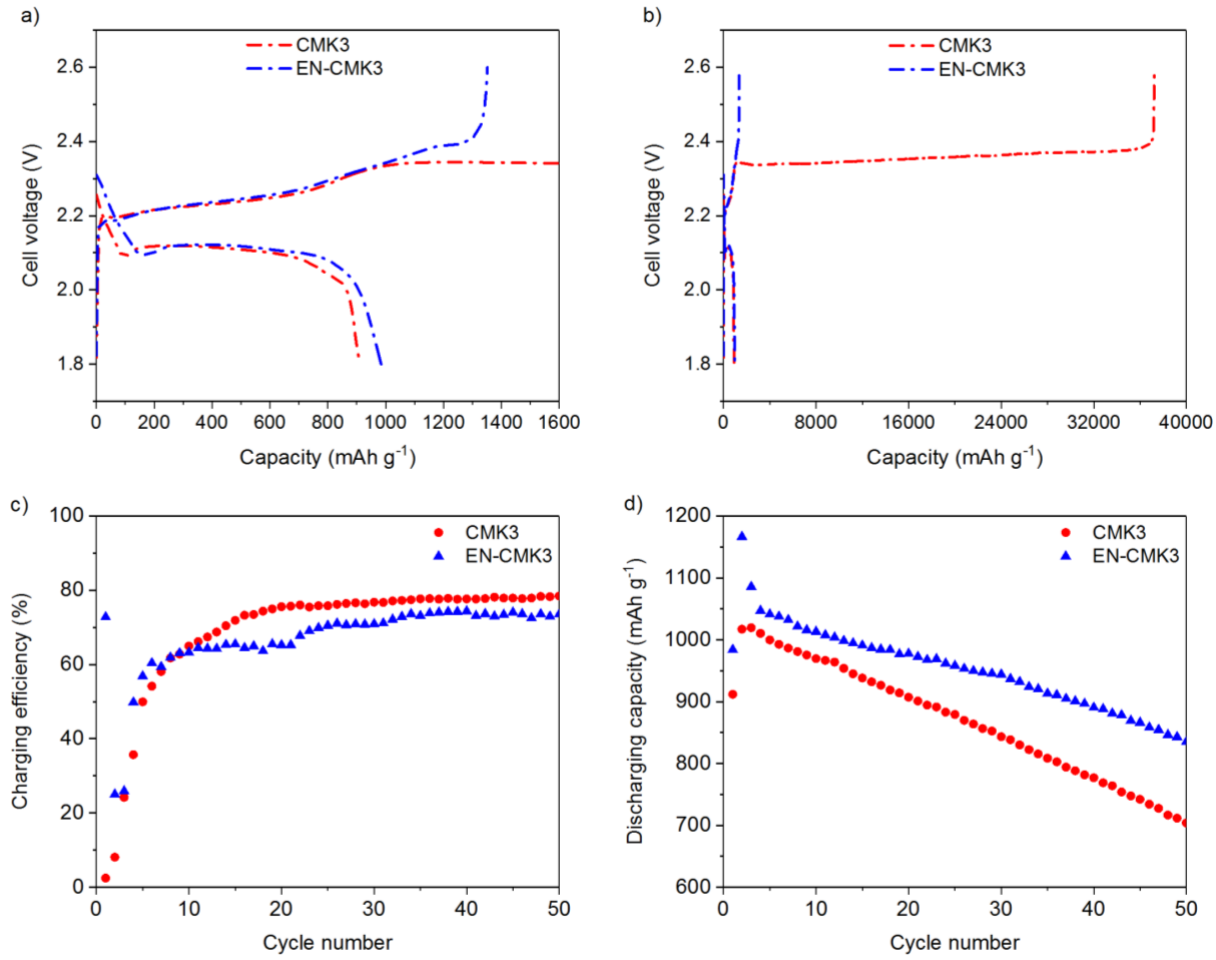

Figure 57. ***a)*** *and* ***b)*** *First cycle waveforms of catholyte/LiTFSI cells at 0.1 C with a CMK3 or EN-CMK3 cathode. The right graph contains the extended version of the left one in order to display the ultralong charging time required for the CMK3 cell.* ***c)*** *Charging efficiencies and* ***d)*** *discharging capacities at 0.1 C of catholyte/LiTFSI cells with a CMK3 or EN-CMK3 cathode.*

The first discharge reveals no significant difference between the two cells as both have similar capacities between 900 and 1000 mAh g^{-1}. However, the ensuing charging cycle reveals a stark difference between the two cathodes: whereas the functionalized cathode is able to charge in 8 h (1350 mAh g^{-1}), its unmodified analogue requires 222 h (37225 mAh g^{-1}). The corresponding ICEs are 73% and 3% respectively. This monumental decrease in charging time (or increase in ICE) lends evidence for strong interactions between the surface EN groups and the LiPS, which, in turn, limit the LiPS shuttle.

During the second cycle, the CE for CMK3 improves to 8% while that for the EN-CMK3 decreases to 25%, which shows that the EN groups cannot shut down the LiPS shuttle entirely. However, during the first five cycles, the cumulative charging times for CMK3 and EN-CMK3 are 351 and 84 hrs, respectively; the LiPS shuttle is, nevertheless, greatly decreased on the EN-CMK3 surface. Upon increase cycling, both cells reach CEs of *ca.* 75% (Figure 57c), which is much lower than the ca. 97% CEs achieved with the $LiNO_3$ catholyte (Figure A67 in Appendix); nitrate is still superior in increasing the CEs of the Li-S cell. For the cells with LiTFSI, they exhibit lower capacities and suffer from faster capacity fading (Figure 57d), which are consequences of their lower CEs. Encouragingly, the cells with EN-CMK3 cathodes show higher capacity and experience slower capacity fading compared to unmodified CMK3, again showing the measurable benefits that polar groups on the cathode surface can exert on the battery cycling.

7.2.3 Cyclic voltammetry to quantify the LiPS shuttle on modified CMK3

The final electrochemical test performed in Paper 2 was cyclic voltammetry (CV, Section 3.4.1). These tests were done to gain insight into the potential roles and redox activity of the EN surface groups, $LiNO_3$, and LiTFSI. As shown previously, in the absence of LiPS and $LiNO_3$, all modified carbons and the parent CMK3 show very similar rectangular voltammograms CMK3 (Figure 52, left; Section 6.12). The addition of 0.4 M $LiNO_3$ adds an irreversible reduction peak between 1.8- 2.0 V, but none of the functional groups greatly impact the current or voltage of nitrate reduction (Figure 52, right). Given these similarities, any impact the EN (or other) surface groups have on cell cycling is likely a result of their direct interaction with S species in the battery electrolyte.

CMK3 and EN-CMK3 cathodes were tested with both catholytes using the CV program detailed in Section 3.4.1. This CV program is meant to mimic constant current cell cycling as much as possible. In Figure 58, all four voltammograms show very similar reduction (discharging) peaks, one smaller feature at *ca.* 2.4 V and a larger peak at 2.0 V, which correspond to the reductions of S_8 and Li_2S_8, respectively.[39, 59] The similarity in voltages and peak sizes indicates that the discharging mechanism is not affected significantly by either nitrate or the EN groups. The only major difference is that, for the $LiNO_3$ cells, the peak at 2.4 V is larger compared to those of the LiTFSI cells, which supports their higher discharging capacities of the $LiNO_3$ cells from the constant current (CC) studies (Section 7.2.2).

In contrast, several sharp distinctions are made clear for the oxidation (charging) peaks. Two possible comparisons can be made in the CV traces: $LiNO_3$ *vs.* LiTFSI and CMK3 *vs.* EN-CMK3. First, a direct comparison of the electrolyte salts reveals a major difference in the oxidation or charging mechanism (Figure 58). With LTFSI (dotted traces), two separate peaks are observed with larger peak occurring at *ca.* 2.3 and a smaller one at *ca.* 2.5 V; with $LiNO_3$ (solid traces), these peaks are merged into one major one at 2.4 V with a shoulder peak at 2.5 V.

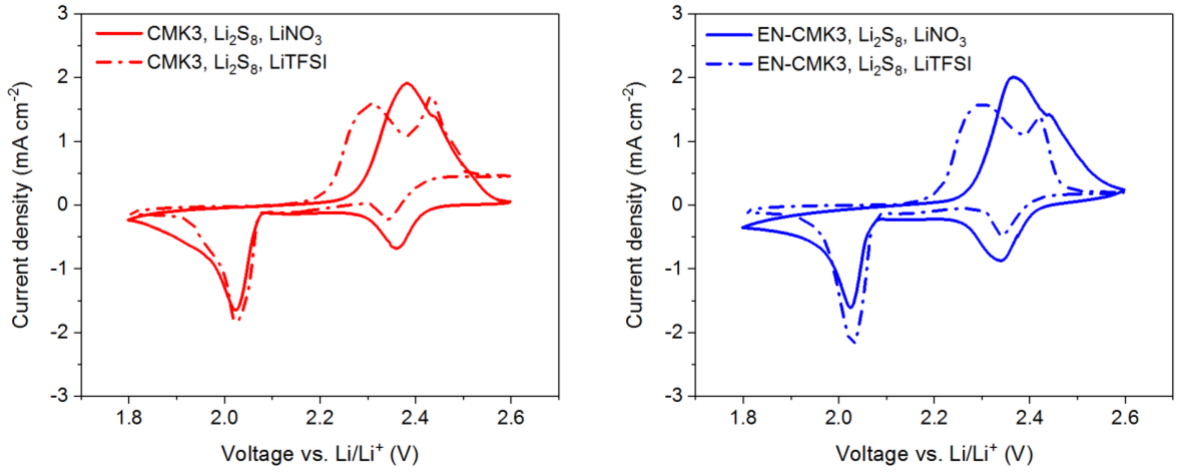

Figure 58. Cyclic voltammograms for CMK3 (red, left) and EN-CMK3 (blue, right) with Li_2S_8 using either electrolyte 3 (with $LiNO_3$, solid traces) or electrolyte 4 (with LiTFSI, dotted traces).

Interestingly, these changes in the oxidation peaks bare resemblance to changes in the charging waveforms in the CC studies (Figure 56, Figure 57a and b): while the discharge waveforms are rather similar in shape between Li salts, several key distinctions arise within the charging waveform (Figure 59). With LiTFSI, no voltage decrease occurs throughout the charging cycling and the waveform shows two main features: one sloped plateau around 2.25 V until *ca.* 800 mAh g^{-1} and a second flatter and much longer plateau at 2.35 V. The plateau at 2.35 V is directly connected to the LiPS shuttle since its length varies considerably depending on the strength of the LiPS shuttle while the slopped plateau at 2.25 V is consistent in length from cycle-to-cycle.

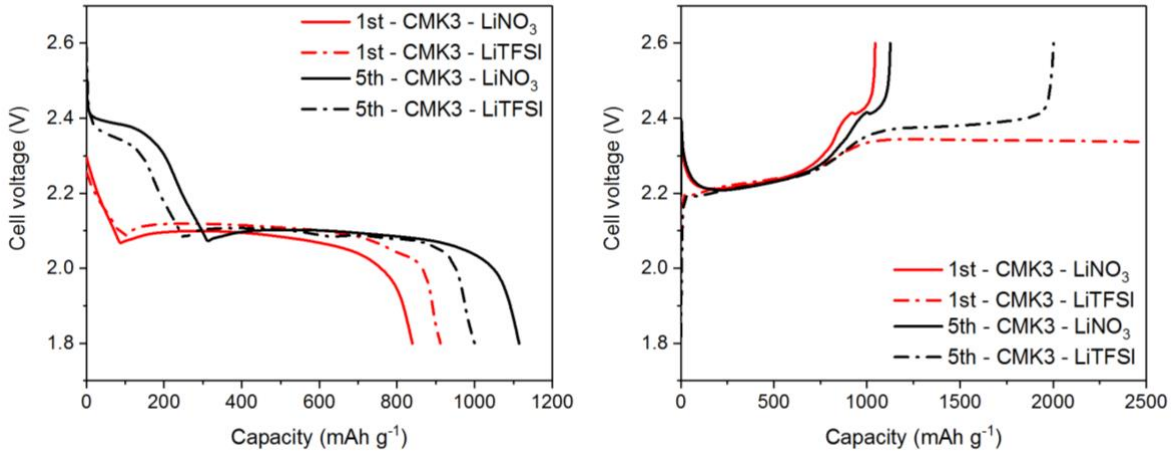

Figure 59. Comparison of 1st (red) and 5th (black) waveforms between catholyte cells with $LiNO_3$ (solid traces) and LiTFSI (dotted traces).

In contrast, with $LiNO_3$, the charging waveform starts out by *decreasing* in voltage from about 2.4 to 2.2 V before reaching a similar slopped plateau at 2.25 V. At the end of the slopped plateau, the $LiNO_3$ cell experiences a steeper rise in voltage until it reaches a short, flat plateau at 2.4 V. The plateaus in the CC studies map nicely onto the peaks in CV: with LiTFSI, the CC plateaus at 2.25 V and 2.35 V map onto the CV peaks at 2.3 V and 2.5 V, respectively; with $LiNO_3$, the slopped plateau at 2.25 V and short, flat plateau at 2.4 V correspond to the large CV peak at 2.4 V and small shoulder peak 2.5 V, respectively. The slight differences in voltages between the two techniques are attributable to the different current densities: the current density at the cathode is 0.23 mA cm^{-2} at 0.1C in the CC studies, which is about a factor of 10 less than the peak current density measured in the CV traces (*ca.* 2 mA cm^{-2}).

The CV traces shown in Figure 58 can be rearranged for a direct comparison of CMK3 to EN-CMK_3, which shows a couple of major differences (Figure 60). First, in the cells with LiTFSI, the oxidation peak at 2.5 V is significantly smaller for EN-CMK3 compared to CMK3. As this peak corresponds to the LiPS shuttle, its much-reduced size supports an attenuated LiPS shuttle mechanism on the EN-CMK3 surface. Furthermore, between 2.5 and 2.6 V, a significantly higher baseline current density is found for CMK3 with LiTFSI (0.48 mA cm^{-2}) compared to both EN-CMK3 with LiTFSI (0.18 mA cm^{-2}; Figure 60, right) and CMK3 with $LiNO_3$ (0.05 mA cm^{-2}; Figure 58, left). This analysis of the oxidation traces provides additional evidence for a reduced LiPS shuttle mechanism on the EN-CMK3 surface. Importantly, the larger baseline current density for EN-CMK3 with LiTFSI relative to CMK3 with $LiNO_3$ is also consistent with the former's reduced, but still significant, LiPS shuttle current from the CC cycling studies (Figure 57c).

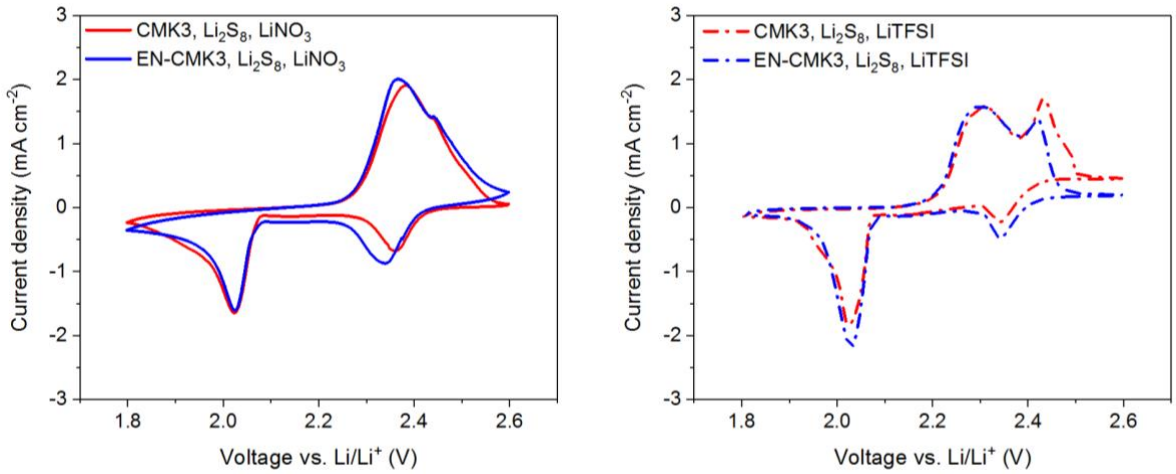

Figure 60. Cyclic voltammograms for CMK3 (red) and EN-CMK3 (blue) with Li_2S_8 using either electrolyte 3 (with $LiNO_3$, solid traces, left) or electrolyte 4 (with LiTFSI, dotted traces, right). All CVs are the same as those in Figure 58, but rearranged to directly compare CMK3 with EN-CMK3.

Overall, the CV study has two major findings about the electrochemistry in Li-S batteries. First, nitrate anions definitely impact the mechanism of charging, which reflect changes in the charging waveforms in the CC study. Second, in the absence of $LiNO_3$, the EN surface groups attenuate the LiPS shuttle as evidenced by its lower current density of the oxidation peak at 2.5 V and lower baseline current density between 2.5 and 2.6 V.

7.3 Amide- and amine-surface groups for increased binding energies and improved battery capacities (Paper 3)

The Li-S battery and CV results from Paper 1 (Section 7.2) show that the functionalized surfaces synthesized using bromomethylation can have a meaningful impact on the battery performance. The two types of catholyte used showed unique features of the EN surface groups: with $LiNO_3$ in the electrolyte, the EN groups help to deliver higher discharging capacities; without $LiNO_3$, the EN groups help to reduce the LiPS shuttle and attain reasonable charging times. The next two studies use only one type electrolyte (with or without $LiNO_3$) to help focus the message of each paper. Paper 3 used $LiNO_3$ in its electrolyte and focuses on improving S utilization. Paper 4 did *not* use $LiNO_3$ in its electrolyte and focuses on how the surface groups impact the LiPS shuttle. To further differentiate these studies, differently-terminated surfaces were explored for their potential to improve the battery performance; amides were used in Paper 3 (this Section) while lithium sulfonates were used in Paper 4 (Section 7.4). In both studies, EN-CMK3 was used as a reference to the amine-functionalized surface from Paper 1* while unmodified CMK3 was used as the control for all samples. (*Even though different EN-CMK3 batches were used between Paper 2 and Papers 3 and 4, no major differences are expected between them given their similar properties).

7.3.1 New sulfur impregnation method: LiPS solution deposition

To replace the catholyte system used in Paper 2, a different S impregnation method must be used. One alternative is LiPS solution deposition on the cathode surface with subsequent heating to remove the solvent (Section 4.1.5). For this reason, a 1 M LiPS (Li_2S_8) solution in DME was created. Although requiring higher temperatures compared to a catholyte, the temperature needed for DME evaporation (60 – 80 °C) is still substantially lower than for S_8 melt diffusion (155 °C); minimal harm to the surface groups should occur. Moreover, the catholyte system allows for the LiPS to come into direct contact with the Li anode from the moment the cell is made. Not only does the LiPS deposition avoid this unwanted contact, but also it should allow any bonding interactions between the LiPS and surface to pre-form before electrolyte addition, thereby potentially enhancing the impact of the surface groups on battery cycling. Lastly, using LiPS deposition permits LiPS-free electrolytes to be used in conjunction with the functionalized CMK3 cathodes.

7.3.2 Selection of new amide-terminated surfaces: DMA-CMK3 and TMMA-CMK3

The syntheses of the amide terminated surface were discussed in Section 6.10. The reasons behind their selection for use in Li-S batteries are discussed here. In the interest of increasing the affinity of LiPS for the CMK3 surface, a new, more powerful surface group to replace EN was needed: previous work has shown that carbonyl groups have the strongest binding energy to LiPS.[128] While ester carbonyls were determined to have the highest binding energies, the lack of a new element makes the characterization and quantification of surface ester groups difficult (*i.e.* bad "organic" chemistry). Instead, amide groups, with a N atom, allow for relatively easy quantification *via* EA and qualification with XPS due to its 1 eV shift in binding energy relative to amines (Figure 48b). A monoamide group (N,N-dimethylacetamide, DMA) and diamide group (N,N,N',N'-tetramethylmalonamide, TMMA) were selected to see if having two carbonyl groups in close proximity can further increase the binding interaction of the surface groups to the LiPS.

7.3.3 Calculation of binding energies between LiPS and surface groups

Density functional theory (DFT) calculations were employed to assess the strength of the interactions between the surface groups and various S species. The interaction is modelled as the binding energy between one of Li_2S, Li_2S_2, Li_2S_4, Li_2S_6, Li_2S_8, or S_8 and a graphitic sheet, with or without a functional group. Only even-numbered S species were considered to limit the large number of combinations and to avoid calculations with radical species. The unfunctionalized carbon surface was simulated using a $C_{54}H_{20}$ model containing of 18 aromatic rings. The functional group was attached to the central carbon, causing its hybridization to change from sp^2 to sp^3. To avoid radical species and to maintain a neutral charge, a proton was added to the neighboring carbon (Figure 61). The interaction was calculated using the M06-2X functional with Grimme dispersion corrections (D3), as implemented in Gaussian16 B.01[47], which has been shown to be appropriate for studies of graphene and carbon nanotubes.[129] DFT calculations were ran in Gaussian16 B.01.[47] Further details relating to the DFT calculations can be found in the experimental section of Paper 3. The binding energies are shown in Table 21. Please note that the BEs in this thesis are updated relative to the version of Paper 3 available at the time. The BEs in Paper 3 do not include dispersion corrections.

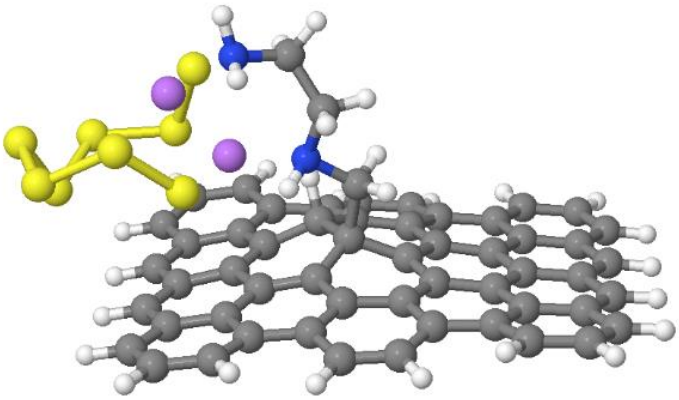

Figure 61. Optimized structure between EN-CMK3 and Li_2S_8. A proton has been added to the graphitic sheet to maintain spin and charge balance.

Table 21. Binding energy values of S species to the model carbon surfaces. Values are reported in eV.

Sample	S_8	Li_2S_8	Li_2S_6	Li_2S_4	Li_2S_2	Li_2S	Average
CMK3	1.23	1.25	1.14	0.80	0.87	0.88	0.99
EN-CMK3	1.17	1.81	1.85	1.60	1.72	1.96	1.79
DMA-CMK3	1.36	2.33	2.03	1.79	1.94	2.03	2.02
TMMA-CMK3	1.18	1.92	1.90	1.70	1.79	1.97	1.86

Based on the hydrophobic nature of S_8, one would intuitively expect it to have the highest affinity for the unfunctionalized, hydrophobic carbon surface. However, the slightly higher binding energy calculated between S_8 and DMA-CMK3 shows that other effects (*e.g.* polarizability) could have an impact on the calculated binding energies. Along similar lines of thinking, by reducing S_8 to Li_2S_8, one might expect the latter to show lower binding energies to the unmodified surface due to its increased polarity, but instead a slightly higher binding energy was calculated. Thus, at least in some cases, simple hydrophilic-hydrophobic arguments do not always seem to be the defining factor. Further reduction of Li_2S_8 deceases its binding energy to the unmodified CMK3 surface relative to S_8 as would be expected from a hydrophilic-hydrophobic point of view. Overall, these comparisons show the complexity of potential interactions between the surface and the S species and trends among binding energies cannot always be predicted *a priori*.

Without a doubt, the most obvious different results from the interaction of reduced S (Li_2S, Li_2S_2, Li_2S_4, Li_2S_6, Li_2S_8) and a functionalized carbon surface. The addition of any functional group increases the binding energy dramatically, sometimes by a factor of 2 or more, compared to the bare CMK3 surface. The greatly enhanced binding energies indicate that the functionalized carbon surfaces will have a potential advantage at keeping the polar S species in close proximity to the cathode, which should facilitate electron transfer and electrochemical conversion of S at this interface. Among the three functionalized surfaces, DMA-CMK3 was found to have the highest average binding energy (2.02 eV), followed by TMMA-CMK3 (1.86 eV), which had a slight edge over EN-CMK3 (1.79 eV). This trend is consistent with the previous report that found the highest binding energies for carbonyl groups,[128] since TMMA and DMA contain carbonyl groups whereas and EN has zero. The noticeably higher BE for DMA-CMK3 over TMMA-CMK3 suggests that monoamides may bind reduced S species better than diamide, despite the latter have twice as many carbonyls. One plausible explanation for this difference is the bulkiness and inflexibility of surface-bound TMMA, which could limit its potential binding modes to LiPS, thereby reducing its BE relative to the smaller, more flexible DMA groups.

7.3.4 Li-S battery performance of amide-modified carbons

These carbons were then tested in Li-S batteries to confirm that the higher BEs do indeed have a positive impact on the battery cycling. The electrolyte used was 1 M LiTFSI with 0.4 M $LiNO_3$ in 1:1 DOL-DME (Electrolyte 2, Table 4). The battery results are summarized in Figure 62.

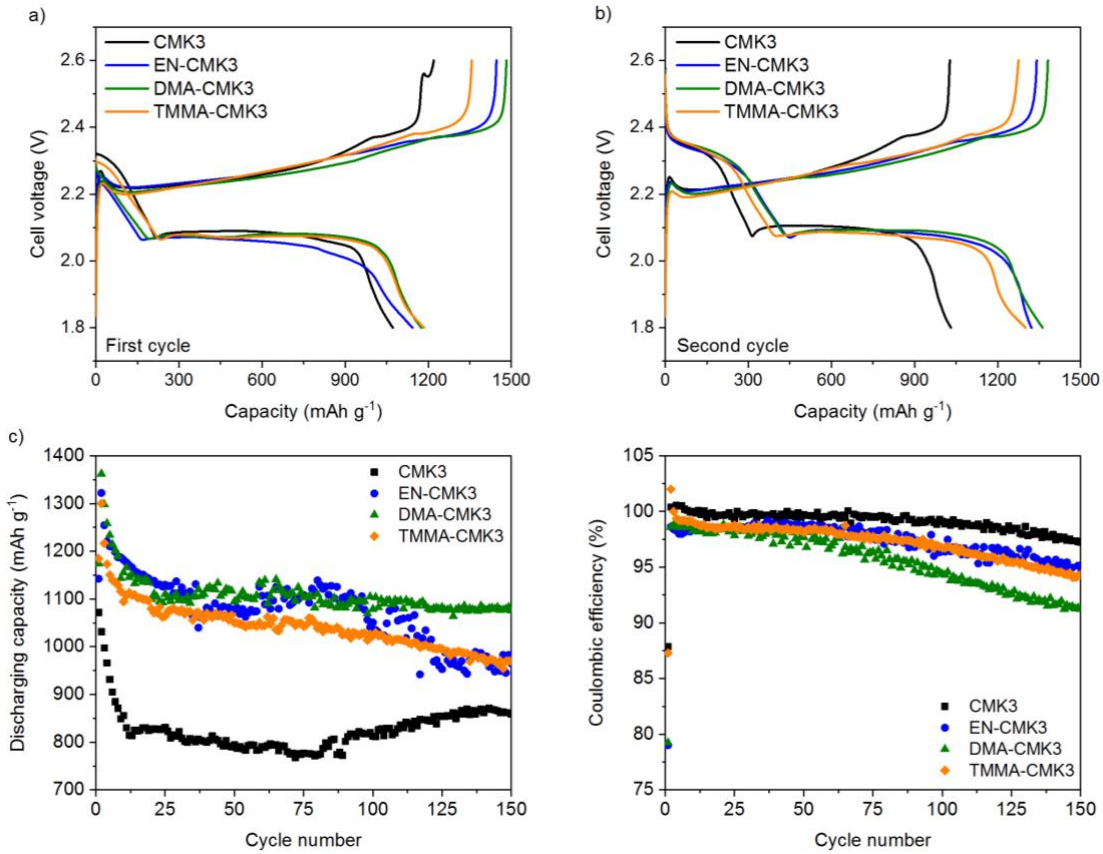

*Figure 62. Constant current cycling performance of Li-S cells using amide- and amine-modified CMK3 cathodes cycled at 0.1 C (167.5 mA g^{-1}). **a)** Voltage profiles for the 1st cycle and **b)** 2nd cycle. **c)** Specific discharging capacities and **d)** Coulombic efficiencies versus cycle number.*

As was the case with the catholytes from Paper 2 (Section 7.2), all cells in this study experience the same change in their discharge profile between the first and second cycle: the high voltage plateau at 2.4 V again becomes distinct during the second cycle (Figure 62a and b). What this shows is that the S starting material is the same from the electrochemical perspective; whether the Li_2S_8 is homogeneously dissolved in the catholyte (Paper 2) or deposited on the surface (Paper 3) does not appear to affect the first discharge. In both cases, S_8 results at the end of the first cycle, which allows for additional reduction of S and therefore higher capacities in latter cycles. Also similar to the previous study, the extra oxidation in the first cycle to create S_8 results in a relatively low ICE of *ca.* 87% for CMK3 and TMMA-CMK3 and *ca.* 78% for EN-CMK3 and DMA-CMK3 (Figure 62d).

Importantly, the cells with functionalized cathodes exhibit significantly higher discharging capacities. This is due to another change in their 2nd cycle waveforms: while the appearance of the 2.4 V plateau occurs for all CMK3 cathodes, the second discharge plateau at 2.1 V becomes proportionally shorter in the case of unmodified CMK3. Given that the 2.1 V plateau comes as a result of LiPS (Li_2S_n, $3 \leq n \leq 8$) conversion to Li_2S_2 and Li_2S,[39, 59] its decreased length suggests a relatively inefficient electrochemical process on the pristine surface. The 2.4 V plateau is also proportionally shorter for CMK3, which further supports weaker interactions with S species at this electrode-electrolyte interface. These observations are consistent with the much higher BEs calculated for the functionalized CMK3 samples compared to their unmodified precursor (Table 21).

Increased cycling reveals the CMK3 reaching a stable capacity around 800 mAh g^{-1} near cycle 15 while the functionalized cathodes show much higher capacities around 1100 mAh g^{-1} (Figure 62c). Overall, the three functionalized cathodes show similar performance over 100 cycles, but afterwards, DMA-CMK3 shows the highest, most stable capacity. This is in line with its higher average BE compared to the other two surfaces.

Surprisingly, the unmodified CMK3 cathode shows a slight increase in capacity after the first 100 cycles, but its capacity is still lower than the modified cathodes. The reasons for this increase are unknown.

In the CEs, all cells increase to >97% after the first cycle with the CMK3 cell slightly outperforming the rest. Around cycle 50, all three functionalized cathodes start to show their CEs decaying faster than the control cell. Some plausible explanations for this faster decease include: one, the higher capacities of the modified cathodes require that more S is reduced and oxidized in each cycle making it harder to achieve and maintain higher CEs; two, residual Br species from bromomethylation (Table 16) could dissolve into the electrolyte, which could potentially impact the S electrochemistry and/or cause corrosion; and three, the surface groups could slowly degrade overtime and/or become covered with deposited electrolyte species (*e.g.* reduction of nitrate; Figure 52, right), either of which would render the surface groups less effective at binding LiPS.

In summary, attaching any one of these functional groups to the carbon surface greatly benefits the cell cycling, which is observed primarily in the form of higher S utilization (*ca.* 30% increase over the unmodified control). Unfortunately, with the exception of the higher capacity for DMA-CMK3 after cycle 100, the surface groups new to this study, DMA and TMMA, do not appear to further enhance any cell parameter significantly more than the previously used EN surface group. Part of this discrepancy could be due to the relative surface group loadings: EN had a much higher loading (0.91 mmol g^{-1}) than either DMA (0.71 mmol g^{-1}) or TMMA (0.37 mmol g^{-1}). In other words, if the surface group loading of either amide could be increased to the level of EN or greater, the battery performance would be measurably improved. The high BEs calculated for amide groups, in particular monoamides like DMA, provide reasons for their continued use as modifying groups on surfaces (carbon or otherwise) where strong interactions are desired with the LiPS and other polar S species.

7.4 Lithium sulfonate groups for a greatly reduced LiPS shuttle (Paper 4)

While Paper 3 focused on $LiNO_3$-containing electrolytes and improving the S utilization, the final study, Paper 4, focused on $LiNO_3$-free electrolytes and studying the LiPS shuttle. The LiPS shuttle, which is discussed in detail in background (section 4.1.4) and studied in Paper 2 (Section 7.2), is an electrochemical phenomenon common in Li-S batteries that comes as a result of the high solubility of LiPS. The undesired diffusion of LiPS away from the carbon surface and subsequently reducing at the Li anode counteracts the applied current; basically, the cell self-discharges when one tries to charge it. $LiNO_3$ is a common electrolyte additive for Li-S batteries to attenuate the lithium polysulfide (LiPS) shuttle[74-75, 82, 130] and increase the CEs to > 95% (Figure A67). Thus, by excluding it, the direct effects of the surface groups on the LiPS shuttle can be observed by measuring the CEs.

For this study, a surface group was chosen specifically so as to resemble the chemical characteristics of the nitrate anion as closely as possible. This selection was lithium sulfonate group ($LiSO_3$-CMK3) whose synthesis was discussed previously in Section 6.10. The reasons for its selection for use in Paper 4 are discussed here.

In the pursuit of a surface-bound "nitrate mimic", several groups were considered. Unfortunately, the construction of surface-bound nitrate groups creates an organic nitrate (R-ONO_2), which is a neutral species and would likely show much different properties compared to its anionic, solution-phase cousin (NO_3^-). Moreover, the conditions to install nitrate groups would also likely involve nitric acid (HNO_3), which is potent carbon oxidizer (Section 2.3).[37, 131] The synthesis of organic nitrates would likely result in a large increase of O-containing functionality (*e.g.* alcohols, carboxylic acids) in addition to the desired nitrate groups.[27-30, 132] In summary, surface-bound nitrate groups are probably not the best choice for a "nitrate mimic."

Looking for a replacement, organic sulfonates (R-SO_3^-) appear to fit the bill; like nitrate anions, they are monoanionic, contain three Os, and are halogen-free. Their basicities are also comparable since their conjugate acids, methanesulfonic acid (CH_3SO_3H) and HNO_3, have pKa values of -1.9 and -1.4, respectively.[119]

Overall, $LiSO_3$ groups should work well as surface-bound nitrate mimics. EN-CMK3 was also used to test for its potential in reducing the LiPS shuttle. The S impregnation method, LiPS deposition, was the same as used in Paper 3 (Section 7.3). The electrolyte was also the same, except for the purposeful omission of 0.4 M $LiNO_3$; the electrolyte was 1 M LiTFSI in 1:1 DOL-DME (Electrolyte 1, Table 4).

7.4.1 Measuring the LiPS: the initial Coulombic efficiency (ICE)

The first test performed was 0.1C cycling with a maximum charging time set to 1000 hrs, or 100 times the theoretical maximum. As stated in Paper 2 (Section 7.2), one of the main tests for the LiPS shuttle is the ICE or the ratio of the first discharge over the first charge.[75] A strong LiPS is characterized by an exceptionally long charging plateau at *ca.* 2.35 V during the first cycle, which results in a very low ICE (< 10%). To help account for random fluctuations in cell fabrication and testing and to obtain an average ICE, multiple cells for each cathode were made. The first cycles for all cells are summarized in Figure 63.

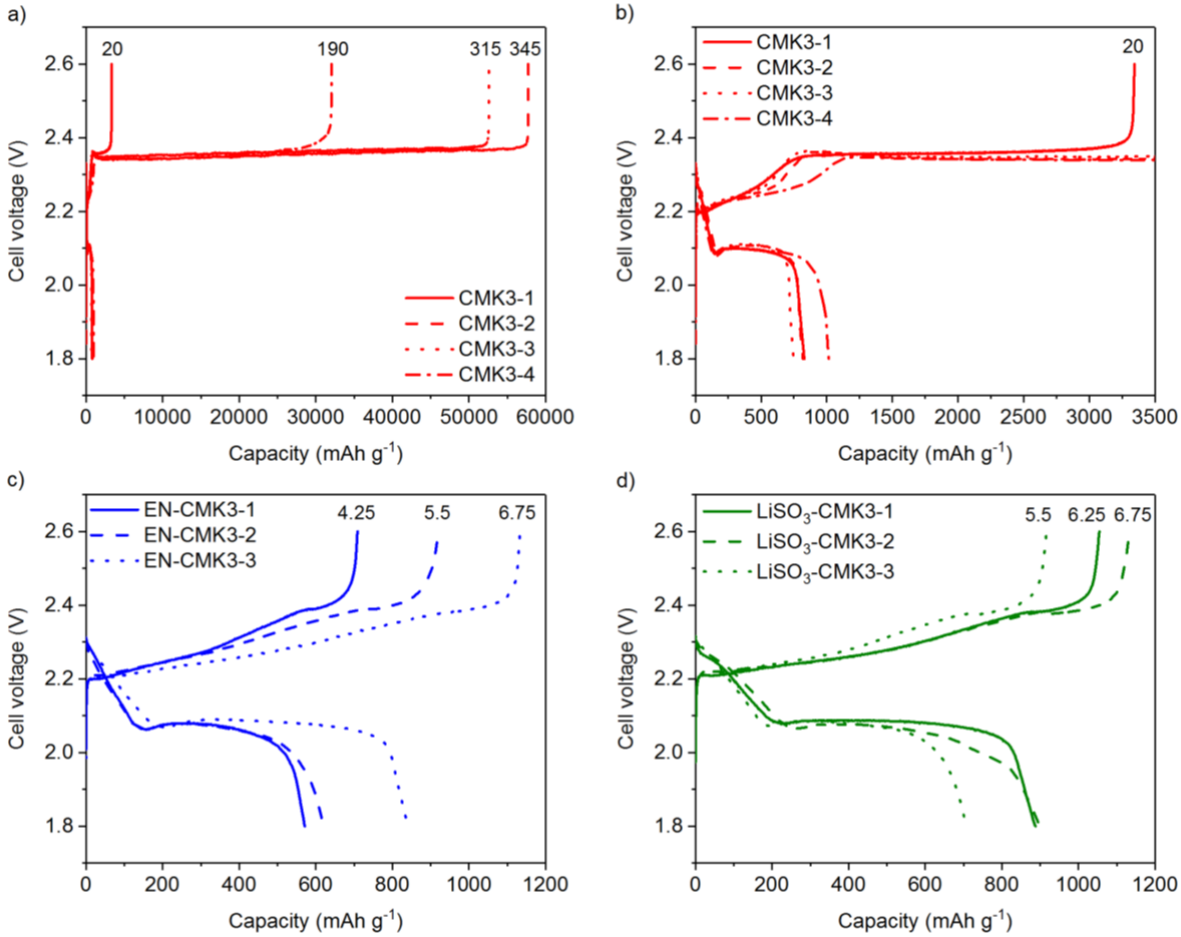

Figure 63. ***a)*** *and* ***b)*** *First cycles for unfunctionalized CMK3 cathodes at 0.1C. The left graph contains an extended version of the right in order to display the ultralong charging times required. First cycles for* ***c)*** *EN-CMK3 cathodes and* ***d)*** *$LiSO_3$-CMK3 cathodes at 0.1C. The number above each trace corresponds to the charging time in hours. The first cells for each cathode, CMK3-1, EN-CMK3-1, and $LiSO_3$-CMK3-1 (solid traces), were subjected to long-term cycling (Figure 64) while EN-CMK3-2 and $LiSO_3$-CMK3-2 (dashed traces) were subjected to rate testing (Figure 65).*

Four replicate cells with unfunctionalized CMK3 cathodes show exceptionally long charge times of 340, 315, 190, and 20 hours with corresponding ICEs of 1.4%, 1.4%, 3.2, and 25%, respectively (average: 7.8%, Figure 63a and b). From these long charging times and low ICEs, it is clear that the LiPS shuttle is unambiguously present in these cells when $LiNO_3$ is not used in the electrolyte. At the same time, the large variation in charging times among these cells shows that the strength of the LiPS shuttle is relatively random. In stark contrast, triplicate cells made with EN-CMK3 cathodes exhibit charging times of 4.25, 5.5, and 6.75 hrs with

ICEs of 81%, 68%, and 74%, respectively (average: 74.3, Figure 63c), while triplicate cells made with $LiSO_3$-CMK3 charge in 6.25, 6.75, and 5.5 hrs with ICEs of 84%, 79%, and 77%, respectively (average: 80%, Figure 63d).

For comparison, these average ICEs were compared to ICEs reported in other studies, which also used cathode modifications in place of electrolytic $LiNO_3$ (Table 22). What is clear is that the ICE without cathode modification in this study is much lower than same value from other reports. This noticeably lower ICE shows that, under the conditions used in this study, unmodified CMK3 is inherently inept at retaining LiPS within its pores and attenuating the LiPS shuttle. Even though the average ICEs of both EN-CMK3 and $LiSO_3$-CMK3 are still below other cathode modifications, their *relative* increases in ICE are among the highest reported. This drastic increase supports strong interactions between the LiPS and both the EN and $LiSO_3$ surface groups, which reduce the LiPS shuttle.

Table 22. Comparison of improvements in initial Coulombic efficiency (ICE) without electrolytic $LiNO_3$ using cathode modifications.

Cathode modification	ICE without cathode modification (%)	ICE with cathode modification (%)	Increase (%)
Nitrogen-enriched mesoporous carbon, ref[10]	85%	95%	10%
Phosphorous quantum dots, ref[133]	80%	90%	10%
Magnéli-phase Ti_nO_{2n-1}, ref[134]	80%*	95%*	15%
RuO_2 in graphite, ref[75]	66.4%	92.5%	26.1%
EN-CMK3 with Li_2S_8 catholyte, ref[81]	3%	73%	70%
This work	7.8%#	EN-CMK3: 74.3%§	66.5%
		$LiSO_3$-CMK3: 80%§	72.2%

* -Unmodified sample contained rutile TiO_2 while the best performing modified sampled contained Magnéli-phase Ti_4O_7.
# -Average of four ICEs
§ -Average of three ICEs

7.4.2 Long-term battery cycling

For each cathode, one cell was selected for prolonged cycling (100 cycles) at 0.1C to see the long-term effect of the surface groups on battery performance. In selecting the control cell, CMK3-1 was the obvious choice given its much shorter charging cycle than the other three. For the functionalized cathodes, EN-CMK3-1 and $LiSO_3$-CMK3-1 were chosen for 0.1C cycling while EN-CMK3-2 and $LiSO_3$-CMK3-2 was subjected to rate testing (Section 7.4.3) given the similar discharge capacities and CEs between the first and second cell of each cathode.

As was the case in both previous studies, the second cycle discharging waveforms show the prominence of the plateau at 2.4 V becoming clear (Figure A68Figure A70). This change happens for both functionalized cathodes and the CMK3 control. Given this similarity among all three battery studies regardless of cathode and electrolyte used, it appears that S_8 is the final charge product in all cases. This observation is important since the presence or lack of $LiNO_3$ does not appear to change the S_8 charge product. Thus, the main role of $LiNO_3$ is likely to catalyze the transformation of Li_2S to S_8, not change the final S charge product.

The long-term capacities are shown in Figure 64, left. As before, the second cycle for all cells shows a noticeable increase in the discharging capacity due to starting from S_8, which allows for extra S reduction in latter cycles. After the second cycle, all cells show a slow capacity fade, but only the functionalized cathodes reach stabilized capacities. For EN-CMK3 and $LiSO_3$-CMK3, stable capacities of 670 and 820 mAh

g^{-1}, respectively, are realized at about the 20th cycle. In contrast, the CMK3 cell loses on average *ca.* 2 mAh g^{-1} of discharging capacity per cycle after the 20th cycle, which prevents this cathode from reaching a stabilized capacity, eventually falling below EN-CMK3. Together with the greatly increased ICEs, the enhanced capacity retention shown by the functionalized cathodes provides evidence for beneficial interactions between the surface groups and the LiPS. Between the two functionalized cathodes, $LiSO_3$-CMK3 exhibits a *ca.* 160 mAh g^{-1} advantage over EN-CMK3. Given the much higher surface group loading for EN-CMK3 compared to $LiSO_3$-CMK3 (0.92 *vs.* 0.32 mmol g^{-1}, Table 16), the higher capacity obtained in the latter evidences proportionally stronger interactions between the $LiSO_3$ groups at the LiPS. Strong ionic interactions possible with $LiSO_3$ but not EN could be part of increased capacity. Likewise, the sulfonate groups could facilitate Li^+ hopping, thereby increasing Li^+ ion conduction near the cathode surface.

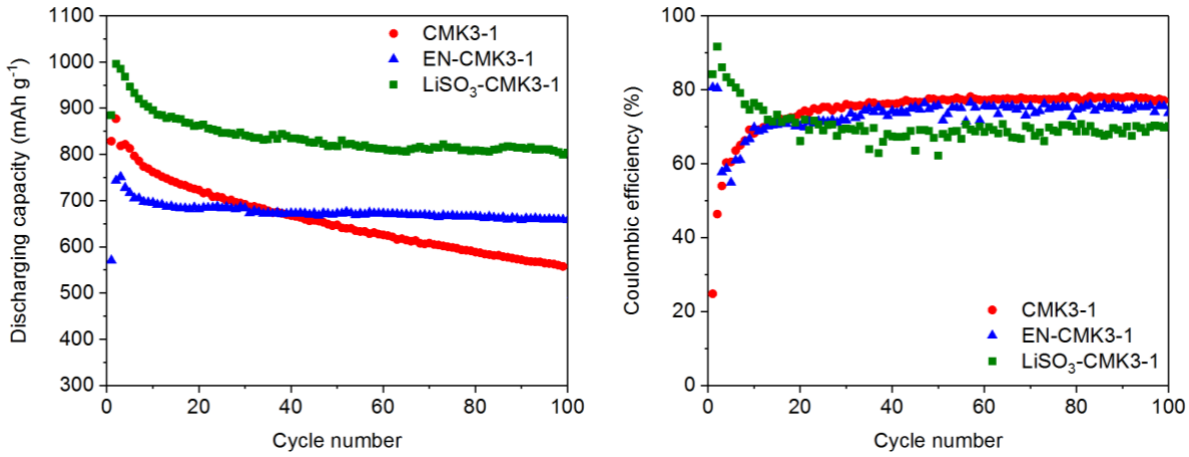

Figure 64. Discharging capacities (left) and coulombic efficiencies (right) at 0.1C for CMK3 cathodes.

In the CEs (Figure 64, right), the EN-CMK3 cell experiences a slight decrease during the third cycle to 58%, before gradually increasing to *ca.* 75%. This behavior is similar to the catholyte/LiTFSI cell from Paper 2 (Figure 57c), which showed a decrease in its CE to *ca.* 25% in the second cycle. These similar results suggest that the EN groups, while greatly increasing the ICE, struggle to contain the LiPS shuttle during cycles 2-10. For $LiSO_3$-CMK3, its CE increases during the second cycle to >90% and then slowly decreases to *ca*. 70%, showing that this surface group is much better at suppressing the LiPS shuttle. During this time, the CMK3 cell demonstrates that prolonged, continuous cycling can eventually alleviate a strong LiPS shuttle since its CE gradually increases from 25% to *ca.* 77% over the first 20 cycles. This is the highest stabilized CE among the three cells, but this value for CMK3 could be artificially high due to its much faster capacity fading. Between the two functionalized cathodes, the higher CE for EN-CMK3 (75%) relative to $LiSO_3$-CMK3 (68%) could be due to the former's lower capacity and/or significantly higher surface group loading.

7.4.3 Rate testing of functionalized cathodes

To study how the LiPS is affected by the applied current, one cell of each functionalized cathode was subjected to rate testing. The CMK3 control was not rate tested due to its considerably longer charging times. The cells were cycled at 0.1C, 0.2C, 0.5, 1C for ten cycles each then 10 more at 0.1C. The ICEs at 0.1C for EN-CMK3 and $LiSO_3$-CMK3 are 75 and 78%, respectively, similar to the ones found previously (80% and 85%) and are incorporated into Table 22. During the first 10 cycles at 0.1C, both cathodes behave very similarly to the previous cells cycled 100 times at 0.1C in terms of their discharging capacities and CEs (Figure 65, left). As before, EN-CMK3 shows a sharp decrease in its CE during the second cycle, this time to 18% while $LiSO_3$-CMK3 experiences a brief increase in its CE before stabilizing to *ca.* 70%. Both cells show a slow capacity fade after an initial increase in capacity.

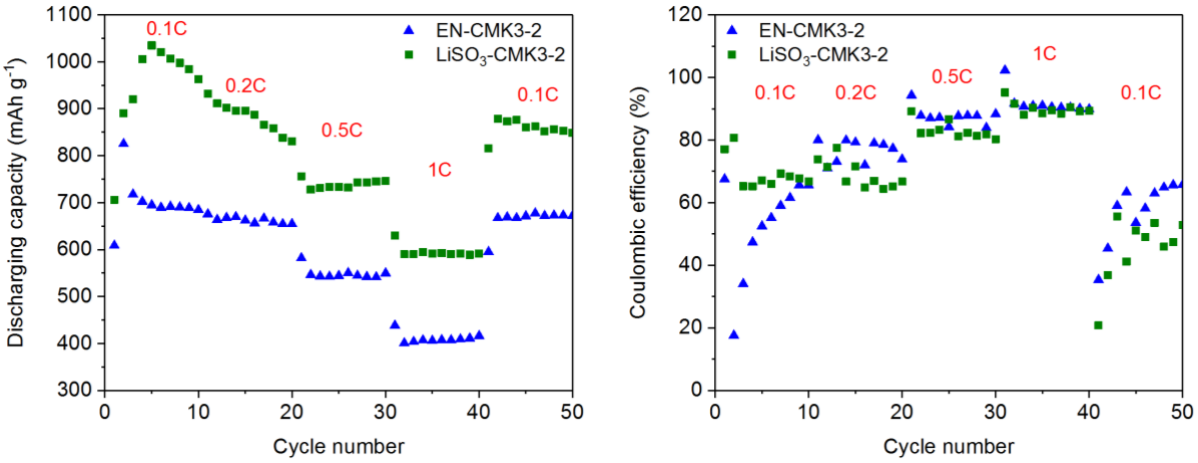

Figure 65. Discharging capacities (left) and Coulombic efficiencies (right) at several C-rates for EN-CMK3 and $LiSO_3$-CMK3 cathodes.

During cycles 11-20, doubling the applied current to 0.2C appears to not greatly impact the rate of capacity fading established during the first ten cycles in either cell. The CEs are increased slightly during this time, but more for EN-CMK3 than LiSO3-CMK3. Upon further increase of current to 0.5C, a moderate decrease in capacity (100-150 mAh g^{-1}) is observed, but the capacity fading is stalled completely. In fact, a slight capacity increase is observed in $LiSO_3$-CMK3 during these 10 cycles. The CEs are also improved to about 87% and 82% for EN-CMK3 and $LiSO_3$-CMK3, respectively. When the current maximum of 1C is reached during cycles 30-40, a similar decrease in capacity is recorded along with a slight increase in CE to *ca.* 90% for both cathodes. Upon returning to 0.1C, most of the capacity is regained and a slight capacity fading is found for $LiSO_3$-CMK3. Most importantly, however, the cells experience a significant decrease in CE to 35% and 21% for EN-CMK3 and $LiSO_3$-CMK3, respectively. In subsequent cycles, the CEs improve gradually but the cells struggle to regain their previously attained CE values at 0.1C at cycle 10.

To summarize the Li-S battery results in this study, the surface groups of $LiSO_3$ appear to be a better "nitrate mimic," as was anticipated. Although both groups greatly increase the ICE relative to unmodified CMK3, $LiSO_3$-CMK3 does not seem prone to temporary lapses in retaining the LiPS shuttle; the EN-CMK3 has shown three times that it suffers from lower CEs during cycles 2-10 while two cells for LiSO3-CMK3 maintain high CEs (> 65%) during these cycles. Additionally, the higher capacities obtained with $LiSO_3$-CMK3 is meriting. By increasing the applied current, the discharging capacities decrease but the CEs increase. This observation suggests that, for Li-S batteries where the LiPS shuttle is a major issue, its severity can be diminished simply by increasing the applied currents. However, the return to lower currents indicates that increased cycling rates might not be the best option since the CEs suffer noticeably during the first cycle at 0.1C.

7.4.4 Self-discharge with concurrent electrochemical impedance spectroscopy (EIS)

In testing for the LiPS shuttle, a few possible tests can be performed. One of the main tests is the aforementioned ICE, but the LiPS shuttle can manifest itself in other ways as well. One of these is self-discharge where, as one might expect, a strong LiPS has been correlated with fast rate of voltage losses[66] and, importantly, $LiNO_3$ is known to suppress self-discharge.[135-136] In the present study, one uncycled cell of each cathode was subjected to self-discharge for 70 hrs with electrochemical impedance spectra (EIS, Section 3.4.3) taken every hour. All cells started with open-circuit voltages (OCVs) of approximately 2.34 V (Figure 66, left). After 70 hrs, the OCV of the CMK3 cell decreases by 165 mV, the bulk of which happens after 30 hrs. In contrast, the two functionalized cathodes fare much better as $LiSO_3$-CMK3 loses only 6 mV while EN-CMK3 *gains* 11 mV. Thus, the surface groups act as effective "nitrate mimics" in that they help to suppress self-discharge.

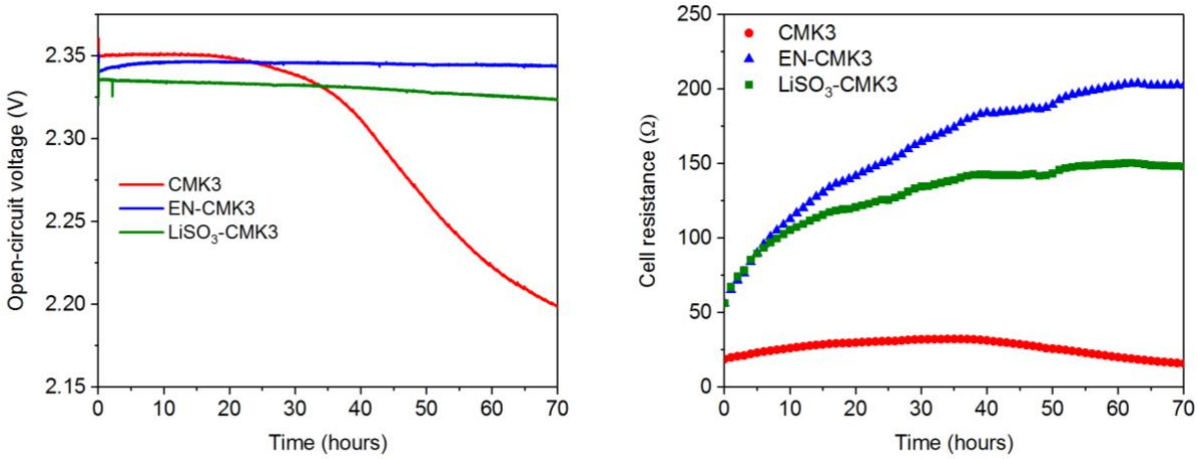

Figure 66. Open-circuit voltages (OCVs, left) and cell resistances (right) during self-discharge test for all CMK3 cathodes.

The concurrent EIS was used to measure the cell resistance (see Paper 4 for details). During the entire 70 hr test, the cell resistance was measured to be very low for CMK3 at between 20-30 Ω (Figure 66, right). The same parameter for each of the functionalized cells started much higher at around 60 Ohms before increasing greatly to about 150 and 200 for $LiSO_3$-CMK3 and EN-CMK3, respectively. Overall, the higher cell resistances correlate with lower rates of voltage loss. Since this test was run in self-discharge as opposed to normal cycling, a higher cell resistance is a *beneficial* feature. That is, the higher cell resistances can be interpreted as the cathodes' ability to oppose LiPS diffusion away from its surface, which minimizes self-discharge. As further evidence for this correlation, the period of time during which the CMK3 lost the most voltage (30-60 hrs) is also the time when a slight decrease in cell resistance was recorded. Additionally, between the two modified cathodes, the lower voltage loss (or higher gain) of EN-CMK3 correlates with its higher final cell resistance.

Overall, the correlation between cell resistance and voltage retention suggests that the former is a direct measurement of the interaction strength between the electroactive LiPS and the cathode surface; the surface groups of EN-CMK3 and $LiSO_3$-CMK3 provide superior binding points for LiPS, which, in turn, minimize self-discharge.

7.5 Conclusions from the Li-S battery studies

The major takeaway from all three studies is that the surface groups installed on the surface *via* bromomethylation have a definite, positive impact on the Li-S cell. A total of four surface groups were tested (EN, DMA, TMMA, and $LiSO_3$) and all of them imparted a measurable benefit to the battery, regardless of which electrolyte was used. Of these four used, DMA and $LiSO_3$ would appear to be the best candidates for future tests in Li-S batteries. For DMA, it is due to its higher binding energy and superior capacity retention. For $LiSO_3$, it is due to its higher capacities and higher CEs. When taking into consideration that $LiSO_3$-CMK3 had the lowest surface group loading of the 4 (0.32 mmol g^{-1}), the impact of this surface group on cell cycling is even more impressive. If the surface sulfonate loading could be increased to the level of EN-CMK3 (0.91 mmol g^{-1}) or greater, such a modified carbon would likely perform extremely well as a cathode in Li-S batteries. Specifically, when paired with a $LiNO_3$-free electrolyte, the CEs of a highly sulfonated carbon would hopefully reach those achieved with electrolytic $LiNO_3$ (>95%).

8 Conclusions

Carbon, one of the elements known longest to humans, has provided a constant energy source in the form of charcoal for millennia. The ever-increasing role of carbon emissions (CO_2, CO, CH_4) in affecting the planet's climate will mean reducing the use of carbon-based fuels, especially charcoal. However, these same carbons may provide the necessary combination of material properties to make alternative energy sources viable. One of the most important properties of charcoal-based materials is the ease with which they can be shaped and modified to fit the needs of a given application.

The two ways of modifying carbon materials presented in this thesis are a bottom-up method of doping Fe-OMCs with soluble Fe salts and a two-step surface modification method of bromomethylation and nucleophilic substitution. One of the main conclusions from the first study is that soluble salts can indeed increase the Fe concentration in the carbon precursor solution, but this increased concentration does not necessary lead to higher Fe loadings in the final Fe-OMC. For one Fe-OMC made using a soluble salt, a much higher Fe loading was obtained, but the other two exhibited similar or lower loadings compared to the control Fe salt. The other important conclusion is that the extra Fe in the one Fe-OMC does not appear to greatly increase its catalytic efficiency in the ORR. Using EPR, it was found that the Fe salt definitely influences the type of Fe formed within the carbonaceous structure. Future studies with soluble Fe salts should focus on tuning one synthesis parameter (*e.g.* carbonization temperature, type of carbon precursor) in an effort to transform more of the soluble Fe salt into ORR active sites.

The second major method of creating new carbon materials is surface modification. In this thesis, a new, two-step method for the surface modification of carbon materials consisting of bromomethylation and nucleophilic substitution is presented and discussed. This two-step method boasts many advantages over other techniques such as oxidation and diazonium coupling including high reproducibility, synthetic simplicity and flexibility, and mild reaction conditions using commercially available reagents. A total of 12 surface groups were synthesized across three studies including amines, amides, azide, ferrocene, and lithium sulfonate. A good sense of "organic" chemistry allows for efficient qualification and quantification of these surface groups; all surface groups introduce at least one new element to the carbon structure. Four of these surface groups were tested in Li-S batteries and all four showed greatly enhanced battery performance relative to the unfunctionalized control. The enhanced battery performance was realized in the form of higher discharging capacities if $LiNO_3$ was used in the battery electrolyte. If $LiNO_3$ was omitted from the electrolyte, the surface groups greatly increase the ICEs, which is indicative of a much-reduced LiPS shuttle caused by strong interactions between the modified carbon surface and the LiPS dissolved in the electrolyte. Overall, given the lack of viable methods for surface functionalization of carbons, the two-step method should find utility in future studies; Li-S batteries are only one potential application of modified carbon surfaces.

9 Appendix

Table A23. Trials for bromomethylation of AC

Trial	Br loading (mmol g^{-1})§	Mass increase (%)
1	1.35	53.8
2	1.24	54.6
3[a, f]	1.10	32.6
4[a, d, f]	1.05	35.5
5	1.25	47.8
6[a]	1.07	51.9
7[a, h]	1.21	41.5
8[b]	1.01	39.1
9	0.84	22.6
10[d]	1.37	48.5
11[g]	1.00	65.8
12[c, e, i]	1.12	45.2
Average $\pm$ standard deviation	1.13 ± 0.16	44.9 ± 11.7

§ -Determined by XRF
a -Selected for azide substitution (Table A24).
b -Selected for iodide substitution (Table 14, Entry 1)
c -Selected for All_2NH substitution (Table 14, Entry 2)
d -Selected for EN substitution (Table 14, Entry 3a and b)
e -Selected for Me_3EN substitution (Table 14, Entry 4)
f -Selected for tren substitution (Table 14, Entry 5a and b)
g -Selected for NH_4OH substitution (Table 14, Entry 6)
h -Studied with XPS (Figure 27)
i -Studied with nitrogen-sorption (Figure 25, Table 13)

Table A24.Trials for azide substitution of bromide on Br-AC

Trial	Initial Br loading in Br-AC (mmol g^{-1})§	N_3 loading in N_3-AC (mmol g^{-1})*	Remaining Br in N_3-AC (mmol g^{-1}) §	Remaining Br in N_3-AC (%)	Yield (%)
1	1.07	1.00	0.05	4.7	93.4
2	1.07	0.96	0.06	5.6	89.7
3[a]	1.07	0.86	0.07	6.5	80.4
4	1.07	0.78	0.07	6.5	72.9
5	1.10	0.81	0.08	7.3	73.6
6	1.05	0.85	0.07	6.7	81.0
7[a, b]	1.21	1.20	0.10	8.3	99.2
Average ± standard deviation	1.09 ± 0.05	0.92 ± 0.15	0.07 ± 0.02	6.5 ± 1.1	84.3 ± 10.0

* -Determined by EA
§ -Determined by XRF
a -Selected for CuAAC reaction with ethynylferrocene (Table A25).
b -Studied with XPS (Figure 35).

Table A25. Trials for CuACC coupling of ethynylferrocene to N_3-AC to form Fc-AC

Trial	Initial Br loading in Br-AC (mmol g^{-1})§	N_3 loading in N_3-AC (mmol g^{-1})*	Triazole loading in Fc-AC (mmol g^{-1})*	Fe loading in Fc-AC§ (mmol g^{-1})§	Yield from N_3-AC (%)	Yield from Br-AC (%)
1	1.07	0.86	0.77	0.78	90.7	72.9
2[a]	1.21	1.20	1.03	1.02	85.0	84.3
Average ± standard deviation	1.14 ± 0.10	1.03 ± 0.24	0.90 ± 0.18	0.90 ± 0.17	88.5 ± 4.0	78.6 ± 8.1

* -Determined by EA
§ -Determined by XRF
a -Studied with XPS (Figure 46)
Note: Trials 1 and 2 had copper loadings of 0.01 and 0.02 mmol g^{-1}, respectively, as determined by XRF.

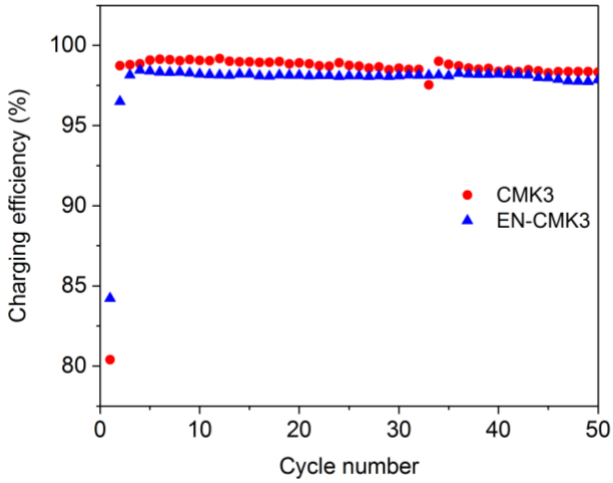

Figure A67. Charging efficiencies at 0.1 C of catholyte/$LiNO_3$ cells with a CMK3 or EN-CMK3 cathode.

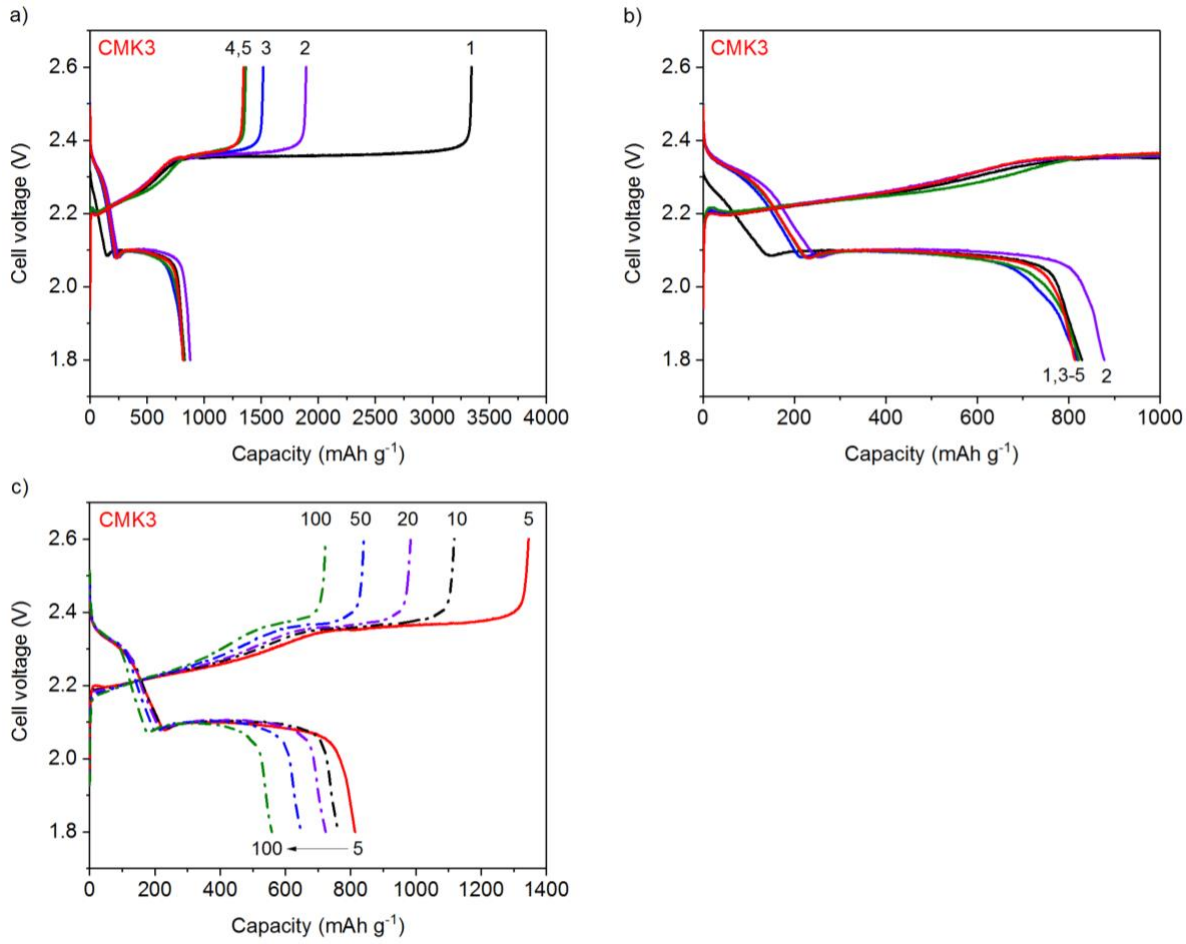

Figure A68. Waveforms for the CMK3 cell cycled at 0.1C. The solid waveforms are colored as follows: 1st black, 2nd violet, 3rd blue, 4th green, 5th red. The dotted waveforms are colored as follows: 10th black, 20th violet, 50th blue, 100th green. The 1st cycle waveform is also shown in Figure 63a and 5b.

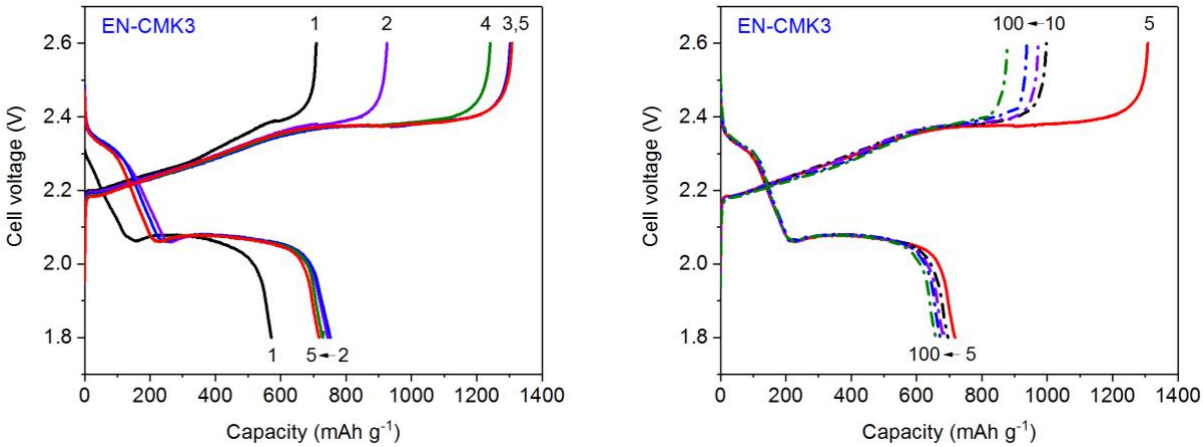

Figure A69. Waveforms for the EN-CMK3 cell cycled at 0.1C. The solid waveforms are colored as follows: 1st black, 2nd violet, 3rd blue, 4th green, 5th red. The dotted waveforms are colored as follows: 10th black, 20th violet, 50th blue, 100th green. The 1st cycle waveform is also shown in Figure 63c.

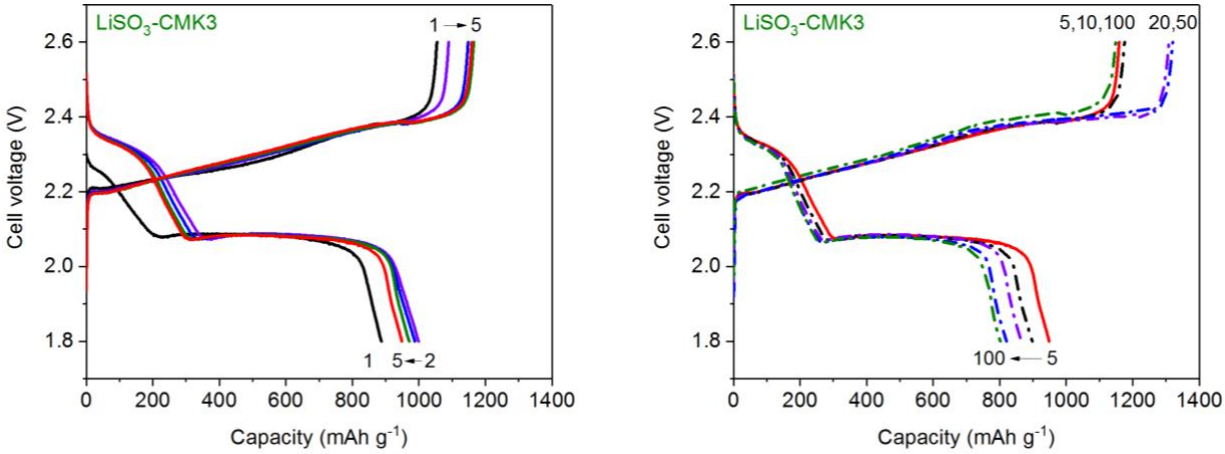

Figure A70. Waveforms for the $LiSO_3$-CMK3 cell cycled at 0.1C. The solid waveforms are colored as follows: 1st black, 2nd violet, 3rd blue, 4th green, 5th red. The dotted waveforms are colored as follows: 10th black, 20th violet, 50th blue, 100th green. The 1st cycle waveform is also shown in Figure 63d.

10 References

1. Carbon. In *Chemistry of the Elements*, Greenwood, N. N.; Earnshaw, A., Eds. Butterworth-Heinemann: Oxford, 1997; pp 268-327.
2. BBC NEWS | Science/Nature | Chinese made first use of diamond. http://news.bbc.co.uk/2/hi/science/nature/4555235.stm.
3. Krogt, P. v. d., 6. Carbonium (Carbon) - Elementymology & Elements Multidict. **2017**.
4. Ströck, M., Eight allotropes of carbon. **2006**.
5. Natural Graphite | Asbury Carbons. https://asbury.com/technical-presentations-papers/materials-in-depth/natural-graphite/.
6. King, H. How Do Diamonds Form? | They Don't Form From Coal! http://geology.com/articles/diamonds-from-coal/.
7. Bundy, F. P., Pressure-Temperature Phase-Diagram of Elemental Carbon. *Physica A* **1989,** *156* (1), 169-178.
8. Kinoshita, K., *Carbon : electrochemical and physicochemical properties*. Wiley: New York, 1988; p xiii, 533 p.
9. Jenkins, G. M.; Kawamura, K., Structure of glassy carbon. *Nature* **1971,** *231* (5299), 175-6.
10. Sun, F.; Wang, J.; Chen, H.; Li, W.; Qiao, W.; Long, D.; Ling, L., High efficiency immobilization of sulfur on nitrogen-enriched mesoporous carbons for Li-S batteries. *ACS Appl Mater Interfaces* **2013,** *5* (12), 5630-8.
11. Kicinski, W.; Szala, M.; Bystrzejewski, M., Sulfur-doped porous carbons: Synthesis and applications. *Carbon* **2014,** *68*, 1-32.
12. Kleitz, F.; Choi, S. H.; Ryoo, R., Cubic Ia3d large mesoporous silica: synthesis and replication to platinum nanowires, carbon nanorods and carbon nanotubes. *Chem Commun (Camb)* **2003,** (17), 2136-7.
13. Li, R.; Ge, Y. J.; He, F.; Dou, L. T.; Liu, B. H.; Li, Z. P., Prevention of active-site destruction during the synthesis of high performance non-Pt cathode catalyst for fuel cells. *Rsc Adv* **2017,** *7* (11), 6622-6630.
14. Pampel, J.; Fellinger, T. P., Opening of Bottleneck Pores for the Improvement of Nitrogen Doped Carbon Electrocatalysts. *Adv Energy Mater* **2016,** *6* (8).
15. Dombrovskis, J. K.; Jeong, H. Y.; Fossum, K.; Terasaki, O.; Palmqvist, A. E. C., Transition Metal Ion-Chelating Ordered Mesoporous Carbons as Noble Metal-Free Fuel Cell Catalysts. *Chem Mater* **2013,** *25* (6), 856-861.
16. Nitze, F.; Fossum, K.; Xiong, S. Z.; Matic, A.; Palmqvist, A. E. C., Sulfur-doped ordered mesoporous carbons: A stability-improving sulfur host for lithium-sulfur battery cathodes. *J Power Sources* **2016,** *317* (Supplement C), 112-119.
17. Ma, Z. F.; Xie, X. Y.; Ma, X. X.; Zhang, D. Y.; Ren, Q. Z.; Hess-Mohr, N.; Schmidt, V. M., Electrochemical characteristics and performance of CoTMPP/BP oxygen reduction electrocatalysts for PEM fuel cell. *Electrochem Commun* **2006,** *8* (3), 389-394.
18. Pylypenko, S.; Mukherjee, S.; Olson, T. S.; Atanassov, P., Non-platinum oxygen reduction electrocatalysts based on pyrolyzed transition metal macrocycles. *Electrochim Acta* **2008,** *53* (27), 7875-7883.
19. Vanveen, J. A. R.; Vanbaar, J. F.; Kroese, C. J.; Coolegem, J. G. F.; Dewit, N.; Colijn, H. A., Oxygen Reduction on Transition-Metal Porphyrins in Acid Electrolyte .1. Activity. *Ber Bunsen Phys Chem* **1981,** *85* (8), 693-700.
20. Vanveen, J. A. R.; Vanbaar, J. F.; Kroese, K. J., Effect of Heat-Treatment on the Performance of Carbon-Supported Transition-Metal Chelates in the Electrochemical Reduction of Oxygen. *J Chem Soc Farad T 1* **1981,** *77*, 2827-2843.
21. Ziegelbauer, J. M.; Olson, T. S.; Pylypenko, S.; Alamgir, F.; Jaye, C.; Atanassov, P.; Mukerjee, S., Direct spectroscopic observation of the structural origin of peroxide generation from co-based pyrolyzed porphyrins for ORR applications. *J Phys Chem C* **2008,** *112* (24), 8839-8849.
22. Faubert, G.; Lalande, G.; Cote, R.; Guay, D.; Dodelet, J. P.; Weng, L. T.; Bertrand, P.; Denes, G., Heat-treated iron and cobalt tetraphenylporphyrins adsorbed on carbon black: Physical characterization and catalytic properties of these materials for the reduction of oxygen in polymer electrolyte fuel cells. *Electrochim Acta* **1996,** *41* (10), 1689-1701.
23. Vanveen, J. A. R.; Visser, C., Oxygen Reduction on Monomeric Transition-Metal Phthalocyanines in Acid Electrolyte. *Electrochim Acta* **1979,** *24* (9), 921-928.
24. Wiesener, K.; Ohms, D.; Neumann, V.; Franke, R., N-4 Macrocycles as Electrocatalysts for the Cathodic Reduction of Oxygen. *Mater Chem Phys* **1989,** *22* (3-4), 457-475.

25. Bron, M.; Radnik, J.; Fieber-Erdmann, M.; Bogdanoff, P.; Fiechter, S., EXAFS, XPS and electrochemical studies on oxygen reduction catalysts obtained by heat treatment of iron phenanthroline complexes supported on high surface area carbon black. *J Electroanal Chem* **2002,** *535* (1-2), 113-119.
26. Lefevre, M.; Proietti, E.; Jaouen, F.; Dodelet, J. P., Iron-based catalysts with improved oxygen reduction activity in polymer electrolyte fuel cells. *Science* **2009,** *324* (5923), 71-4.
27. Otake, Y.; Jenkins, R. G., Characterization of Oxygen-Containing Surface Complexes Created on a Microporous Carbon by Air and Nitric-Acid Treatment. *Carbon* **1993,** *31* (1), 109-121.
28. Vinke, P.; van der Eijk, M.; Verbree, M.; Voskamp, A. F.; van Bekkum, H., Modification of the surfaces of a gasactivated carbon and a chemically activated carbon with nitric acid, hypochlorite, and ammonia. *Carbon* **1994,** *32* (4), 675-686.
29. Pradhan, B. K.; Sandle, N. K., Effect of different oxidizing agent treatments on the surface properties of activated carbons. *Carbon* **1999,** *37* (8), 1323-1332.
30. Chen, X.; Farber, M.; Gao, Y. M.; Kulaots, I.; Suuberg, E. M.; Hurt, R. H., Mechanisms of surfactant adsorption on non-polar, air-oxidized and ozone-treated carbon surfaces. *Carbon* **2003,** *41* (8), 1489-1500.
31. Jun, S.; Choi, M.; Ryu, S.; Lee, H.-Y.; Ryoo, R., Ordered mesoporous carbon molecular sieves with functionalized surfaces. In *Studies in Surface Science and Catalysis*, Park, S.-E.; Ryoo, R.; Ahn, W.-S.; Lee, C. W.; Chang, J.-S., Eds. Elsevier: 2003; Vol. 146, pp 37-40.
32. Jiang, K. Y.; Schadler, L. S.; Siegel, R. W.; Zhang, X. J.; Zhang, H. F.; Terrones, M., Protein immobilization on carbon nanotubes via a two-step process of diimide-activated amidation. *J Mater Chem* **2004,** *14* (1), 37-39.
33. Titirici, M. M.; Thomas, A.; Antonietti, M., Aminated hydrophilic ordered mesoporous carbons. *J Mater Chem* **2007,** *17* (32), 3412-3418.
34. Wang, L. F.; Zhao, Y.; Lin, K. F.; Zhao, X. J.; Shan, Z. C.; Di, Y.; Sun, Z. H.; Cao, X. J.; Zou, Y. C.; Jiang, D. Z.; Jiang, L.; Xiao, F. S., Super-hydrophobic ordered mesoporous carbon monolith. *Carbon* **2006,** *44* (7), 1336-1339.
35. Cosnier, F.; Celzard, A.; Furdin, G.; Begin, D.; Mareche, J. F.; Barres, O., Hydrophobisation of active carbon surface and effect on the adsorption of water. *Carbon* **2005,** *43* (12), 2554-2563.
36. He, Q.; Xu, Y. B.; Wang, C. H.; She, S. K.; Zhou, S.; Wang, R., Silane modification and characterization of activated carbon. *Adsorption-Journal of the International Adsorption Society* **2012,** *18* (1), 23-29.
37. Stein, A.; Wang, Z. Y.; Fierke, M. A., Functionalization of Porous Carbon Materials with Designed Pore Architecture. *Adv Mater* **2009,** *21* (3), 265-293.
38. Li, Z.; Yan, W.; Dai, S., Surface functionalization of ordered mesoporous carbons--a comparative study. *Langmuir* **2005,** *21* (25), 11999-2006.
39. Kim, J. H.; Kim, T.; Jeong, Y. C.; Lee, K.; Park, K. T.; Yang, S. J.; Park, C. R., Stabilization of Insoluble Discharge Products by Facile Aniline Modification for High Performance Li-S Batteries. *Adv Energy Mater* **2015,** *5* (14), 1500268-n/a.
40. Jaffe, A.; Valdes, A. S.; Karunadasa, H. I., Quinone-Functionalized Carbon Black Cathodes for Lithium Batteries with High Power Densities. *Chem Mater* **2015,** *27* (10), 3568-3571.
41. Delamar, M.; Hitmi, R.; Pinson, J.; Saveant, J. M., Covalent Modification of Carbon Surfaces by Grafting of Functionalized Aryl Radicals Produced from Electrochemical Reduction of Diazonium Salts. *J Am Chem Soc* **1992,** *114* (14), 5883-5884.
42. Pinson, J.; Podvorica, F., Attachment of organic layers to conductive or semiconductive surfaces by reduction of diazonium salts. *Chemical Society Reviews* **2005,** *34* (5), 429-439.
43. Wang, X. Q.; Liu, R.; Waje, M. M.; Chen, Z. W.; Yan, Y. S.; Bozhilov, K. N.; Feng, P. Y., Sulfonated ordered mesoporous carbon as a stable and highly active protonic acid catalyst. *Chem Mater* **2007,** *19* (10), 2395-2397.
44. Beamson, G.; Briggs, D., *High Resolution XPS of Organic Polymers: the Scienta ESCA300 Database*. John Wiley and Sons: West Sussex, England, 1992.
45. Janson, C. Iron-nitrogen containing carbon catalysts for oxygen reduction in fuel cells - Synthesis, structural characterization and electrochemical evaluation. Chalmers University of Technology, 2018.
46. Jankowski, P. Computational and experimental studies on SEI forming electrolyte additvies for lithium-ion batteries. Warsaw University of Technology, 2018.
47. Frisch, M. J.; Trucks, G. W.; Schlegel, H. B.; Scuseria, G. E.; Robb, M. A.; Cheeseman, J. R.; Scalmani, G.; Barone, V.; Petersson, G. A.; Nakatsuji, H.; Li, X.; Caricato, M.; Marenich, A. V.; Bloino, J.; Janesko, B. G.; Gomperts, R.; Mennucci, B.; Hratchian, H. P.; Ortiz, J. V.; Izmaylov, A. F.; Sonnenberg, J. L.; Williams; Ding, F.; Lipparini, F.; Egidi, F.; Goings, J.; Peng, B.; Petrone, A.; Henderson, T.; Ranasinghe, D.; Zakrzewski, V. G.; Gao, J.; Rega, N.; Zheng, G.; Liang, W.; Hada, M.; Ehara, M.; Toyota, K.; Fukuda, R.; Hasegawa, J.; Ishida, M.; Nakajima, T.; Honda, Y.; Kitao, O.; Nakai, H.; Vreven, T.; Throssell, K.; Montgomery Jr., J. A.; Peralta, J. E.; Ogliaro, F.; Bearpark, M. J.; Heyd, J. J.; Brothers, E. N.; Kudin, K. N.; Staroverov, V. N.; Keith, T. A.; Kobayashi, R.; Normand, J.; Raghavachari, K.; Rendell, A. P.; Burant, J. C.; Iyengar, S. S.; Tomasi, J.; Cossi, M.; Millam, J. M.; Klene, M.; Adamo, C.; Cammi, R.;

Ochterski, J. W.; Martin, R. L.; Morokuma, K.; Farkas, O.; Foresman, J. B.; Fox, D. J. *Gaussian 16 Rev. B.01*, Wallingford, CT, 2016.
48. Scrosati, B., History of lithium batteries. *Journal of Solid State Electrochemistry* **2011,** *15* (7-8), 1623-1630.
49. Simonin, L. In *Batteries and Na-ion batteries basics*, NAIADES Summerschool Sodium-ion Batteries: Fundamentals & Applications, Smögen, Sweden, 30-05-17; Smögen, Sweden, 2017; p 50.
50. Daniel, C.; Besenhard, J. O., *Handbook of Battery Materials*. Wiley: 2011.
51. Choi, N. S.; Chen, Z.; Freunberger, S. A.; Ji, X.; Sun, Y. K.; Amine, K.; Yushin, G.; Nazar, L. F.; Cho, J.; Bruce, P. G., Challenges facing lithium batteries and electrical double-layer capacitors. *Angew Chem Int Ed Engl* **2012,** *51* (40), 9994-10024.
52. Nitta, N.; Wu, F. X.; Lee, J. T.; Yushin, G., Li-ion battery materials: present and future. *Materials Today* **2015,** *18* (5), 252-264.
53. Tarascon, J. M.; Armand, M., Issues and challenges facing rechargeable lithium batteries. *Nature* **2001,** *414* (6861), 359-67.
54. Chu, S.; Cui, Y.; Liu, N., The path towards sustainable energy. *Nat Mater* **2016,** *16* (1), 16-22.
55. Imanishi, N.; Yamamoto, O., Rechargeable lithium-air batteries: characteristics and prospects. *Materials Today* **2014,** *17* (1), 24-30.
56. Bruce, P. G.; Freunberger, S. A.; Hardwick, L. J.; Tarascon, J. M., Li-O2 and Li-S batteries with high energy storage. *Nat Mater* **2011,** *11* (1), 19-29.
57. Pang, Q.; Liang, X.; Kwok, C. Y.; Nazar, L. F., Advances in lithium-sulfur batteries based on multifunctional cathodes and electrolytes. *Nature Energy* **2016,** *1*, 16132.
58. Helmenstine, A. M. Table of Electrical Resistivity and Conductivity. https://www.thoughtco.com/table-of-electrical-resistivity-conductivity-608499.
59. Nazar, L. F.; Cuisinier, M.; Pang, Q., Lithium-sulfur batteries. *MRS Bulletin* **2014,** *39* (05), 436-442.
60. Yin, Y. X.; Xin, S.; Guo, Y. G.; Wan, L. J., Lithium-sulfur batteries: electrochemistry, materials, and prospects. *Angew Chem Int Ed Engl* **2013,** *52* (50), 13186-200.
61. Bresser, D.; Passerini, S.; Scrosati, B., Recent progress and remaining challenges in sulfur-based lithium secondary batteries--a review. *Chem Commun (Camb)* **2013,** *49* (90), 10545-62.
62. Harks, P. P. R. M. L.; Robledo, C. B.; Verhallen, T. W.; Notten, P. H. L.; Mulder, F. M., The Significance of Elemental Sulfur Dissolution in Liquid Electrolyte Lithium Sulfur Batteries. *Adv Energy Mater* **2017,** *7* (3).
63. Cheon, S.-E.; Ko, K.-S.; Cho, J.-H.; Kim, S.-W.; Chin, E.-Y.; Kim, H.-T., Rechargeable Lithium Sulfur Battery. *J Electrochem Soc* **2003,** *150* (6).
64. Lim, D. H.; Agostini, M.; Nitze, F.; Manuel, J.; Ahn, J. H.; Matic, A., Route to sustainable lithium-sulfur batteries with high practical capacity through a fluorine free polysulfide catholyte and self-standing Carbon Nanofiber membranes. *Sci Rep* **2017,** *7* (1), 6327.
65. Wang, Q.; Jin, J.; Wu, X.; Ma, G.; Yang, J.; Wen, Z., A shuttle effect free lithium sulfur battery based on a hybrid electrolyte. *Phys Chem Chem Phys* **2014,** *16* (39), 21225-9.
66. Ryu, H. S.; Ahn, H. J.; Kim, K. W.; Ahn, J. H.; Cho, K. K.; Nam, T. H., Self-discharge characteristics of lithium/sulfur batteries using TEGDME liquid electrolyte. *Electrochim Acta* **2006,** *52* (4), 1563-1566.
67. Manthiram, A.; Fu, Y.; Su, Y. S., Challenges and prospects of lithium-sulfur batteries. *Acc Chem Res* **2013,** *46* (5), 1125-34.
68. Ji, X.; Lee, K. T.; Nazar, L. F., A highly ordered nanostructured carbon-sulphur cathode for lithium-sulphur batteries. *Nat Mater* **2009,** *8* (6), 500-6.
69. Mikhaylik, Y.; Kovalev, I.; Schock, R.; Kumaresan, K.; Xu, J.; Affinito, J., High Energy Rechargeable Li-S Cells for EV Application. Status, Remaining Problems and Solutions. *Battery/Energy Technology (General) - 216th Ecs Meeting* **2010,** *25* (35), 23-34.
70. Yuan, L. X.; Feng, J. K.; Ai, X. P.; Cao, Y. L.; Chen, S. L.; Yang, H. X., Improved dischargeability and reversibility of sulfur cathode in a novel ionic liquid electrolyte. *Electrochem Commun* **2006,** *8* (4), 610-614.
71. Tamura, T.; Hachida, T.; Yoshida, K.; Tachikawa, N.; Dokko, K.; Watanabe, M., New glyme-cyclic imide lithium salt complexes as thermally stable electrolytes for lithium batteries. *J Power Sources* **2010,** *195* (18), 6095-6100.
72. Zhang, S. S., Liquid electrolyte lithium/sulfur battery: Fundamental chemistry, problems, and solutions. *J Power Sources* **2013,** *231*, 153-162.
73. Aihara, Y.; Bando, T.; Nakagawa, H.; Yoshida, H.; Hayamizu, K.; Akiba, E.; Price, W. S., Ion Transport Properties of Six Lithium Salts Dissolved in γ-Butyrolactone Studied by Self-Diffusion and Ionic Conductivity Measurements. *J Electrochem Soc* **2004,** *151* (1).
74. Mikhaylik, Y. V., Electrolytes for lithium sulfur cells. Google Patents: 2008.

75. Ding, N.; Zhou, L.; Zhou, C.; Geng, D.; Yang, J.; Chien, S. W.; Liu, Z.; Ng, M. F.; Yu, A.; Hor, T. S.; Sullivan, M. B.; Zong, Y., Building better lithium-sulfur batteries: from LiNO3 to solid oxide catalyst. *Sci Rep* **2016,** *6*, 33154.
76. Aurbach, D.; Pollak, E.; Elazari, R.; Salitra, G.; Kelley, C. S.; Affinito, J., On the Surface Chemical Aspects of Very High Energy Density, Rechargeable Li-Sulfur Batteries. *J Electrochem Soc* **2009,** *156* (8), A694-A702.
77. Zhang, S. S., Role of LiNO3 in rechargeable lithium/sulfur battery. *Electrochim Acta* **2012,** *70*, 344-348.
78. Liang, X.; Wen, Z. Y.; Liu, Y.; Wu, M. F.; Jin, J.; Zhang, H.; Wu, X. W., Improved cycling performances of lithium sulfur batteries with LiNO3-modified electrolyte. *J Power Sources* **2011,** *196* (22), 9839-9843.
79. Gong, Z. J.; Wu, Q. X.; Wang, F.; Li, X.; Fan, X. P.; Yang, H.; Luo, Z. K., A hierarchical micro/mesoporous carbon fiber/sulfur composite for high-performance lithium-sulfur batteries. *Rsc Adv* **2016,** *6* (44), 37443-37451.
80. Fretz, S. J.; Agostini, M.; Matic, A.; Palmqvist, A. E. C., Synthesis of amide-functionalized carbons for lithium-sulfur batteries. *Manuscript in preparation* **2019**.
81. Fretz, S. J.; Lyons, C. T.; Levin, E.; Chidsey, C. E. D.; Palmqvist, A. E. C.; Stack, T. D. P., Bromomethylation of high-surface area carbons as a versatile synthon: Adjusting the electrode-electrolyte interface in lithium-sulfur batteries. *Under review* **2019**.
82. Zhang, S. S., A new finding on the role of LiNO3 in lithium-sulfur battery. *J Power Sources* **2016,** *322*, 99-105.
83. Sun, X. L.; Jianwen, L.; Weihan, L.; Jing, L.; Xia, L.; Xiaofei, Y.; Yongfeng, H.; Qunfeng, X.; Wanqun, Z.; Ruying, L.; Tsun-Kong, S.; Xueliang, Stabilizing Sulfur Cathode in Carbonate and Ether Electrolytes: Excluding Long-Chain Lithium Polysulfide Formation and Switching Lithiation/Delithiation Route. **2019**.
84. Chen, Z.; Jean-Pol, D.; Jiujun, Z., *Non-Noble Metal Fuel Cell Catalysts*. Wiley-VCH: 2014; p 448.
85. Williams, M. C., *Fuel Cell Handbook, 7th Edition*. US Department of Energy: 2004.
86. Moroimoto, Y., Alternative PEFC Catalysts for Future Commercial FCVs. *EFCD 2015 - Challenges Towards Zero Platinum for Oxygen Reduction* **2015**.
87. Gong, K.; Du, F.; Xia, Z.; Durstock, M.; Dai, L., Nitrogen-doped carbon nanotube arrays with high electrocatalytic activity for oxygen reduction. *Science* **2009,** *323* (5915), 760-4.
88. Wu, G.; More, K. L.; Johnston, C. M.; Zelenay, P., High-performance electrocatalysts for oxygen reduction derived from polyaniline, iron, and cobalt. *Science* **2011,** *332* (6028), 443-7.
89. Janson, C.; Dombrovskis, J. K.; Palmqvist, A. E. C., Influence of iron precursor hydration state on performance of non-precious metal fuel cell catalysts. *J Mater Chem A* **2018,** *6* (7), 3116-3125.
90. Dombrovskis, J. K.; Palmqvist, A. E. C., One-pot synthesis of transition metal ion-chelating ordered mesoporous carbon/carbon nanotube composites for active and durable fuel cell catalysts. *J Power Sources* **2017,** *357*, 87-96.
91. Dombrovskis, J. K.; Palmqvist, A. E. C., The Active Site Structure of Transition Metal Ion-Chelating Ordered Mesoporous Carbon Fuel Cell Catalysts. *Fuel Cells* **2016,** *16* (1), 23-31.
92. Dombrovskis, J. K.; Palmqvist, A. E. C., Recent Progress in Synthesis, Characterization and Evaluation of Non-Precious Metal Catalysts for the Oxygen Reduction Reaction. *Fuel Cells* **2016,** *16* (1), 4-22.
93. Ramaswamy, N.; Tylus, U.; Jia, Q.; Mukerjee, S., Activity descriptor identification for oxygen reduction on nonprecious electrocatalysts: linking surface science to coordination chemistry. *J Am Chem Soc* **2013,** *135* (41), 15443-9.
94. Ge, X. M.; Sumboja, A.; Wuu, D.; An, T.; Li, B.; Goh, F. W. T.; Hor, T. S. A.; Zong, Y.; Liu, Z. L., Oxygen Reduction in Alkaline Media: From Mechanisms to Recent Advances of Catalysts. *Acs Catal* **2015,** *5* (8), 4643-4667.
95. Burstyn, J. N.; Roe, J. A.; Miksztal, A. R.; Shaevitz, B. A.; Lang, G.; Valentine, J. S., Magnetic and Spectroscopic Characterization of an Iron Porphyrin Peroxide Complex - Peroxoferrioctaethylporphyrin(1-). *J Am Chem Soc* **1988,** *110* (5), 1382-1388.
96. Yatsunyk, L. A.; Walker, F. A., NMR and EPR spectroscopic and structural studies of low-spin, $(d_{xz},d_{yz})^4(d_{xy})^1$ ground state Fe(III) bis-tert-butylisocyanide complexes of dodecasubstituted porphyrins. *Inorg Chem* **2004,** *43* (14), 4341-52.
97. Petasis, D. T.; Hendrich, M. P., Quantitative interpretation of EPR spectroscopy with applications for iron-sulfur proteins In *Iron-Sulfur Clusters in Chemistry and Biology*, Rouault, T. A., Ed. 2014; pp 21-48.
98. Wittenberg, J. B.; Wittenberg, B. A.; Peisach, J.; Blumberg, W. E., On the state of the iron and the nature of the ligand in oxyhemoglobin. *Proc Natl Acad Sci U S A* **1970,** *67* (4), 1846-53.
99. Lan, M. B.; Zhao, H. L.; Yuan, H. H.; Jiang, C. R.; Zuo, S. H.; Jiang, Y., Absorption and EPR spectra of some porphyrins and metalloporphyrins. *Dyes Pigments* **2007,** *74* (2), 357-362.
100. Shpak, A. P.; Kolesnik, S. P.; Mogilny, G. S.; Petrov, Y. N.; Sokhatsky, V. P.; Trophimova, L. N.; Shanina, B. D.; Gavrijuk, V. G., Structure and magnetic properties of iron nanowires encased in multiwalled carbon nanotubes. *Acta Mater* **2007,** *55* (5), 1769-1778.

101. Koksharov, Y. A.; Pankratov, D. A.; Gubin, S. P.; Kosobudsky, I. D.; Beltran, M.; Khodorkovsky, Y.; Tishin, A. M., Electron paramagnetic resonance of ferrite nanoparticles. *J. Appl. Phys.* **2001,** *89* (4), 2293-2298.
102. Ferguson, R. M.; Minard, K. R.; Krishnan, K. M., Optimization of nanoparticle core size for magnetic particle imaging. *J Magn Magn Mater* **2009,** *321* (10), 1548-1551.
103. van der Kraan, A. M.; Ramselaar, W. L. T. M.; de Beer, V. H. J., Mössbauer Spectroscopy of Iron and Iron-Molybdenum Hydrotreating Catalysts. In *Mössbauer Spectroscopy Applied to Inorganic Chemistry*, Long, G. J.; Grandjean, F., Eds. Springer: Boston, MA, USA, 1989; Vol. 3.
104. Takayama, T.; Takagi, H., Phase-change magnetic memory effect in cation-deficient iron sulfide $Fe_{1-x}S$. *Appl Phys Lett* **2006,** *88* (1).
105. McMurry, J., *Organic chemistry*. Cengage Learning, Boston, MA, USA: 2016.
106. Liang, C.; Li, Z.; Dai, S., Mesoporous carbon materials: synthesis and modification. *Angew Chem Int Ed Engl* **2008,** *47* (20), 3696-717.
107. McCreery, R. L., Advanced carbon electrode materials for molecular electrochemistry. *Chem Rev* **2008,** *108* (7), 2646-2687.
108. Benzigar, M. R.; Talapaneni, S. N.; Joseph, S.; Ramadass, K.; Singh, G.; Scaranto, J.; Ravon, U.; Al-Bahily, K.; Vinu, A., Recent advances in functionalized micro and mesoporous carbon materials: synthesis and applications. *Chem Soc Rev* **2018,** *47* (8), 2680-2721.
109. Vandermade, A. W.; Vandermade, R. H., A Convenient Procedure for Bromomethylation of Aromatic-Compounds - Selective Monobromomethylation, Bisbromomethylation, or Trisbromomethylation. *J Org Chem* **1993,** *58* (5), 1262-1263.
110. Samuels, W. D.; LaFemina, N. H.; Sukwarotwat, V.; Yantasee, W.; Li, X. H. S.; Fryxell, G. E., Chloromethylated Activated Carbon: A Useful New Synthon for Making a Novel Class of Sorbents for Heavy Metal Separations. *Separ Sci Technol* **2010,** *45* (2), 228-235.
111. Stenehjem, E. D.; Ziatdinov, V. R.; Stack, T. D.; Chidsey, C. E., Gas-phase azide functionalization of carbon. *J Am Chem Soc* **2013,** *135* (3), 1110-6.
112. Jun, S.; Joo, S. H.; Ryoo, R.; Kruk, M.; Jaroniec, M.; Liu, Z.; Ohsuna, T.; Terasaki, O., Synthesis of new, nanoporous carbon with hexagonally ordered mesostructure. *J Am Chem Soc* **2000,** *122* (43), 10712-10713.
113. Carbon Black - Vulcan XC 72R. http://www.fuelcellstore.com/vulcan-xc-72r.
114. Chidsey, C. E. D.; Bertozzi, C. R.; Putvinski, T. M.; Mujsce, A. M., Coadsorption of Ferrocene-Terminated and Unsubstituted Alkanethiols on Gold - Electroactive Self-Assembled Monolayers. *J Am Chem Soc* **1990,** *112* (11), 4301-4306.
115. Pellow, M. A.; Stack, T. D.; Chidsey, C. E., Squish and CuAAC: additive-free covalent monolayers of discrete molecules in seconds. *Langmuir* **2013,** *29* (18), 5383-7.
116. Li, J.; Vaisman, L.; Marom, G.; Kim, J. K., Br treated graphite nanoplatelets for improved electrical conductivity of polymer composites. *Carbon* **2007,** *45* (4), 744-750.
117. Zhou, X. L.; Coon, S. R.; White, J. M., Potassium promoted decomposition of methyl bromide on Ag(111). *The Journal of Chemical Physics* **1991,** *94* (2), 1613-1625.
118. Min, M.; Seo, S.; Lee, J.; Lee, S. M.; Hwang, E.; Lee, H., Changes in major charge transport by molecular spatial orientation in graphene channel field effect transistors. *Chem Commun (Camb)* **2013,** *49* (56), 6289-91.
119. Ripin, D. H.; Evans, D. A., pKa Table.
120. Atkins, P. W., *Shriver & Atkins' inorganic chemistry*. Oxford University Press: Oxford; New York, 2010.
121. Devadoss, A.; Chidsey, C. E., Azide-modified graphitic surfaces for covalent attachment of alkyne-terminated molecules by "click" chemistry. *J Am Chem Soc* **2007,** *129* (17), 5370-1.
122. McCrory, C. C.; Devadoss, A.; Ottenwaelder, X.; Lowe, R. D.; Stack, T. D.; Chidsey, C. E., Electrocatalytic O2 reduction by covalently immobilized mononuclear copper(I) complexes: evidence for a binuclear Cu2O2 intermediate. *J Am Chem Soc* **2011,** *133* (11), 3696-9.
123. Unger, E. L.; Fretz, S. J.; Lim, B.; Margulis, G. Y.; McGehee, M. D.; Stack, T. D., Sequential "click" functionalization of mesoporous titania for energy-relay dye enhanced dye-sensitized solar cells. *Phys Chem Chem Phys* **2015,** *17* (9), 6565-71.
124. Reich, H. J. Overview of Enolate Alkylations. https://www.chem.wisc.edu/areas/reich/chem547/1-carbonyl%7B06%7D.htm.
125. Chakravarti, R.; Kantam, M. L.; Iwai, H.; Al-deyab, S. S.; Ariga, K.; Park, D.-H.; Choy, J.-H.; Lakhi, K. S.; Vinu, A., Mesoporous Carbons Functionalized with Aromatic, Aliphatic, and Cyclic Amines, and their Superior Catalytic Activity. *ChemCatChem* **2014,** *6* (10), 2872-2880.
126. Moulder, J. F.; Stickle, W. F.; Sobol, P. E.; Bomben, K. D., *Handbook of X-ray Photoelectron Spectroscopy*. Perkin-Elmer Corporation, Physical Electronic Division: 1992.

127. Zheng, G.; Zhang, Q.; Cha, J. J.; Yang, Y.; Li, W.; Seh, Z. W.; Cui, Y., Amphiphilic surface modification of hollow carbon nanofibers for improved cycle life of lithium sulfur batteries. *Nano Lett* **2013,** *13* (3), 1265-70.
128. Seh, Z. W.; Zhang, Q. F.; Li, W. Y.; Zheng, G. Y.; Yao, H. B.; Cui, Y., Stable cycling of lithium sulfide cathodes through strong affinity with a bifunctional binder. *Chem Sci* **2013,** *4* (9), 3673-3677.
129. Ramraj, A.; Hillier, I. H.; Vincent, M. A.; Burton, N. A., Assessment of approximate quantum chemical methods for calculating the interaction energy of nucleic acid bases with graphene and carbon nanotubes. *Chemical Physics Letters* **2010,** *484* (4-6), 295-298.
130. Manthiram, A.; Fu, Y.; Chung, S. H.; Zu, C.; Su, Y. S., Rechargeable lithium-sulfur batteries. *Chem Rev* **2014,** *114* (23), 11751-87.
131. Wang, Z. Y.; Li, F.; Ergang, N. S.; Stein, A., Effects of hierarchical architecture on electronic and mechanical properties of nanocast monolithic porous carbons and carbon-carbon nanocomposites. *Chem Mater* **2006,** *18* (23), 5543-5553.
132. Jaramillo, J.; Alvarez, P. M.; Gomez-Serrano, V., Oxidation of activated carbon by dry and wet methods Surface chemistry and textural modifications. *Fuel Processing Technology* **2010,** *91* (11), 1768-1775.
133. Xu, Z. L.; Lin, S.; Onofrio, N.; Zhou, L.; Shi, F.; Lu, W.; Kang, K.; Zhang, Q.; Lau, S. P., Exceptional catalytic effects of black phosphorus quantum dots in shuttling-free lithium sulfur batteries. *Nat Commun* **2018,** *9* (1), 4164.
134. Tao, X.; Wang, J.; Ying, Z.; Cai, Q.; Zheng, G.; Gan, Y.; Huang, H.; Xia, Y.; Liang, C.; Zhang, W.; Cui, Y., Strong sulfur binding with conducting Magneli-phase Ti(n)O2(n-1) nanomaterials for improving lithium-sulfur batteries. *Nano Lett* **2014,** *14* (9), 5288-94.
135. Sun, M.; Wang, X.; Wang, J.; Yang, H.; Wang, L.; Liu, T., Assessment on the Self-Discharge Behavior of Lithium-Sulfur Batteries with LiNO3-Possessing Electrolytes. *ACS Appl Mater Interfaces* **2018,** *10* (41), 35175-35183.
136. Moy, D.; Manivannan, A.; Narayanan, S. R., Direct Measurement of Polysulfide Shuttle Current: A Window into Understanding the Performance of Lithium-Sulfur Cells. *J Electrochem Soc* **2014,** *162* (1), A1-A7.